uc3m

Heliostat field aiming strategies

Universidad
Carlos III de Madrid

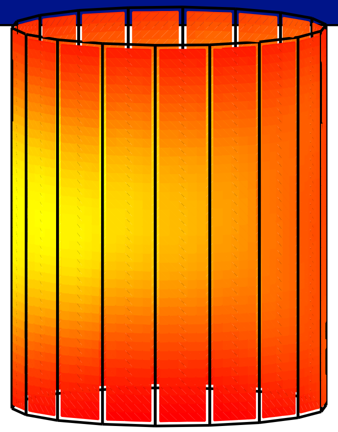

Heliostat field aiming strategies

for solar central receivers

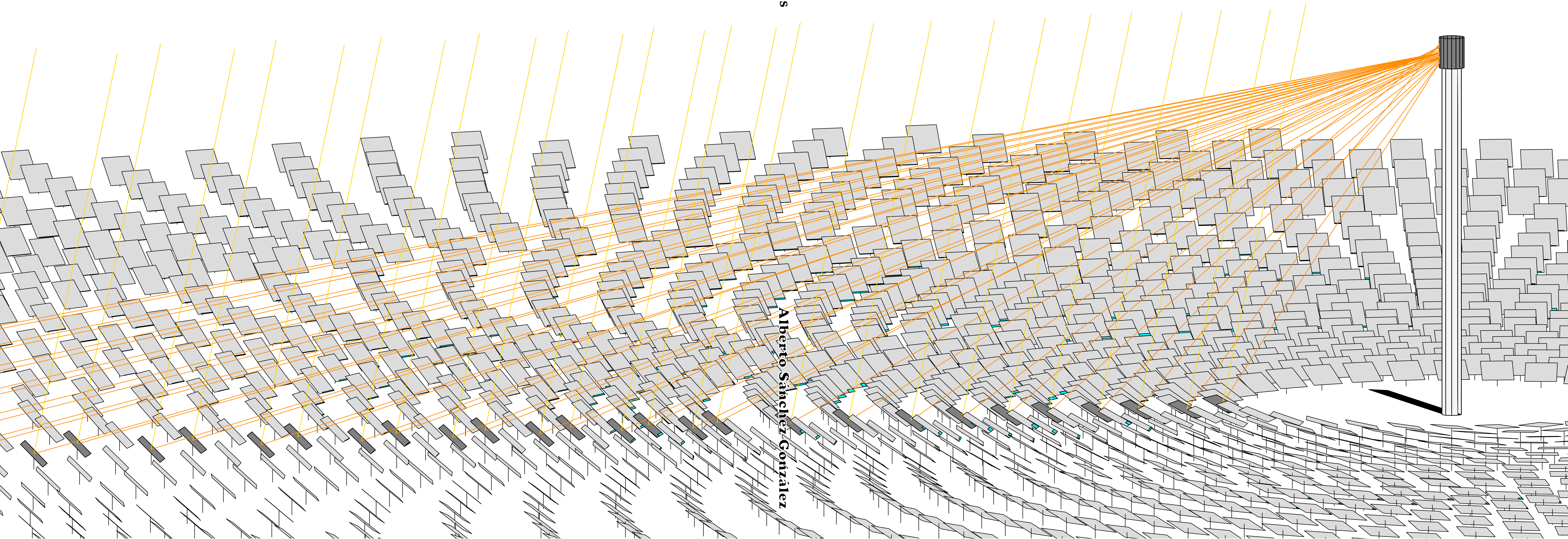

Alberto Sánchez González

Universidad
Carlos III
de Madrid

ISE Research Group

Departamento de ingeniería térmica y de fluidos

Ph.D. Thesis | 2016

Doctoral Thesis

Alberto Sánchez González

uc3m | Universidad Carlos III de Madrid

Ph.D. Thesis

Heliostat field aiming strategies
for solar central receivers

Author
Alberto Sánchez González

Advisor
Domingo Santana Santana

DEPARTAMENTO DE INGENIERÍA TÉRMICA Y DE FLUIDOS

Leganés, diciembre 2016

uc3m | Universidad Carlos III de Madrid

Tesis Doctoral

Heliostat field aiming strategies for solar central receivers

Autor
Alberto Sánchez González

Director
Domingo Santana Santana

Firma del Tribunal Calificador:

Firma

Presidente
D. Manuel Jesús Blanco Muriel | The Cyprus Institute

Secretario
D. Manuel Romero Álvarez | IMDEA Energía

Vocal
D. Francisco Javier Collado Giménez | Universidad de Zaragoza

Calificación:

Leganés, 16 de diciembre de 2016

DEPARTAMENTO DE INGENIERÍA TÉRMICA Y DE FLUIDOS
Escuela Politécnica Superior

Heliostat field aiming strategies
for solar central receivers

Doctorado en Ingeniería Mecánica y de Organización Industrial

Autor
Alberto Sánchez González

Director
Domingo Santana Santana

Leganés, diciembre 2016

A mis padres, mi hermana y Cristina

The Sun is God
J.M.W. Turner

Las cualidades indispensables al cultivador de la investigación son:
la independencia de juicio, la curiosidad intelectual, la perseverancia en el estudio, [...]
y el gusto por la originalidad científica.
Santiago Ramón y Cajal

An algorithm must be seen to be believed,
and the best way to learn what an algorithm is all about is to try it.
Donald E. Knuth

Acknowledgments

I thank Cyril Caliot, senior researcher at PROMES-CNRS laboratory, for supporting my research stay that finally resulted in Chapter 3 of this thesis. I also acknowledge Alain Ferrière, Antoine Pérez, Yann Volut and William Baltus for their help during the experimental phase at THEMIS solar power tower plant. I am indebted to Universidad Carlos III de Madrid for the mobility grant that funded the stay at PROMES-CNRS during spring-summer 2016.

I acknowledge Rafael Monterreal, Plataforma Solar de Almería, for providing the experimental images that helped to validate the model described in Chapter 2.

I also show gratitude to the anonymous journal reviewers for their comments and suggestions on the manuscripts that finally resulted in the published articles. Similarly, I acknowledge the external experts assessment to fulfill the international mention requirements, which has been carried out by: Giampaolo Manzolini (Politecnico di Milano); Ricardo Vasquez Padilla (Southern Cross University); and Luis Cutz (Chalmers University of Technology).

Last but not least, I am grateful to my thesis advisor, Domingo Santana, and colleague Reyes Rodríguez, without whom this thesis would not have been possible. I also appreciate the companionship and encouragement from colleagues and friends.

Resumen

La presente tesis está dedicada al desarrollo de modelos ópticos aplicados a la tecnología de central solar tipo torre. Más concretamente, este trabajo se centra en el modelado de mapas de flujo y estrategias de apuntamiento para sistemas de receptor central. Los códigos resultantes son de utilidad en las fases de diseño y operación de centrales solares de torre. Esta memoria fundamentalmente presenta cuatro modelos computacionales.

El primer modelo, sobre el cual se construyen el resto de modelos, calcula la distribución de densidad de flujo incidente en cualquier tipo de receptor central y que es causada por un único heliostato. El procedimiento se basa en la proyección oblicua de la malla de cálculo desde el receptor hasta el plano imagen, en donde se evalúa una función analítica de precisión conocida, e.g. UNIZAR. La proyección oblicua se obtiene mediante un adecuado cambio de sistemas de coordenadas. El método de proyección reproduce notablemente la distorsión presente en la mancha de luz concentrada cuando el ángulo de incidencia con el receptor es elevado. Este modelo básico ha sido validado con medidas de distribución de flujo en un receptor plano y con simulaciones de Monte Carlo de trazado de rayos para un receptor cilíndrico. En comparación con SolTrace, el modelo propuesto requiere un tiempo de computación 50 veces inferior y con un nivel de resolución aún mayor.

El segundo modelo determina los errores de canteo en las facetas de heliostatos reales. En base a un algoritmo de optimización determinista, se ha establecido un procedimiento que ajusta los mapas de flujo simulados con las imágenes tomadas en un blanco lambertiano. Se han empleado imágenes experimentales tomadas en la planta THEMIS para encontrar los errores de reglaje en tres heliostatos CETHEL seleccionados. A partir de los resultados del modelo, uno de los heliostatos ha sido satisfactoriamente reajustado, mejorando de forma significativa su calidad óptica y validando la metodología propuesta.

El tercer modelo es una ampliación del primero de ellos para superponer los mapas de flujo producidos por cada uno de los heliostatos en un campo completo. Las pérdidas ópticas por sombras y bloqueos se calculan mediante proyección paralela de los heliostatos vecinos. Se ha desarrollado una estrategia de apuntamiento que da lugar a mapas de flujo simétricos respecto de la línea media ecuatorial del receptor y que depende de un solo parámetro: k, factor de apuntamiento. Con $k = 3$ se obtienen mapas de flujo similares a los de apuntamiento simple al ecuador, mientras que con $k = 0$ los heliostatos apuntan a los bordes inferior y superior del receptor. Para el caso de estudio basado en Gemasolar, un factor de apuntamiento igual a 2 da lugar a las distribuciones de flujo más uniformes, i.e. perfil plano en la región central, sin menoscabo del factor de intercepción en comparación con el apuntamiento ecuatorial simple.

En el cuarto de los modelos se ha implementado una estrategia de apuntamiento óptima para receptores centrales de sales fundidas. Se ha desarrollado un algoritmo que maximiza la potencia térmica instantánea del receptor, al mismo tiempo que se cumplen sus límites de operación. Los límites de corrosión y estrés térmico se traducen en flujos máximos admisibles; AFD, por sus siglas en inglés. En comparación con el apuntamiento simple, habitualmente inviable, la estrategia de apuntamiento optimizado asegura la integridad del receptor, a la vez que las pérdidas por desbordamiento sólo se incrementan en 4 puntos porcentuales. Se ha comprobado que la posición óptima de los apuntamientos en cada panel se encuentra, en promedio, ligeramente desplazada hacia el lado de entrada de las sales. A pesar de los requisitos contradictorios entre paneles adyacentes de receptores multi-panel con flujo de sales en serpentín, el algoritmo consigue un buen ajuste al perfil AFD instantáneo. El código resultante requiere alrededor de 2 minutos de cálculo en una computadora estándar para determinar los apuntamientos óptimos en un campo de 2650 heliostatos.

Abstract

This thesis deals with the development of optical models for solar power tower technology. Specifically, this work is focused on modeling flux mapping and aiming strategies for central receiver systems (CRS). The resulting codes are applicable to CRS design and operation. This dissertation essentially presents four computational models.

The first model, on which the rest of the models are built up, computes the flux density distribution incident on any kind of central receiver which is caused by a single heliostat. The procedure relies on the oblique projection of the receiver mesh onto the image plane, where an accurate analytic function, e.g. UNIZAR, is evaluated. Oblique projection is accomplished by transformation of coordinate systems. The 4-step projection method remarkably reproduces the distorted spot found for large incidence angles on the heliostat and the receiver. This basic model was validated against flux measurements on a flat receiver and Monte Carlo Ray Tracing simulations on a cylindrical receiver. Compared to SolTrace, the model takes 50 times less computation time and higher level of resolution.

The second model was developed to determine canting errors in the facets of real heliostats. Based on a deterministic optimization algorithm, a procedure was set up to minimize the difference between computed flux maps and captured images on a lambertian target. Experimental images from THEMIS plant were employed to find out canting errors in selected CETHEL heliostats. From results of the model, one of the heliostats was successfully readjusted, significantly improving its optical quality, and validating the proposed methodology.

The third model extends the basic model to superpose single heliostat flux maps in a whole field of heliostats. Shading and blocking losses are computed by parallel projection of neighbor heliostats. An aiming strategy, symmetric about the receiver equator, was developed on the basis of only one parameter: k, aiming factor. Nearly single equatorial aiming is achieved with $k \geq 3$, while $k = 0$ results in pointing to either upper or lower receiver edges. For the Gemasolar case study, an aiming factor equal to 2 yielded the most uniform flux maps, i.e. flat profile in the central region, and negligible increase in spillage losses compared to equatorial aiming.

An optimal aiming strategy for molten salt receivers was implemented in the fourth model. An algorithm was developed to maximize receiver thermal output, while meeting at the same time corrosion and thermal stress limits; which were translated into allowable flux densities, AFD. Compared to unreliable single aiming, the optimized aiming strategy ensures receiver integrity and spillage losses only increase up to 4 percentage points. It was found that optimal aim points are, on average, slightly shifted towards the panel entrance. Despite the conflicting demand between adjacent panels in multi-panel receivers with serpentine flow pattern, the fit algorithm performs noticeable matching to the AFD profile. The resulting code takes around 2 minutes in a standard PC to compute the optimal aim points for a field made up of 2650 heliostats.

Contents

List of Figures

List of Tables

List of publications

Part of the work presented in this thesis has been published in refereed journal articles:

- A. Sánchez-González, D. Santana
  Solar flux distribution on central receivers: A projection method from analytic function.
  Renewable Energy, 74 (2015) 576-587.
- A. Sánchez-González, C. Caliot, A. Ferrière, D. Santana
  Determination of heliostat canting errors via deterministic optimization.
  Solar Energy, 150 (2017) 136-146.
- A. Sánchez-González, M.R. Rodríguez-Sánchez, D. Santana
  Aiming strategy model based on allowable flux densities for molten salt central receivers.
  Solar Energy (2016) In press `http://dx.doi.org/10.1016/j.solener.2015.12.055`

CHAPTER

ONE

General introduction

Contents

Summary

Research in concentrating solar power and renewable energy, in the broadest sense, is needed for two main reasons. On one hand, the environmental impact associated to non-renewable energy sources and, on the other hand, the progressive depletion of fossil fuel reserves. Concentrating solar power is one of the clean technologies that are intended to gradually replace non-renewable energy sources.

This work lays in the framework of solar central receiver systems (CRS), and, more specifically, in the development of models to accurately simulate the interaction between heliostat field and central thermal receiver. An introduction to these topics is dealt in the following. At the end of this introductory Chapter, the objectives of the thesis are formulated and its structure is outlined.

1.1 Concentrating solar power technologies

In Concentrating Solar Power (CSP) systems, solar radiation is concentrated by mirrors and the final output is, usually, electric power. Leaving aside thermochemical processes where other products are obtained (e.g. hydrogen production, water desalinization...), solar concentrated energy can be converted to electricity in two ways: 1) direct conversion by means of photovoltaic effect, namely concentrating photovoltaic (CPV); and, 2) indirect conversion with intermediate transformation into thermal energy. This thesis is concerned with the second alternative. Concentrated solar radiation is transferred into a heat transfer fluid (HTF) from which mechanical energy is extracted and, eventually, electricity is produced.

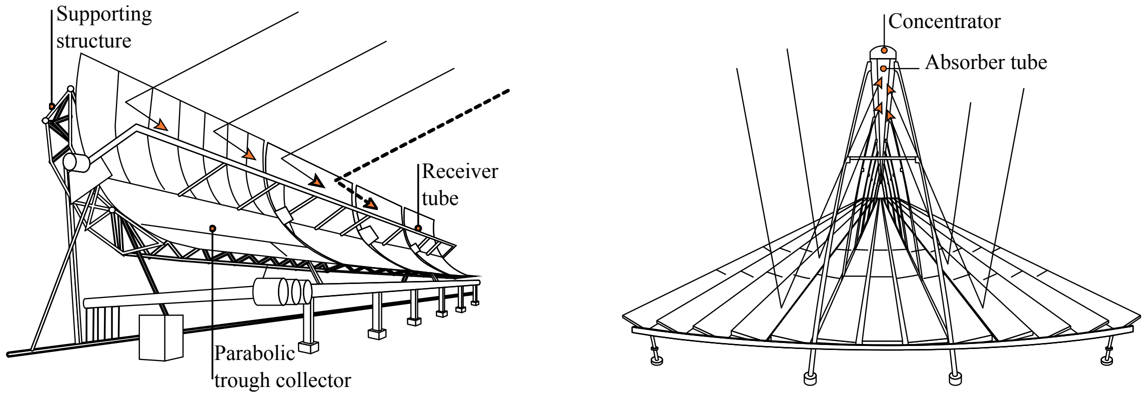

(a) Parabolic trough collector.

(b) Linear Fresnel reflector.

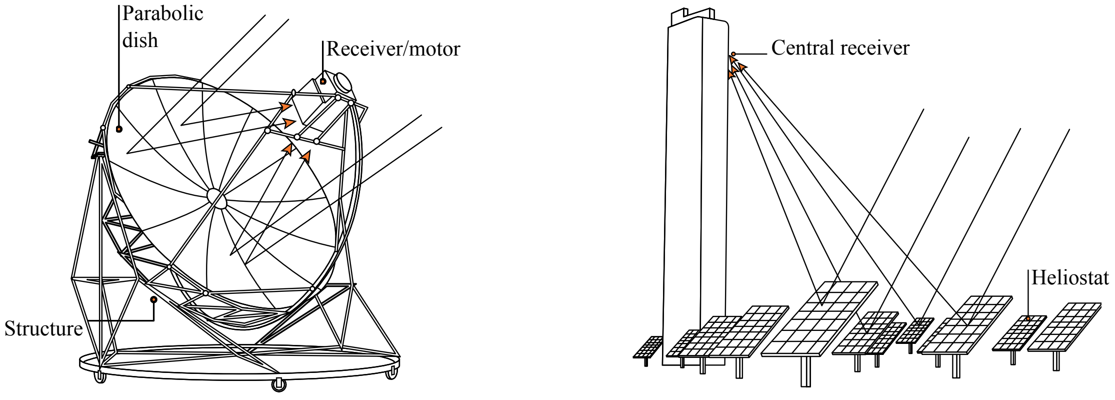

(c) Parabolic dish.

(d) Central receiver system.

Figure 1.1: CSP technologies. Adapted from SolarConcentra (2013).

Depending on the way in which solar direct radiation is concentrated, CSP can be classified into four different technologies. They are, in order of current deployment level (Lovegrove & Stein, 2012): parabolic trough, central receiver tower, linear Fresnel and parabolic dish. Key performance parameters for each of these CSP technologies are given on Table 1.1. Figure 1.1 sketches these four technologies that are briefly described in the following.

Table 1.1: Comparison of CSP technologies (Kalogirou, 2009; Romero-Alvarez & Zarza, 2007)

CSP technology	Tracking	Concentration	Capacity size [MW]	Solar-electric efficiency [%]
Parabolic trough	one axis	70-80	30-80	10-15
Linear Fresnel	one axis	25-100	30-80	9-11
Parabolic dish	two axes	1000-3000	0.005-0.025	16-18
Central receiver	two axes	300-1000	10-200	8-10

- **Parabolic trough collector** (PTC) consists of a parabolic trough mirror in whose focus is placed a linear receiver, where beam sunlight is concentrated. Sun movement is tracked on one axis, elevation axis. Depending on the orientation of the rotation axis, there are basically two configurations of PTC: north-south and east-west.

- **Linear Fresnel reflector** (LFR) shares the same principle as PTC, but instead of a continuous parabolic mirror, it is made up of strips of flat or slightly curved mirrors parallel to the linear receiver. Concentration ratio ranges in LFR are similar to PTC (Table 1.1), but LFR is optically less efficient, mainly because of shading and blocking effects.
- **Parabolic dish** is a small scale point-focus system. It is made up of a single paraboloidal mirror (dish) and a receiver placed in its focal point. A Stirling engine is usually mounted in the receiver, so that this system is commonly referred to as dish Stirling (DS).
- **Central receiver system** (CRS) consists of a field of heliostats that concentrates beam radiation into a central receiver. The thermal receiver is usually mounted at the top of a tower, reason why this technology is also called Solar Power Tower (SPT).

This work is confined to CRS technology, which is further described in the following Subsection. The terms solar power tower (SPT) and central receiver system (CRS) are used interchangeably to refer the same technology (Vant-Hull, 2012).

1.1.1 Solar power tower

Origins of SPT date back to mid 20^{th} century. First edition of *Solar Energy* journal in 1957 opened with the feasibility study of a solar plant consisting in 1293 movable mirrors to be located in the Soviet Union (Baum *et al.*, 1957).

A couple of decades later, coinciding with the first oil crisis, in USA and Europe awoke interest in SPT (Hildebrandt & Vant-Hull, 1977). USA began the construction in Mojave Desert of Solar One pilot plant, that was completed in 1981. The plant was made up of a field of 1818 heliostats and a central superheated steam receiver. In 1995 Solar One was reconverted into Solar Two, where the central receiver was changed into another using molten salt as HTF. Demonstration CRS projects were also built in that period in Europe: THEMIS in Targassonne (France); and SSPS and CESA-1 in PSA, Tabernas (Spain).

As a result of these demonstration projects, many publications and technical reports have arisen in the scientific community. A good example of open access to technical reports is given by SANDIA National Laboratories that, for instance, have shared the lessons learned from Solar Two project (Litwin & Park, 2002; Pacheco, 2002).

Commercial SPT plants started deployment at the beginning of this century. One of the most representative projects has been built in Spain; the plant, named Gemasolar, uses a molten salt central receiver and has 15 hours of thermal storage capacity (Lata *et al.*, 2010). Other recent emblematic projects are Crescent Dunes and Ivanpah, both of them located in USA.

From the functional point of view, a SPT plant is made up of four subsystems: heliostat field, central receiver, thermal energy storage and power block. These four subsystems are represented in Figure 1.2.

The heliostat field consists of an array of tracking mirrors that concentrate beam sunrays onto the receiver. Heliostats track the sun in two axes, commonly azimuth and elevation. Alternative heliostats perform spinning and elevation tracking (Chen *et al.*, 2004).

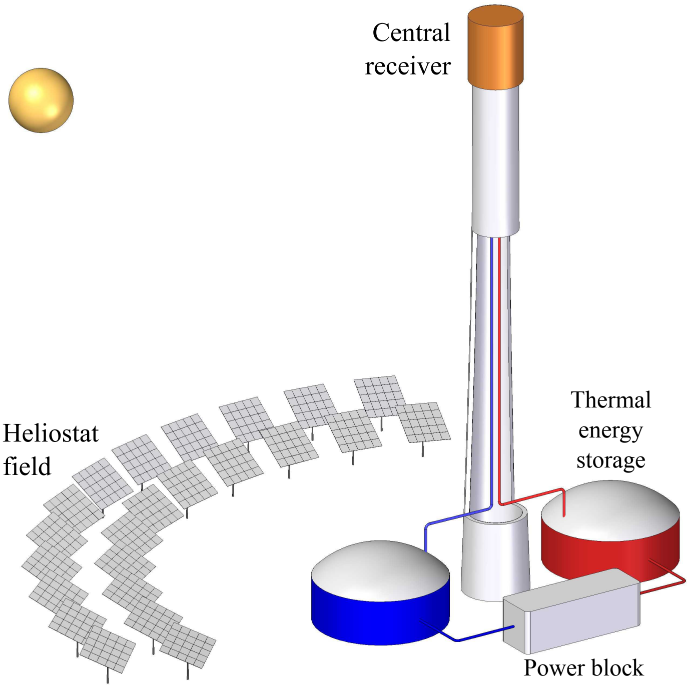

Figure 1.2: Solar power tower plant.

The thermal receiver is mounted on the top a central tower, Figure 1.2; or, alternatively, on the ground in case of beam down optics with a secondary concentrator. An initial classification of thermal receivers is performed depending on the phase of the heat transfer fluid (HTF) either gas or liquid (Ho & Iverson, 2014). The most common gas receiver is the air volumetric absober that takes advantage of the so-called volumetric effect. On the other hand, liquid (and steam) receivers adopt the form of tubular receivers.

Tubular receivers consist of an array of thin-walled tubes through which the HTF flows. This kind of receiver is usually made up of flat panels consisting in an array of tubes connected in parallel by top and bottom headers. At the same time, these panels are connected between them in series, and, optionally, in parallel if more than one flow path is required. External tubular receivers adopt two basic geometries: flat (single panel or billboard) and cylindrical. In internal tubular cavity receivers, the panels are contained in an insulating enclosure with an glazed aperture to the field.

The main layout of the heliostat field is dictated by the type of central receiver, that sets the opening angle. Flat receivers oriented to the north (in northern hemisphere) lead to north fields; the same can be said for single cavity receivers. On the contrary, cylindrical receivers demand surround heliostat fields. To take advantage of heliostats oppositely located to the sun, which have better incidence angles, these heliostat fields are biased to the north (in northern hemisphere).

Regarding HTFs, six different groups are identified (Vignarooban *et al.*, 2015): water/steam, molten salt, thermal oil, organics, liquid metals and gases/air. Required HTF characteristics are: high thermal conductivity, low melting point, high boiling point, low viscosity and low corrosion. In this regard, the most common HTF in CRS are water/steam and molten salt. The latter has a high heat capacity suitable for thermal storage purposes, however molten salts are corrosive.

The third SPT subsystem is thermal energy storage (TES), which is optional depending on whether collected energy in the HTF is stored or not. TES allows electricity production in the absence of instantaneous solar radiation (i.e. existence of clouds and at night). CRS using molten salt as HTF take advantage of the TES. Figure 1.2 depicts the cold (blue) and hot (red) tanks correspondingly arranged before and after the HTF passes through the receiver.

The power block (PB) constitutes the last subsystem in a SPT plant; grey box in Figure 1.2. In the PB, thermal energy from the HTF is converted into mechanical energy in a turbine joined to an alternator to generate electricity. In the event of molten salt receivers, the PB includes a heat recovery steam generator that transfers heat from the HTF to the feeding water. Depending on the HTF, a steam or a gas turbine is utilized to operate the corresponding Rankine or Brayton thermodynamic cycle.

1.2 Optical modeling tools for SPT

Since the beginning of solar power tower technology, several simulation models have been developed. This Section contains a brief review of existing tools for optical modeling of the flux distribution on central receivers. A first classification of optical tools for SPT is done on the basis of their final objective, namely:

- Performance tools, aimed to determine the flux distribution incident on central receivers.
- Optimization tools, aimed to design the heliostat field and, presumably, the receiver.

The calculation of the flux distribution on central receiver carried out by performance tools can be classified in two categories, depending on the underlying methodology. According to Garcia *et al.* (2008), these two approaches are:

- Monte Carlo Ray Tracing (MCRT)
- Convolution

In the following, these two methodologies are described.

1.2.1 MCRT approach

MCRT is a statistical method that traces a bundle of random rays. Specifically in SPT, a large number of rays are traced from the sun following a solar distribution (i.e. sunshape), typically Gaussian or pillbox. Incoming rays are reflected by the heliostat mirrors. Collision of reflected rays in the receiver surface are accounted for to generate the flux map. Alternatively to MCRT based on collisions, an integral formulation has been established (Galtier *et al.*, 2013). Because of the randomness associated to MCRT, accuracy and level of resolution are directly proportional to the number of traced rays.

MIRVAL (Leary & Hankins, 1979) was the first code using the MCRT approach. Four of the currently most popular MCRT tools for SPT are: SolTrace, Tonatiuh, Stral and Solfast. Except for Stral, the remaining tools have been developed to optically simulate all kinds of CSP technologies. Table 1.2 lists the

Table 1.2: MCRT tools for CSP.

	SolTrace	Tonatiuh	Stral	Solfast 4D
Developer	NREL	CENER	DLR	CNRS & HPC-SA
Reference	(Wendelin, 2003)	(Blanco *et al.*, 2005)	(Belhomme *et al.*, 2009)	(Roccia *et al.*, 2012)
Formulation	Based on collisions	Based on collisions	Based on collisions	Integral
Programming language	Delphi5	C++	C++	-
Availability	Freeware	Source code	Proprietary	Proprietary
CSP technologies	CRS, PT, DS	CRS, PT, DS	CRS	CRS, PT, DS

characteristics of these four MCRT codes. A recent and complete list of modeling tools for SPT can be found in (Li *et al.*, 2016).

SolTrace and Tonatiuh are open access tools respectively developed by NREL and CENER. The former was used in this study to validate the model developed in Chapter 2. Contrary to the rest, Solfast uses an integral formulation that boosts convergence (Piaud *et al.*, 2012).

Computational cost associated to MCRT technique is high, both in terms of time and memory resources. Besides, solution exactitude is proportional to such computational cost. These factors restrict the usage of MCRT tools to performance studies, where time is not a limiting factor.

1.2.2 Convolution approach

Convolution-based models ground on the superposition, convolution, of the mathematical functions that rule these optical systems. To obtain the direct flux density, F, on a plane the superposed functions are: concentration function, CF; solar distribution or sunshape, S; and optical errors, E. Mathematically the convolution of these three function can be expressed as:

$$F(x, y) = CF * S * E \tag{1.1}$$

Functions S and E are usually modeled as circular Gaussian distributions, since this distribution emulates adequately the physical reality and the convolution operation is achievable using such normal distribution. On the other hand, the concentration function CF is usually a constant depending on the cosine of the incidence angle on the heliostat mirror, ω_h.

Early models based on the convolution approach were developed at the end of the 70's decade. Initial models presumed flat surface of the mirrors (Lipps & Walzel, 1978), likewise first heliostat prototypes. Later, with the arrival of focusing heliostats, models have taken into account the curvature of the mirrors.

To date, several models based on the convolution approach have been developed. They differ between them in the way the convolution is worked out. HELIOS model (Biggs & Vittitoe, 1979) solved by means of the fast Fourier transform the two-dimensional convolution along the discretized mirror surface. Results from HELIOS are very precise, but computation time is similar to MCRT.

Table 1.3: Models for CRS based on convolution.

	UNIZAR	DELSOL	HFLCAL
Developer	UNIZAR	SNL	DLR
Reference	(Collado *et al.*, 1986)	(Kistler, 1986)	(Schwarzbözl *et al.*, 2009)
Convolution	Analytic integration	Hermite function expansion	Simplified convolution
Programming language	Matlab	Fortran/Basic	-
Availability	No	Source code. Embedded in SAM	No
Receiver type	Flat	Flat, cavity, cylindrical	Flat

Three of the currently most known models are UNIZAR, DELSOL and HFLCAL, whose characteristics are pointed out in Table 1.3.

Collado *et al.* (1986) solved the convolution through analytic integration on the plane of the receiver, and also the image plane, achieving an analytic function. This model, named UNIZAR (Collado, 2010), is partially adopted in the present work, as will be shown in the next Chapter.

DELSOL uses analytic integration in one axis and, in the other, numeric integration by means of Hermite polynomial expansion, originally described in (Walzel *et al.*, 1977). Unlike UNIZAR, DELSOL code allows the three types of receiver geometry: flat, cavity and cylindrical. DELSOL source code is open access. Moreover, DELSOL model is implemented in System Advisor Model (SAM), which is a general purpose software tool for CSP simulation (Blair *et al.*, 2014).

Thirdly, HFLCAL makes use of an analytic function which is literally a circular Gaussian distribution. HFLCAL includes in its formulation the sources of astigmatic aberration.

As a general rule, convolution models are faster than those based in MCRT, which makes convolution codes more appropriate for optimization purposes. These models entail errors around 1-2% in the peak flux density and significant errors in the calculation of spillage losses (Walzel *et al.*, 1977; Garcia *et al.*, 2008).

Analytic functions (e.g. UNIZAR and HFLCAL) have been developed for a single flat surface, while their extension to other geometries (i.e. cavity and cylinder) remains pending. Such extension has motivated a part of the research work collected in this thesis.

1.3 Scope of the thesis

This dissertation presents a work essentially focused on the modeling of flux mapping and aiming strategies for central receivers.

The key objectives of the Ph.D. thesis are:

- Build and validate a model to map the flux incident on central receivers, both flat and cylindrical. Model requirements are accuracy and computation speed.
- Develop and validate a methodology to determine canting errors from heliostat flux images measured on a target. Optimization techniques are utilized to computationally find canting errors.
- Carry out an aiming strategy model to generate different patterns of flux maps, including fairly uniform distributions as well. Single parameter control of spillage losses is pursued.
- Develop a heliostat field aiming strategy for molten salt cylindrical receivers to maximize receiver thermal output, while carefully meeting corrosion and thermal stress limits.

1.3.1 Outline of the dissertation

The objectives set above are addressed in this document. The remainder of the dissertation is organized as follows.

Chapter 2 presents a methodology to calculate the flux distribution from a single heliostat on central a receiver, either flat or cylindrical. The method is based on the projection from the image plane onto the receiver surfaces. On the image plane, it is taken an analytic function resulting from the convolution approach (e.g. UNIZAR, HFLCAL). An expression to compute the intercept factor is provided. The model is validated against experimental PSA measurements and MCRT simulations in SolTrace. Besides, computational cost is compared with that in the latter tool.

In Chapter 3, the model developed in the previous Chapter is applied to find canting errors in real heliostats. From flux images taken on the target of THEMIS plant, an optimization procedure to find out alignment errors in selected CETHEL heliostats in THEMIS field is developed and validated.

The model described in Chapter 2 for a single heliostat is extended in Chapter 4 to generate flux maps from an entire field of heliostats. Optical losses are accounted for and special attention is paid to the calculation of shading and blocking areas in the mirrors. Besides the single aiming strategy, a methodology to generate symmetric flux maps is carried out. The model is build upon a single control parameter.

Chapter 5 exposes a full aiming strategy devoted to molten salt cylindrical receivers. This model, partially constructed on the preceding strategy, maximizes the flux incident on the receiver, while preserving molten salt receiver requirements; i.e. corrosion and thermal stress limitations. An allowable flux density approach is developed and a detailed thermal model of molten salt receivers is incorporated. From *ad hoc* algorithms, an automated code is implemented to determine heliostat target points; resulting flux maps are also generated.

Finally, conclusions are summarized in Chapter 6.

Nomenclature

CF	Concentration function	S	Solar distribution, sunshape
E	Optical errors	ω_h	Incidence angle on the heliostat [rad]
F	Flux density [W/m^2]		

Acronyms

CENER	Centro Nacional de Energías Renovables
CNRS	Centre National de la Recherche Scientifique
CPV	Concentrating Photovoltaic
CRS	Central Receiver System
CSP	Concentrating Solar Power
DLR	Deutsches Zentrum für Luft- und Raumfahrt
DS	Dish Stirling
HTF	Heat Transfer Fluid
LFR	Linear Fresnel Reflector
MCRT	Monte Carlo Ray Tracing
NREL	National Renewable Energy Laboratory
PB	Power Block
PSA	Plataforma Solar de Almería
PTC	Parabolic Trough Collector
SNL	Sandia National Laboratories
SPT	Solar Power Tower
TES	Thermal Energy Storage
UNIZAR	Universidad de Zaragoza

References

BAUM, V. A., APARASI, R. R. & GARF, B. A. 1957 High-power solar installations. *Solar Energy* 1 (1), 6–12.

BELHOMME, B., PITZ-PAAL, R., SCHWARZBÖZL, P. & ULMER, S. 2009 A New Fast Ray Tracing Tool for High-Precision Simulation of Heliostat Fields. *Journal of Solar Energy Engineering* 131.

BIGGS, F. & VITTITOE, C. N. 1979 Helios model for the optical behavior of reflecting solar concentrators. *Tech. Rep.*. Sandia National Laboratories, SAND-76-0347.

BLAIR, N., DOBOS, A. P., FREEMAN, J., NEISES, T., WAGNER, M., FERGUSON, T., GILMAN, P. & JANZOU, S. 2014 System advisor model, SAM 2014.1. 14: General description. *Tech. Rep.*. NREL & DoE, TP-6A20-61019.

BLANCO, M. J., AMIEVA, J. M. & MANCILLAS, A. 2005 The tonatiuh software development project: An open source approach to the simulation of solar concentrating systems. In *ASME Conference Proceedings*. ASME.

CHEN, Y., KRIBUS, A., LIM, B., LIM, C., CHONG, K., KARNI, J., BUCK, R., PFAHL, A. & BLIGH, T. P. 2004 Comparison of Two Sun Tracking Methods in the Application of a Heliostat Field. *Journal of Solar Energy Engineering* 126 (1), 638.

COLLADO, F. J. 2010 One-point fitting of the flux density produced by a heliostat. *Solar Energy* 84 (4), 673–684.

COLLADO, F. J., GÓMEZ, A. & TURÉGANO, J. 1986 An analytic function for the flux density due to sunlight reflected from a heliostat. *Solar Energy* 37 (3), 215–234.

GALTIER, M., BLANCO, S., CALIOT, C., COUSTET, C., DAUCHET, J., EL HAFI, M., EYMET, V., FOURNIER, R., GAUTRAIS, J., KHUONG, A., PIAUD, B. & TERRÉE, G. 2013 Integral formulation of null-collision Monte Carlo algorithms. *Journal of Quantitative Spectroscopy and Radiative Transfer* 125, 57–68.

GARCIA, P., FERRIÈRE, A. & BEZIAN, J.-J. 2008 Codes for solar flux calculation dedicated to central receiver system applications: A comparative review. *Solar Energy* 82 (3), 189–197.

Hildebrandt, A. F. & Vant-Hull, L. L. 1977 Power with Heliostats. *Science* 197 (4309), 1139–1146.

Ho, C. K. & Iverson, B. D. 2014 Review of high-temperature central receiver designs for concentrating solar power. *Renewable and Sustainable Energy Reviews* 29, 835–846.

Kalogirou, S. A. 2009 Solar Thermal Power Systems. In *Solar Energy Engineering: Processes and Systems*, chap. 10, pp. 521–552. Elsevier.

Kistler, B. 1986 A user's manual for DELSOL3: Computer code for calculating the optical performance and optimal system design for solar thermal central receiver plants. *Tech. Rep.*. Sandia National Laboratories, SAND-86-8018.

Lata, J. M., Alcalde, S., Fernández, D. & Lekube, X. 2010 First surrounding field of heliostats in the world for commercial solar power plants - Gemasolar. *Proceedings of SolarPACES* .

Leary, P. L. & Hankins, J. D. 1979 User's guide for MIRVAL: a computer code for comparing designs of heliostat-receiver optics for central receiver solar power plants. *Tech. Rep.*. Sandia National Laboratories, SAND-77-8280.

Li, L., Coventry, J., Bader, R., Pye, J. & Lipiński, W. 2016 Optics of solar central receiver systems: a review. *Optics Express* 24 (14).

Lipps, F. W. & Walzel, M. D. 1978 An analytic evaluation of the flux density due to sunlight reflected from a flat mirror having a polygonal boundary. *Solar Energy* 21 (2), 113–121.

Litwin, R. Z. & Park, C. 2002 Receiver System : Lessons Learned from Solar Two. *Tech. Rep.* March. Sandia National Laboratories.

Lovegrove, K. & Stein, W. 2012 Introduction to concentrating solar power (CSP) technology. In *Concentrating Solar Power Technology*, chap. 1, pp. 3–15. Woodhead Publishing - Elsevier.

Pacheco, J. E. 2002 Final Test and Evaluation Results from the Solar Two Project. *Tech. Rep.* January. Sandia National Laboratories, SAND2002-0120.

Piaud, B., Coustet, C., Caliot, C., Guillot, E. & Flamant, G. 2012 Application of Monte-Carlo sensitivities estimation in Solfast-4D. In *SolarPACES*.

Roccia, J. P., Piaud, B., Coustet, C., Caliot, C., Guillot, E., Flamant, G. & Delatorre, J. 2012 SOLFAST, a Ray-Tracing Monte-Carlo software for solar concentrating facilities. *Journal of Physics: Conference Series* 369, 012029.

Romero-Alvarez, M. & Zarza, E. 2007 Concentrating Solar Thermal Power. In *Handbook of Energy Efficiency and Renewable Energy*, , vol. 20070849, chap. 21, pp. 21.1–21.97. Taylor and Francis Ltd.

Schwarzbözl, P., Schmitz, M. & Pitz-paal, R. 2009 Visual HFLCAL - A software tool for layout and optimisation of heliostat fields. In *SolarPACES*. Berlin, Germany.

SolarConcentra 2013 Identificación de las principales líneas de investigación en el sector de la electricidad termosolar. *Tech. Rep.*. Solar Concentra.

Vant-Hull, L. L. 2012 Central tower concentrating solar power (CSP) systems. In *Concentrating solar power technology: principles, developments and applications*, chap. 8. Woodhead Publishing - Elsevier.

VIGNAROOBAN, K., XU, X., ARVAY, A., HSU, K. & KANNAN, A. 2015 Heat transfer fluids for concentrating solar power systems: A review. *Applied Energy* 146, 383–396.

WALZEL, M. D., LIPPS, F. W. & VANT-HULL, L. L. 1977 A solar flux density calculation for a solar tower concentrator using a two-dimensional Hermite function expansion. *Solar Energy* 19 (3), 239–253.

WENDELIN, T. 2003 SolTRACE: a new optical modeling tool for concentrating solar optics. In *ISEC*. ASME.

CHAPTER

TWO

Flux distribution from a single heliostat: projection method

Contents

Summary

This Chapter presents a methodology to project the flux distribution produced by a heliostat from the image plane into the panels of any central receiver in Solar Power Tower plants. Since analytic functions derived from the convolution approach are conveniently defined on the image plane, its oblique projection solves the distorted spot found in actual receivers. Because of its accuracy describing the flux distribution due to rectangular focusing heliostats, the analytic function on the image plane by Collado *et al.* (1986) is used along this dissertation. Based on the projection method, a computer code was developed and validated against SolTrace simulations and measurements at Plataforma Solar de Almería. The projection methodology was successfully implemented for both flat plate and multi-panel cylindrical receivers. The validated model overcomes the computation time limitation associated to Monte Carlo Ray Tracing technique.

2.1 Introduction

In Central Receiver Systems (CRS), thousands of heliostats reflect the direct solar radiation into the receiver. System design and optimization demand not only fast, but also accurate models to perform optical calculations. On the receiver surface, the distribution of flux density or its concentration ratio becomes the key outcome of these optical tools.

Existing models are divided into two categories (Garcia *et al.*, 2008): Monte Carlo Ray Tracing (MCRT) and convolution methods. The first one is a statistical approach that traces a bundle of random rays from the sun. The more rays are traced the higher precision is achieved, but also higher computational cost; unaffordable for design and optimization studies. On the other hand, convolution methods rely on the mathematical superposition of error cones, namely: sunshape, concentration and mirror errors. While several approaches have been proposed to solve the convolution integral, all of them are faster than MCRT techniques.

Numerical resolution of the convolution integral with Fourier transform has been implemented in HELIOS code (Biggs & Vittitoe, 1979). Such resolution is highly accurate, but not fast enough for system design; at least, with late 20^{th} century computers. Otherwise, the convolution integral can be solved analytically under certain assumptions, leading to an analytic expression for the flux density on the image plane; expressions which are faster to evaluate. Lipps & Walzel (1978) found an exact analytic result for flat, i.e. non-focusing, polygonal heliostats. Similarly, by means of analytic integration over a linearly mapped domain, Collado *et al.* (1986) obtained an analytical expression based on the error function, which is suitable for rectangular focused heliostats. This last model has been recently named UNIZAR (Collado, 2010).

Other authors have found approximate solutions for the flux density on the image plane. Assuming Gaussian behavior for all error cones, a single circular normal distribution has been proposed (Schwarzbözl *et al.*, 2009). Unlike other models, this simplified one can handle the astigmatism effect produced by off-axis aberration. The circular normal distribution has been implemented in HFLCAL code, which performs either optical or optimization simulations.

Walzel *et al.* (1977) proposed a sixth order Hermite polynomial to represent the flux density on the image plane from flat heliostats. Its precision increases for small and distant heliostats. For focusing heliostats, a faceted heliostat composed of flat canted mirrors can be considered. Walzel's function has been implemented in DELSOL3 code (Kistler, 1986), that takes a representative heliostat for each field sector, thus decreasing considerably computation time. In addition to optical performance calculations, DELSOL3 carries out optimization analysis scaling results from the performance run.

There remains a need for models to accurately predict the solar flux density on actual cylindrical receivers caused by focusing heliostats. Since analytic functions are adequately defined on the image plane, the present Chapter proposes an oblique projection onto the receiver panels. This way, the heliostat image shape can be appropriately distorted. The analytic function on the image plane by UNIZAR was adopted because of its accurate distribution of the solar flux density reflected by rectangular focusing heliostats.

A computer code was developed based on the oblique projection methodology, which is described in the following Section. Then, the model is first validated for flat plate receivers and secondly for cylindrical receivers, using experimental flux distributions and MCRT simulations.

2.2 Model based on projection

Analytic functions are usually defined on the plane normal to the central reflected ray; taking the target point as the origin of coordinates. That plane, named image plane, hardly coincides with any receiver plane. Therefore an appropriate transformation is claimed, namely oblique projection.

In the present Chapter, it is proposed a methodology to project the solar flux density distribution from the image plane onto the receiver surfaces. The suggested procedure, represented in Figure 2.1, consists in the following four steps:

1. Receiver panels are discretized in a mesh of equally spaced nodes.
2. Mesh nodes are projected onto the image plane in the direction of the central reflected ray.
3. The analytic function is evaluated at the nodes in the image plane.
4. Flux density at image nodes is multiplied by the cosine of the incidence angle on the receiver.

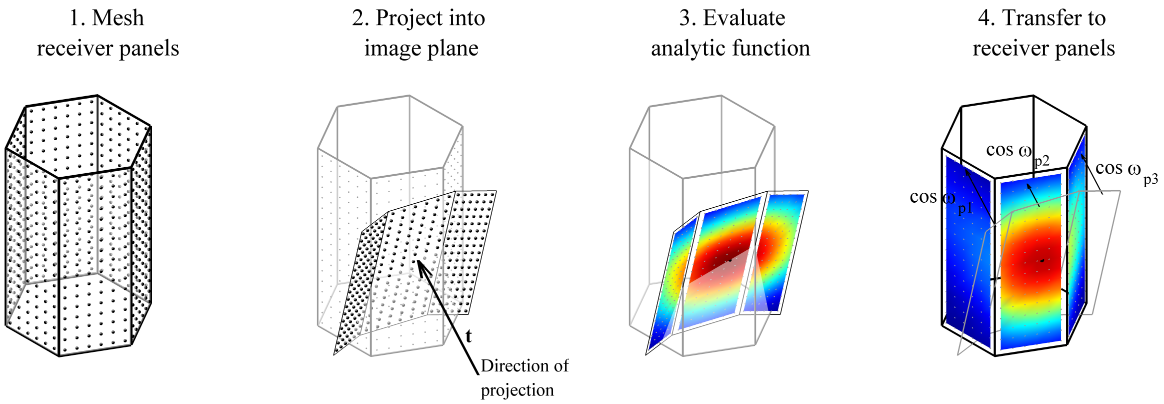

Figure 2.1: Projection methodology.

Since the ultimate goal is to project the flux distribution from the image plane to the receiver, an alternative procedure could be argued: first discretize the image plane and then project onto the receiver. Although the same goal is achieved, the proposed method offers several advantages. The discrete domain is strictly limited to the surfaces of interest, avoiding useless nodes. A unique mesh for the receiver also facilitates the sum of fluxes from a whole field of heliostats.

The proposed model and, particularly, the projection step lead to three-dimensional geometric transformations, involving operations with vectors and matrices. A computer code, implemented in Matlab®, deals with all types of central receivers made up of flat panels, either cylindrical or flat plate. Cylindrical receivers consist of any number of panels arranged in a cylindrical shell. Figures in this Section correspond to a receiver of six panels. Obviously, the methodology herein described also applies to flat plate and cavity receivers.

A formulation based on the concentration ratio of flux density, C, is advantageous. This dimensionless parameter can be seen as the number of suns impinging on the receiver, regardless of the instantaneous solar insolation. Strictly speaking, the concentration of flux density is the ratio of flux density, F, on the receiver to the direct normal irradiance, DNI, incident on the heliostat field.

$$C = \frac{F}{DNI} \tag{2.1}$$

In this Section, the four steps of the suggested procedure are described in detail. Prior to that, various coordinate systems are defined. The computation of spillage losses is presented at the end of current Section.

2.2.1 Coordinate systems and transformations

The global system of coordinates (denoted as sg) has its origin G in the base of the tower at ground level. The positive X_{sg} axis points east and the positive Y_{sg} axis points north. As left handed coordinate system, the positive Z_{sg} axis is directed to the zenith.

Other Cartesian coordinate systems are locally placed. At each specific target point T on the receiver, a coordinate system (st) is defined. The $X_{st}Y_{st}$ plane is taken coplanar with the target panel, where the X_{st} axis is horizontal, the Y_{st} axis is vertical and the Z_{st} axis is outward normal to the panel. Also in T, a coordinate system referenced to the image plane (si) is set, as will be introduced in Subsection 2.2.3.

For each heliostat, a coordinate system (sh) is defined with origin in the mirror center H. The $X_{sh}Y_{sh}$ plane corresponds to the plane of the mirror and the Z_{sh} axis is outward normal to the mirror plane. For conventional rectangular heliostats with azimuth-elevation tracking, the Y_{sh} axis is parallel to the sides of the mirror and the X_{sh} axis remains horizontal as elevation axis.

Figure 2.2 illustrates the systems of coordinates above mentioned. Throughout this Chapter, **u**, **v** and **w** stand for the unit vectors in the positive directions of X, Y and Z axes, respectively. Subscripts indicate the corresponding coordinate system.

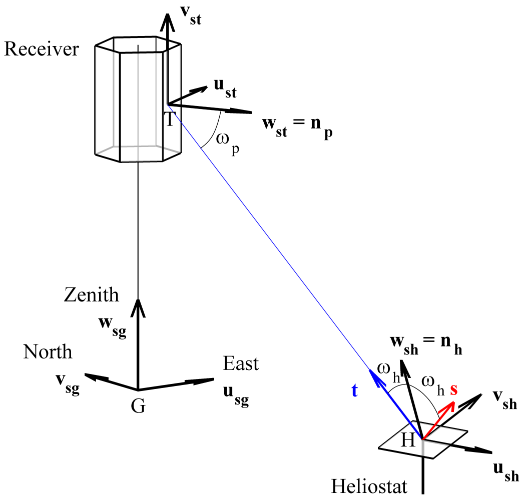

Figure 2.2: Systems of coordinates.

The unit vector **s** points to the sun and is computed with Equation (2.2). Solar azimuth and elevation angles, α_{sun} and ϵ_{sun}, depend on solar time and site latitude. Unless otherwise specified, in this thesis solar position is calculated with the formulae stated in Braun & Mitchell (1983), in turn based on Cooper (1969) equation for the solar declination.

$$\mathbf{s} = \frac{\mathbf{S}}{|\mathbf{S}|}, \quad \textit{where} \quad \mathbf{S} = \begin{bmatrix} -\sin\alpha_{sun}\cdot\cos\varepsilon_{sun} \\ -\cos\alpha_{sun}\cdot\cos\varepsilon_{sun} \\ \sin\varepsilon_{sun} \end{bmatrix} \tag{2.2}$$

For a given heliostat with mirror center in H, $\mathbf{t}$ is the unit vector directed toward the aim point T. Thus, vector $\mathbf{t}$ is in the direction of the central reflected ray. According to Snell's law of reflection, the incident angle on the mirror equals the angle of reflection (ω_h). Then, the bisector of $\mathbf{s}$ and $\mathbf{t}$ is the heliostat normal ($\mathbf{n}_h$), which coincides with $\mathbf{w}_{sh}$.

$$\mathbf{n}_h = \frac{\mathbf{s}+\mathbf{t}}{|\mathbf{s}+\mathbf{t}|} = \mathbf{w}_{sh} \tag{2.3}$$

An appropriate transformation from the global system of coordinates (sg) to the heliostat coordinate system (sh) can be defined. Such a transformation comprises the translation from G to H and two consecutive rotations: azimuth and elevation. The heliostat azimuth angle, α_h, is zero for south orientation and positive in clockwise rotation, as shown in Figure 2.3. The elevation angle, ε_h, is relative to the horizontal projection of the heliostat normal. Mathematically, the transformation from global to heliostat coordinates is expressed through the following matrix Equation:

$$\begin{bmatrix} x \\ y \\ z \end{bmatrix}_{sh} = \begin{bmatrix} \cos\alpha_h & -\sin\alpha_h & 0 \\ \sin\alpha_h\cdot\sin\varepsilon_h & \cos\alpha_h\cdot\sin\varepsilon_h & \cos\varepsilon_h \\ -\sin\alpha_h\cdot\cos\varepsilon_h & -\cos\alpha_h\cdot\cos\varepsilon_h & \sin\varepsilon_h \end{bmatrix} \begin{bmatrix} x-H_x \\ y-H_y \\ z-H_z \end{bmatrix}_{sg} \tag{2.4}$$

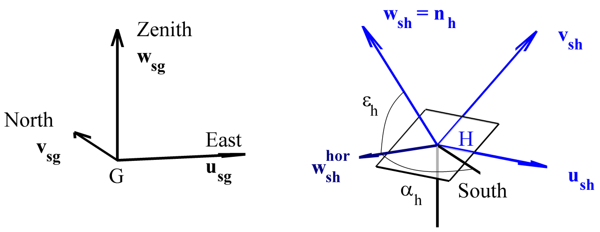

Figure 2.3: Transformation from global to heliostat coordinate system.

External receivers are made of a number p of flat panels. A practical way of numbering the receiver panels is convenient. Figure 2.4 shows the panels counterclockwise numbered starting from the south. The computer code allows any number of panels for the receiver, even single flat plate receiver.

For a given aim point T, another transformation from global (sg) to local (st) system of coordinates can be defined. Such a transformation comprises the translation from G to T and a rotation of angle α_{pt}, which is the azimuth angle of the target panel. In matrix notation, this transformation is equivalent to the following Equation:

$$\begin{bmatrix} x \\ y \\ z \end{bmatrix}_{st} = \begin{bmatrix} \cos\alpha_{pt} & \sin\alpha_{pt} & 0 \\ 0 & 0 & 1 \\ \sin\alpha_{pt} & -\cos\alpha_{pt} & 0 \end{bmatrix} \cdot \begin{bmatrix} x-T_x \\ y-T_y \\ z-T_z \end{bmatrix}_{sg} \tag{2.5}$$

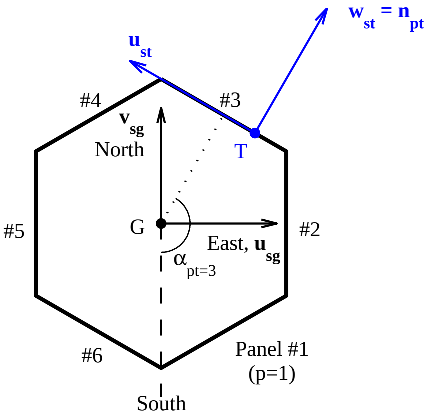

Figure 2.4: Transformation from global to target coordinate system and numeration order of panels. Receiver top view.

Once the reference systems of coordinates is established, the steps of the proposed model can be described in detail.

2.2.2 Receiver discretization

The first step of the suggested procedure (Figure 2.1) is the discretization of the receiver surfaces, prior to its projection onto the image plane. Each receiver panel is discretized in a grid of nodes equally spaced. As schematically is illustrated in Figure 2.5, the nodal spacing along horizontal and vertical directions is Δx and Δy, respectively. Because of geometric constrains, Δx and Δy cannot usually be exactly the same, although they approximate as much as possible ($\Delta x \approx \Delta y$). As usual, the finer the grid, the level of resolution increases, but also the computation time.

Since nodes placed in the edge of two panels would belong to both, such lack of determination is avoided. In practice, each node in the mesh is located in the center of a cell whose area is equal to $\Delta x \Delta y$.

Every single node can be identified by indices $[i, j, p]$. The last p index represents the number of panel, following the counterclockwise numbering previously introduced. Indices i and j stand for the row and column position, respectively. For convenience, $[i, j, p]$ indices start from the bottom left corner of each panel.

Following the order described above, a 3D matrix is created for any parameter of interest. Then, the value in each node is stored at its corresponding position in the matrix. When referring to the concentration ratio of flux density, C, in a generic node, the following notation is used: $C_{i,j,p}$.

2.2.3 Mesh projection

The projection step is the core of the present model. The projection of the receiver mesh is performed from the receiver itself to the image plane, which is perpendicular to the central reflected ray with $\mathbf{t}$ unit vector. The projection is easily done referring the nodal coordinates to the image plane system.

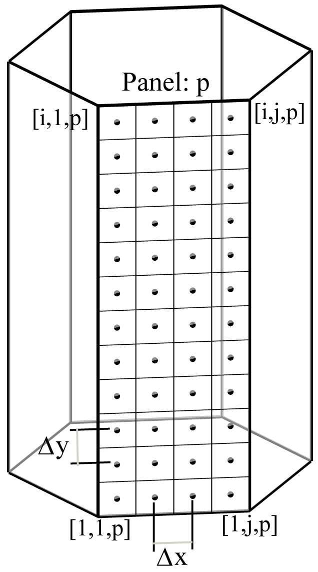

Figure 2.5: Schematic discretization of a receiver panel.

The image system of coordinates (si), with origin in the target point T, matches the $X_{si}Y_{si}$ plane with the image plane. The X_{si} axis is kept horizontal, as X_{st} axis. In the direction of the Z_{si} axis, the $\mathbf{w}_{si}$ unit vector is equivalent to the opposite of vector $\mathbf{t}$.

The transformation from target to image system of coordinates involves two rotations. The azimuth angle of rotation, α_t, is that of $-\mathbf{t}$ referred to the normal of the target panel. And the elevation angle of rotation, ε_t, is that of $\mathbf{t}$ relative to its horizontal projection. The positive rotation angles are displayed in Figure 2.6, along with the target and the image systems of coordinates. In matrix notation, the transformation from target to image coordinate system is developed through the following Equation:

$$\begin{bmatrix} x \\ y \\ z \end{bmatrix}_{si} = \begin{bmatrix} \cos\alpha_t & 0 & \sin\alpha_t \\ -\sin\alpha_t \cdot \sin\varepsilon_t & \cos\varepsilon_t & \cos\alpha_t \cdot \sin\varepsilon_t \\ -\sin\alpha_t \cdot \cos\varepsilon_t & -\sin\varepsilon_t & \cos\alpha_t \cdot \cos\varepsilon_t \end{bmatrix} \cdot \begin{bmatrix} x \\ y \\ z \end{bmatrix}_{st} \tag{2.6}$$

Once in image coordinate system, the projection of the receiver nodes onto the image plane is straightforward. While x and y coordinates remain fixed, the z coordinate drops to zero, thus reaching the image plane. Symbolizing the projection onto the image plane with the superscript *image*, the projection is algebraically equivalent to:

$$\begin{cases} x_{si}^{image} = x_{si} \\ y_{si}^{image} = y_{si} \\ z_{si}^{image} = 0 \end{cases} \tag{2.7}$$

At most, half of the receiver is visible from a heliostat position, while the other half is hidden. Hence, only the visible panels are projected onto the image plane.

The opposite direction of the central reflected beam, $-\mathbf{t}$, has been assumed as the direction of projection. Actually, due to the divergence of sun rays there is not a sole reflected beam direction, even though the central

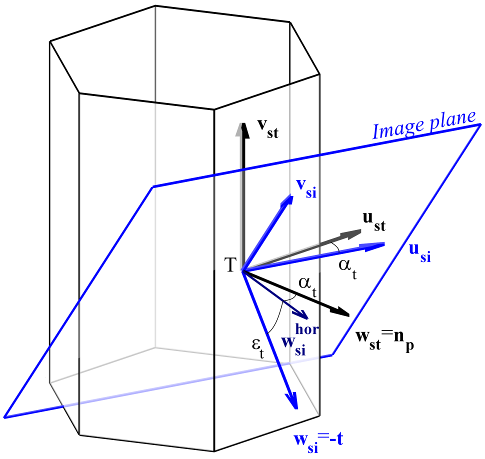

Figure 2.6: Transformation from target plane to image coordinate system.

ray represents the mean and most probable beam direction. The deviation increases with the distance from image plane to the receiving surface. Known the sunshape error (σ_{sun}), for a typical receiver with 4 m of radius, the maximum error is about one centimeter.

2.2.4 UNIZAR analytic function on the image plane

Collado *et al.* (1986) defined two analytic functions for the solar flux density, both on the image plane and on the plane of flat plate receivers. Since linear mapping was assumed, the precision at receiver plane decreases when the angle of incidence with the panel, ω_p, increases. In other words, the image shape deformation found at the receiver is disregarded. Hence, the analytic function on the image plane was adopted in the present study.

Hypothesis taken on UNIZAR model for the image plane represent adequately actual heliostats. The surface of rectangular heliostats is assumed to be continuous and spherical, being the focal length equal to the slant range (SLR). On-axis alignment is considered so that the astigmatic effect, experienced when the angle of incidence with the heliostat increases, is neglected.

UNIZAR expression for the solar flux density is based on the standard error function (erf). Following a matrix notation where i and j are nodal indices, the concentration ratio of flux density on the image plane becomes:

$$C_{i,j,p}^{image} = \frac{\cos\omega_h}{4\cdot(1-\cos\omega_h)^2}\cdot\left[erf\left(\xi_{i,j,p}+aw\right)-erf\left(\xi_{i,j,p}-aw\right)\right]\cdot\left[erf\left(\zeta_{i,j,p}+ah\right)-erf\left(\zeta_{i,j,p}-ah\right)\right] \tag{2.8}$$

where the cosine of the incidence angle is the dot product of unitary vectors:

$$\cos\omega_h = \mathbf{n}_h\cdot\mathbf{s} = \mathbf{n}_h\cdot\mathbf{t} \tag{2.9}$$

The variables $\xi_{i,j,p}$ and $\zeta_{i,j,p}$ correspond to the linear transformation of x_{si} and y_{si} coordinates on the image plane, whereas aw and ah stand for the integration limits. These variables include in their definition the effective error (σ_e), which is the convolution of sunshape, mirror slope and heliostat tracking errors. Modeled these errors as circular Gaussian distributions whose standard deviations are σ_{sun}, σ_{slp} and σ_{trk}, respectively, their convolution σ_e is also a circular normal distribution with standard deviation:

$$\sigma_e = \sqrt{\sigma_{sun}^2 + 2\left(1+\cos\omega_h\right)\sigma_{slp}^2 + \sigma_{trk}^2} \tag{2.10}$$

Hereafter sunshape standard deviation is 2.51 mrad, which was measured at PSA. Further details about UNIZAR functions can be found in references (Collado *et al.*, 1986; Collado, 2010).

2.2.5 Flux density on the receiver and intercept factor

The flux density in a node on the receiver is the same as that of its analogous node on the image plane, although affected by the angle of incidence with the receiver panel, ω_p. Therefore, the concentration ratio in node $[i,j]$ belonging to panel p satisfies:

$$C_{i,j,p} = C_{i,j,p}^{image} \cdot \cos\omega_p \tag{2.11}$$

Note that the concentration ratio obtained from Equation (2.11) does not take into account the heliostat optical losses; except for the cosine of the angle of incidence on the heliostat, $\cos\omega_h$, which is implicitly included in Equation (2.8). The calculation of spillage losses is explained in the following paragraphs, while the remaining loss factors are introduced in Chapter 4, Section 4.3, for the whole field of heliostats.

A portion of the flux reaching the image plane cannot be intercepted by the receiver, incurring spillage losses. The intercept factor, f_{int}, is the fraction of solar flux reflected by the heliostat actually intercepted by the receiver.

$$f_{\text{int}} = \frac{\bar{F} \cdot AR}{F_{ref} \cdot AM} \tag{2.12}$$

where $\bar{F}$ is the mean flux density on the receiver, AR is the area of the receiver, AM is the mirror area of the heliostat, and $F_{ref} = DNI \cdot cos\omega_h$. The intercept factor is an outcome of the calculation of C. In terms of concentration of flux density in each node of the receiver, the above Equation can be computed as:

$$f_{\text{int}} = \frac{\sum\limits_{i,j,p} C_{i,j,p} \cdot \Delta x \cdot \Delta y}{\cos\omega_h \cdot AM} \tag{2.13}$$

where Δx and Δy are the horizontal and vertical spacing between nodes in the receiver. We can conclude that the intercept factor is a measure of not only the spillage, but also the loss due to the incidence angle on the receiver, implicit in the definition of C.

2.3 Validation for flat plate receivers

The proposed model was first validated for a flat plate receiver, which is the simplest case of external receiver. Our model was confronted against experimental measurements from Plataforma Solar de Almería (PSA) and simulation results from SolTrace, software developed by the National Renewable Energy Laboratory (Wendelin *et al.*, 2013).

The Monte Carlo Ray Tracing (MCRT) technique solves the solar energy collection and transmission according to the following procedure (Wang *et al.*, 2010): the Sun, considered as a massive source of sunlight, emits sunlight rays containing the same energy to ensure uniform distribution of sunlight; the sunlight transmission consists of four independent sub-processes (emission, reflection, transmission and absorption) following a specific probability distribution. In the present work, a bundle of 5 million random rays has been traced for each simulation.

During July 2004, experimental measurements were carried out around noon time in the CRS facility at PSA (Monterreal, 2013). The images produced by individual heliostats on the flat plate receiver, at 35.16 m height, were captured. The Martin-Marietta at PSA is a 39.9 m^2 heliostat; 6.68 m width and 6.63 m height, but without mirror facets in a 0.66 m centered vertical strip. Three heliostat positions at PSA field were selected for comparison, providing a wide variety of slant ranges and incidence angles on both the receiver panel ω_p and the heliostat ω_h. For each heliostat position, its name and geometrical parameters are listed in Table 2.1. The slope errors are taken from previous fitting, where the tracking error was neglected (Collado, 2010).

Table 2.1: Parameters of selected PSA heliostats.

Position name	SLR, m	$cos\omega_p$	$cos\omega_h$	σ_{slp}, mrad
C2	165.3	0.936	0.822	0.80
H61	100.0	0.716	0.895	1.40
H11	59.9	0.714	0.950	2.10

In the following three Figures, the normalized flux distribution on the receiver obtained with the proposed model is compared to that of the measured image (a) and to the SolTrace simulation output (b). Since the measured images provide levels of intensity, rather than flux density, the results in this section are expressed in normalized flux density, i.e. F/F_{max}. In each Figure, the root mean square error (RMSE) between both contours is pointed out.

The heliostat in position C2, Figure 2.7, provides quasi-circular contours, where two symmetry axes can be envisaged. This shape is closely related to the standard error function used in the image plane. Since the solar reflected beam impacts nearly perpendicular to the receiver surface for this heliostat, such spot shape seems plausible.

While increasing the incidence angle on the receiver, ω_p, the distribution shape is stretched in the axis of the incident central ray, leading to quasi-elliptical contours, clearly evident in Figures 2.8 and 2.9. For the positions in Table 2.1, the greater distortion is thus expected in heliostat H11.

Comparison between SolTrace and the suggested model shows excellent agreement. On-axis alignment has been considered in both codes, but the angle of incidence with the heliostat and the defocus distance are sources of astigmatism (Igel & Hughes, 1979; Hénault, 2015). Such aberration is not tackled in the model, whereas SolTrace simulates the real optical behavior. This methodological discrepancy can partially explain the 1.4% RMSE found in heliostat C2.

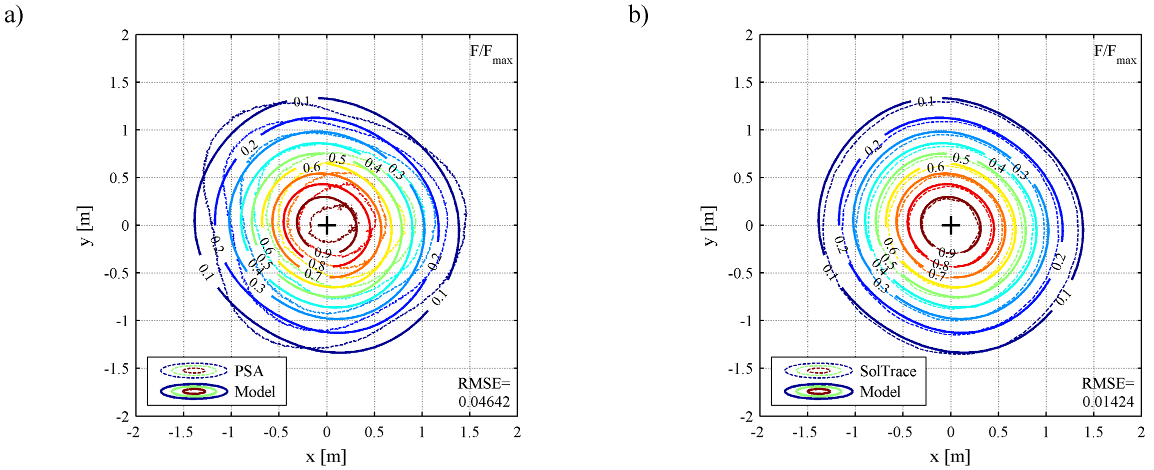

Figure 2.7: Contours of normalized flux due to heliostat C2. Comparison of the model with: a) PSA measurement and b) SolTrace simulation.

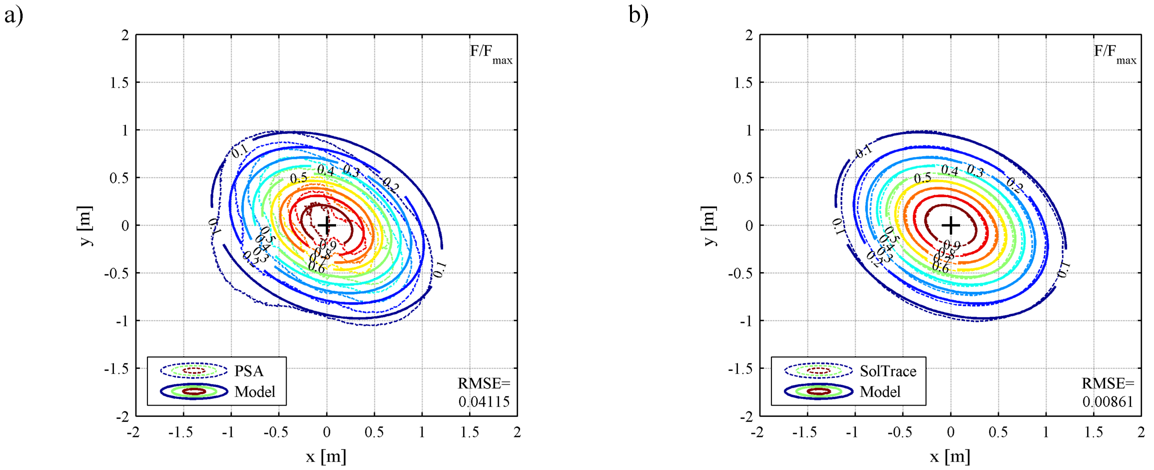

Figure 2.8: Contours of normalized flux due to heliostat H61. Comparison of the model with: a) PSA measurement and b) SolTrace simulation.

Compared to the experimental images, (a) Figures, the general patterns are followed, while particular deviations can be encountered. The RMSE between both curves is around 4% in heliostats C2 and H61, and increases up to 6% in heliostat H11. For the latter (Figure 2.9), differences are more evident. On the other hand, near the aim point where the flux densities are higher, experimental isolines are closer to the center than predicted by the model, as well as SolTrace.

Some disparities are associated with heliostat off-axis alignment, since heliostats were focused and canted for an aim point different to that during the experiments. Apart from heliostat alignment and experimental uncertainty in the measurements, other physical phenomena may explain the measured spots. As an elastic structure, the heliostat frame deflects under wind and gravitational loads, affecting the beam optical quality (Strachan & Houser, 1993). Even temperature differences induce changes of curvature in the mirror facets, causing defocus (Jones *et al.*, 1994).

Despite of acceptable experimental fluctuations, the proposed model can accurately predict the flux distribution on a flat plate receiver, independently of the incidence angle. For increasing incidence angles on

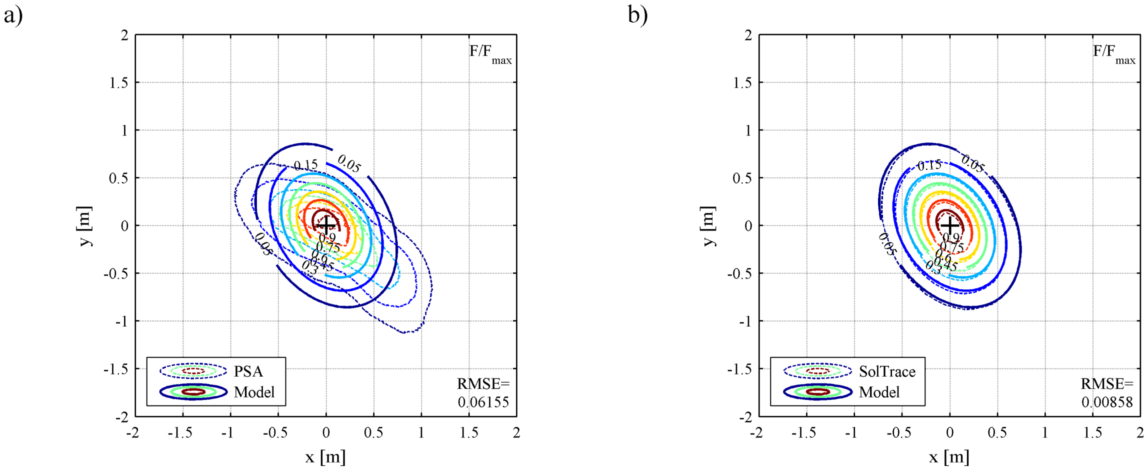

Figure 2.9: Contours of normalized flux due to heliostat H11. Comparison of the model with: a) PSA measurement and b) SolTrace simulation.

the receiver, spot shapes are conveniently distorted likewise MCRT predictions.

2.4 Validation for multi-panel cylindrical receiver

The proposed model was validated for the most general case: cylindrical receivers formed by any number of panels. The results herein presented correspond to a 16-panels cylindrical receiver. For selected heliostats in a surround field, the flux density distribution calculated with the suggested model is compared to SolTrace simulations. A comparison of the computational cost is presented at the end of the present Section.

2.4.1 Comparison with SolTrace

A staggered heliostat field has been generated using the rules and parameters described in Collado (2010), assuming flat land. The field is composed of 3 zones with 35 heliostat in each row in the first zone. The densest heliostat field, not optimized, is considered.

The rectangular heliostats are 12.305 m width and 9.752 m height, representing 120 m^2 similarly to Gemasolar heliostats. For this kind of heliostat the errors of tracking, σ_{trk}, and slope, σ_{slp}, are 2.1 and 2.6 mrad, respectively (Augsburger & Favrat, 2013). The resulting field layout is shown in Figure 2.10, where the resulting 4550 heliostats are distributed in 43 rows. First row radius is 87.46 m, and last one is 676.17 m.

The central receiver comprises 16 flat panels arranged around a cylindrical shell. For a cylinder of 8.5 m diameter, each panel width is 1.691 m. The receiver, and each panel, is 10.5 m in height. The tower optical height (THT), vertical distance from the heliostat mirror center to the receiver equator, is set to 120 m.

Noon time of spring equinox, i.e. Julian day number 81, is considered in the results herein presented. For instance, the field is located at 37.1° latitude north, as PSA facility. Therefore, the solar altitude at solar noon is 52.9°.

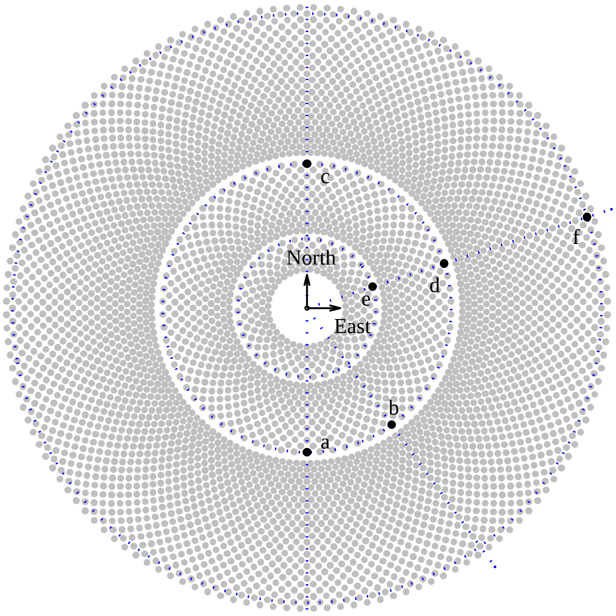

Figure 2.10: Field layout and selected heliostats.

Six heliostat positions were selected, black dots in Figure 2.10. For a middle row, the azimuth position is varied in four heliostats (*a*, *b*, *c* and *d*); where heliostat *a* corresponds to sun position and heliostat *c* to anti-sun. Maintaining the azimuth of heliostat *d*, heliostats *e* and *f* are near and farther to the receiver, respectively. For the above mentioned instant of time, the cosine of the solar incidence angle on each heliostat is indicated in Table 2.2, together with location parameters.

Table 2.2: Location and incidence angle of selected heliostats.

Heliostat	Azimuth, deg	Row radius, m	SLR, m	$cos\omega_h$
a	0	324.5	341.9	0.60
b	−36	324.5	343.0	0.64
c	±180	324.5	341.9	0.96
d	−108	324.5	342.0	0.85
e	−108	155.4	193.0	0.91
f	−108	662.6	669.2	0.81

The flux distribution from each selected heliostat is below showed. Results are expressed in terms of the concentration ratio of flux density, as defined in Equation (2.3). Therefore, data are independent of instantaneous solar radiation. Since Equation (2.11) is used, loss factors because of reflectivity, attenuation and shading and blocking were neglected. These loss factors will be included in Chapter 4.

For each individual heliostat, Figure 2.11 shows the contours of flux density concentration on the unfolded surface of the receiver. Only the corresponding half visible side of the receiver is represented; each panel number is displayed at the top. Solid lines correspond to the present model, while dashed lines correspond to SolTrace simulation.

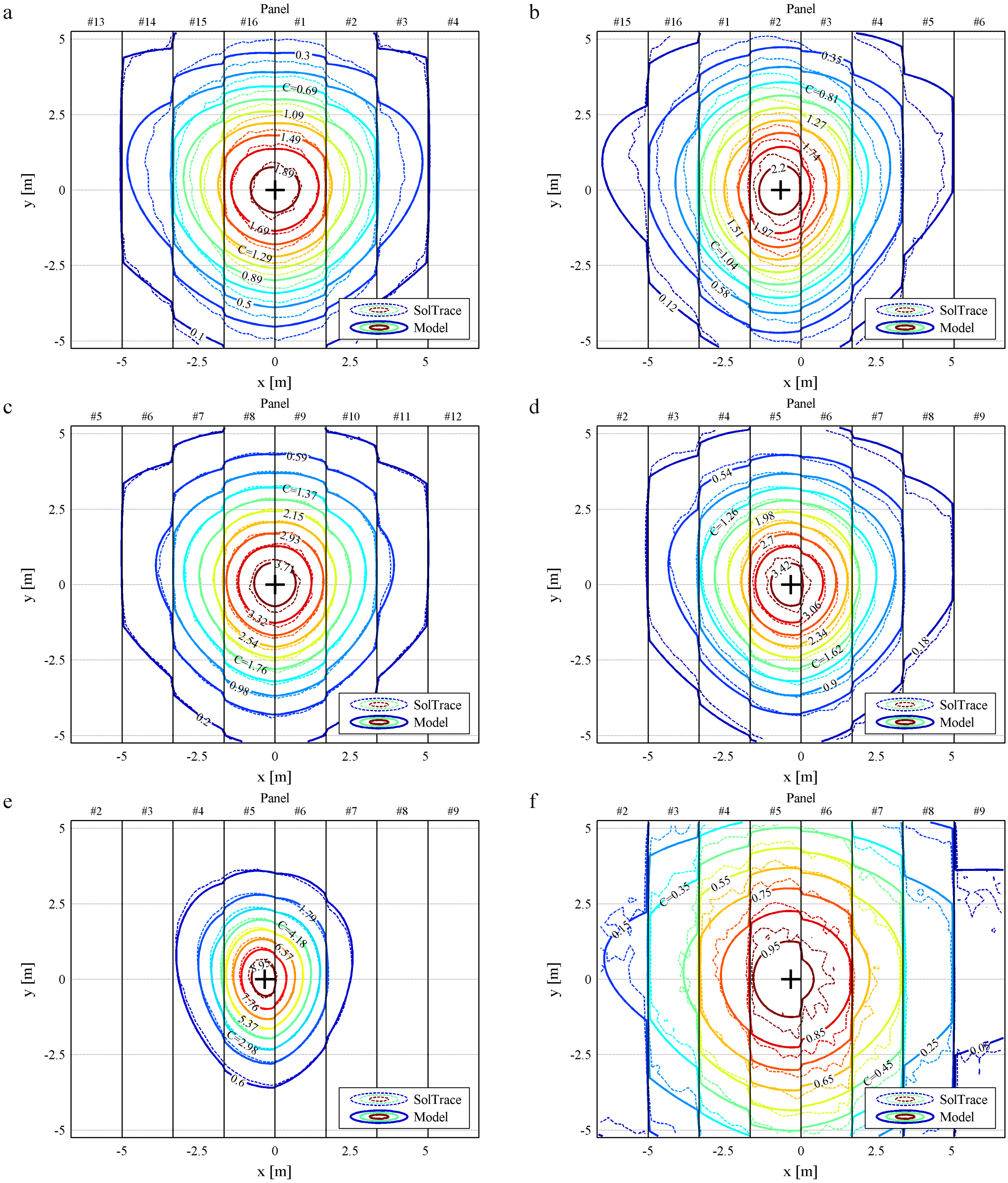

Figure 2.11: Contours of concentration ratio of flux density for heliostats *a*, *b*, *c*, *d*, *e* and *f*.

For the anti-sun position, heliostat *c*, contours lines by the model fit well the SolTrace simulation. Isolines seem to slightly separate when the heliostat cosine decreases. Even for the worst case, heliostat *a*, differences are not significant. Astigmatic aberrations, solved by SolTrace, are again the source of error.

Despite the differences commented in the paragraph above, the proposed model follows the shapes simulated with SolTrace. For the same row, the heliostats in the position of sun (a) and anti-sun (c) produce similar image shapes, while the former is wider. Heliostats in intermediate positions (b and d) lead to image sizes between those, and rotated at the same time.

For a given azimuth angle, the heliostat image is smaller the closer the heliostat is to the receiver (e). Differences between the model and MCRT simulation emerge when the slant range increases. As beam diameter at the focus broadens, 5 million rays do not provide enough resolution, which explains the ripples found in SolTrace isolines for heliostat f. In the side panels where the incidence angle is larger, image shapes are distorted as anticipated for flat plate receivers.

The intercept factor calculated with Equation (2.13) are compared to SolTrace output (Table 2.3). For the selected heliostats, this factor is underestimated by the model, even though deviations do not reach 2%. Insignificant underestimation is also found in the average and peak concentration ratios, listed in Table 2.3.

Table 2.3: Intercept factor, mean and peak concentration ratio for the model and SolTrace.

Heliostat	f_{int}		C_{mean}		C_{max}	
	Model	SolTrace	Model	SolTrace	Model	SolTrace
a	0.917	0.933	0.463	0.472	1.985	2.028
b	0.928	0.939	0.503	0.509	2.318	2.440
c	0.945	0.953	0.767	0.773	3.910	4.040
d	0.948	0.955	0.683	0.688	3.597	3.685
e	1	1	0.765	0.766	9.551	9.844
f	0.596	0.608	0.410	0.419	0.998	1.046

2.4.2 Computational cost and spatial resolution

The distance between nodes in the receiver was set to 10 cm. This nodal spacing was selected from a compromise between CPU time and resolution. The gradient of concentration ratio between nodes is an indicator of such spatial resolution. For the near heliostat e, Figure 2.12 illustrates the CPU time averaged over 10 realizations. For distances lower than 10 cm the computation time rapidly increases. On the other hand, the maximum gradient increases with the nodal spacing.

Simulations were carried out in an Intel® Core™ i5-2400 microprocessor at 3.10 GHz with 4GB of RAM memory. Given 10 cm between nodes, our code takes 0.81 s on average. On the other hand, SolTrace simulations with 5 million rays, in the limit of that hardware, lasts an average time of 43.5 s, using a single core in both cases. The average CPU time employed by SolTrace using 0.5, 1, 2 and 5 millions of intercepted rays is represented in Figure 2.13 for heliostat d at 342 m distance to the target point. Because it is a stochastic method, its accuracy and spatial resolution is dependent of the amount of rays traced. Hence, the standard deviation of the power incident on the receiver, P_{inc}, based on 30 realizations is taken as a measure of the exactitude. Such dispersion decreases when the more rays are traced.

To sum up, the proposed model replicates the distributions simulated with SolTrace, using 50 times less computation time. Furthermore, the spatial resolution can be greater than that of the MCRT simulation.

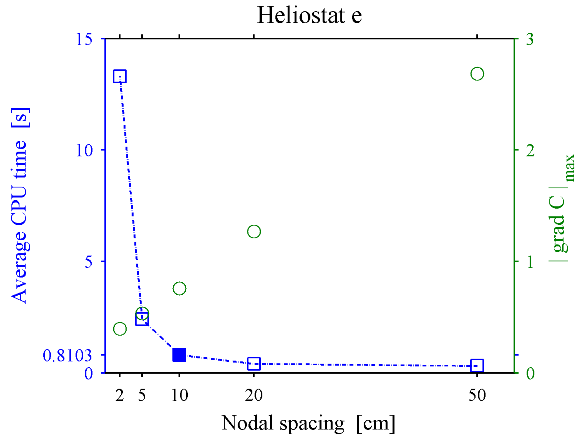

Figure 2.12: CPU time and maximum gradient for different distances between nodes.

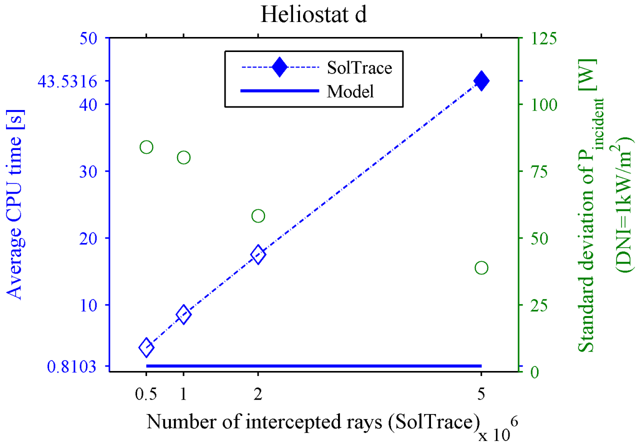

Figure 2.13: CPU time and standard deviation of power incident on the receiver for different numbers of rays.

2.5 Conclusions

A 4-step methodology to determine the flux density distribution on central receivers of flat panels was established. This procedure relies on the oblique projection onto the receiver from the flux distribution on the image plane. This is accomplished by a simple coordinate system transformation, implemented in a computer code.

In this Chapter, the projection method was applied on the basis of the analytic function at the image plane by Collado *et al.* (1986). The resulting model solves the distorted spot found when the incidence angle on the receiver increases. For any given rectangular focusing heliostat, the model compares successfully to both PSA measurements and SolTrace simulations. Compared to the latter, our code underestimates up to 2% the receiver interception. Considerable computation time is saved over MCRT, all of this with similar degree of accuracy and even higher resolution level for far heliostats.

Nomenclature

ah, aw	Limits of the convolution integral [m]
AM	Area of heliostat mirror [m^2]
AR	Area of receiver [m^2]
C	Concentration ratio of flux density [-]
DNI	Direct normal irradiance [$\mathrm{W/m}^2$]
F	Solar flux density [$\mathrm{W/m}^2$]
f	Optical loss factor [-]
G	Origin of the global coordinate system
H	Center of heliostat mirror
$\mathbf{n}$	Normal unit vector
P	Power [W]
$RMSE$	Root mean square error
$\mathbf{s}$	Unit vector pointing to the sun
SLR	Slant range [m]
T	Target point
$\mathbf{t}$	Unit vector from H to T
THT	Tower optical height [m]
$\mathbf{u}$, $\mathbf{v}$, $\mathbf{w}$	Unit vectors in X, Y, Z-direction
X, Y, Z	Cartesian coordinate axes
x, y, z	Coordinates in X, Y, Z-direction

Greek symbols

α	Azimuth angle [rad]
Δx, Δy	Nodal spacing in X, Y-direction [m]
ε	Elevation angle [rad]
ξ, ζ	Linear transformation of x, y [m]
σ	Error, standard deviation [mrad]
ω	Incidence angle [rad]

Subscripts

e	Effective
h	Heliostat
i, j	Node index
inc	Incident
int	Interception
max	Maximum
p	Panel number in the receiver
pt	Target panel
ref	Reflected
sg	Global system of coordinates
sh	Heliostat system of coordinates
si	Image plane system of coordinates
slp	Mirror slope
st	Target system of coordinates
sun	Sunshape
trk	Tracking

Superscripts

image	projection onto image plane

Acronyms

CPU	Computer's central process unit
CRS	Central Receiver System
MCRT	Monte Carlo Ray Tracing
PSA	Plataforma Solar de Almería

References

AUGSBURGER, G. & FAVRAT, D. 2013 Modelling of the receiver transient flux distribution due to cloud passages on a solar tower thermal power plant. *Solar Energy* 87, 42–52.

BIGGS, F. & VITTITOE, C. N. 1979 Helios model for the optical behavior of reflecting solar concentrators. *Tech. Rep.*. Sandia National Laboratories, SAND-76-0347.

BRAUN, J. E. & MITCHELL, J. C. 1983 Solar geometry for fixed and tracking surfaces. *Solar Energy* 31 (5), 439–444.

COLLADO, F. J. 2010 One-point fitting of the flux density produced by a heliostat. *Solar Energy* 84 (4), 673–684.

COLLADO, F. J., GÓMEZ, A. & TURÉGANO, J. 1986 An analytic function for the flux density due to sunlight reflected from a heliostat. *Solar Energy* 37 (3), 215–234.

COOPER, P. I. 1969 The absorption of radiation in solar stills. *Solar energy* 12 (3), 333–346.

GARCIA, P., FERRIÈRE, A. & BEZIAN, J.-J. 2008 Codes for solar flux calculation dedicated to central receiver system applications: A comparative review. *Solar Energy* 82 (3), 189–197.

HÉNAULT, F. 2015 Fast computation of solar concentrating ratio in presence of opto-mechanical errors. *Solar Energy* 112, 183–193.

IGEL, E. & HUGHES, R. 1979 Optical analysis of solar facility heliostats. *Solar Energy* 22, 283–295.

JONES, S. A., EDGAR, R. M. & HOUSER, R. M. 1994 Recent results on the optical performance of solar two heliostats. *Tech. Rep.*. Sandia National Laboratories.

KISTLER, B. 1986 A user's manual for DELSOL3: Computer code for calculating the optical performance and optimal system design for solar thermal central receiver plants. *Tech. Rep.*. Sandia National Laboratories, SAND-86-8018.

LIPPS, F. W. & WALZEL, M. D. 1978 An analytic evaluation of the flux density due to sunlight reflected from a flat mirror having a polygonal boundary. *Solar Energy* 21 (2), 113–121.

MONTERREAL, R. 2013 Personal communication.

SCHWARZBÖZL, P., SCHMITZ, M. & PITZ-PAAL, R. 2009 Visual HFLCAL - A software tool for layout and optimisation of heliostat fields. In *SolarPACES*. Berlin, Germany.

STRACHAN, J. W. & HOUSER, R. M. 1993 Testing and evaluation of large-area heliostats for solar thermal applications. *Tech. Rep.*. Sandia National Laboratories, SAND92-1381.

WALZEL, M. D., LIPPS, F. W. & VANT-HULL, L. L. 1977 A solar flux density calculation for a solar tower concentrator using a two-dimensional Hermite function expansion. *Solar Energy* 19 (3), 239–253.

WANG, Y., DONG, X., WEI, J. & JIN, H. 2010 Numerical simulation of the heat flux distribution in a solar cavity receiver. *Frontiers of Energy and Power Engineering in China* 4 (4), 571–576.

WENDELIN, T., DOBOS, A. & LEWANDOWSKI, A. 2013 SolTrace: A Ray-Tracing Code for Complex Solar Optical Systems. *Tech. Rep.*. NREL, National Renewable Energy Laboratory, Golden, Colorado.

CHAPTER

THREE

Determination of heliostat canting errors via deterministic optimization

Contents

Summary

This Chapter presents a methodology to find out canting errors in mirror modules or facets of real heliostats. An optimization procedure was established to fit simulated flux distributions from heliostats to those measured on the white target of THEMIS solar plant in this instance. On the basis of the optical model developed in Chapter 2, a deterministic algorithm, named DIRECT, was successfully implemented reaching correlation coefficients up to 98%. From the optimization results, the heliostat with higher canting errors was readjusted. As a result, its optical quality was highly increased; and, the methodology was validated (Sánchez-González *et al.*, 2017).

3.1 Introduction

Beam quality of heliostats depends on the correct alignment. Heliostat alignment involves two operations: mirror focusing and heliostat canting. Mirror focusing consists in slightly bending the mirror surface into a concave shape, so that the size of the reflected sun image is minimized (Chong, 2014). Heliostat canting consists in tilting the mirror modules to aim at the same point. Proper heliostat alignment results in maximizing the annual power intercepted by the receiver (Jones, 1996*b*).

Heliostat canting techniques, on which this Chapter is focused, are classified into three categories (Ren *et al.*, 2014): on-sun, mechanical, and optical alignment. In the first method, mirror modules are individually (and qualitatively) canted while the sun is impinging on the heliostat and the rest of the modules are covered. Mechanical alignment makes use of gauge blocks or inclinometers to adjust the orientation of the modules while the heliostat is in horizontal position; this method is very time consuming, as well as on-sun alignment.

Six optical alignment techniques can be identified: laser method, camera look-back, photogrammetry, deflectometry, TOPHAT and H-FACET. There are two laser beam projection methods (Yellowhair & Ho, 2010): scanning prism laser projection and parallel laser beam projection. Camera look-back method was developed and successfully tested by SNL (Jones *et al.*, 1994). Photogrammetry and deflectometry techniques utilize camera images to determine the orientation of heliostat facets. Theoretical overlay photographic heliostat alignment technique, TOPHAT (SNL, 2013), and heliostat focusing and canting enhancement technique, H-FACET (Sproul *et al.*, 2011), are tools feed by camera images, both of which were recently developed by SNL.

In this Chapter it is proposed a novel methodology to find out canting errors in focused heliostats to correct them. From heliostat experimental images taken in THEMIS solar power tower plant, an optimization procedure was developed to minimize the difference between experimental flux distribution and simulations, where module canting errors are the unknowns. The experimental set up and characteristics are described in the next Section. Afterwards, the proposed procedure is presented, as well as results for three heliostats. From the results, one heliostat is *in situ* readjusted to validate the proposed methodology.

3.2 Problem description

Misalignment of mirror facets leads to heliostats with poor optical quality. On a lambertian target near the receiver, flux distributions from misaligned heliostats result in images with multiple spots and/or large beam sizes. Some heliostats at THEMIS plant were found to be incorrectly adjusted. In this Section, it is described the characteristics of the heliostats and the experimental campaign carried out at THEMIS.

3.2.1 Canting errors in CETHEL heliostats

CETHEL heliostat in THEMIS field consists of 9 rectangular modules of mirrors. Eight modules are distributed in two wings at either side of the heliostat pole, and a ninth smaller module is in between and above the pole. Figure 3.1 shows a photograph of one of the heliostats in the field and a drawing with the dimensions of the heliostat and the modules; total reflective surface is 54 m^2.

The module consists of three vertical strips of parabolic mirror; two strips in the complimentary module. Each mirror strip is mechanically tighten to the module frame so that curvature and orientation are forced. As a result, each module acts almost like a single spherical mirror with focal distance, f_m. This way, heliostat focusing is achieved. In this study, CETHEL heliostats are assumed to be properly focused.

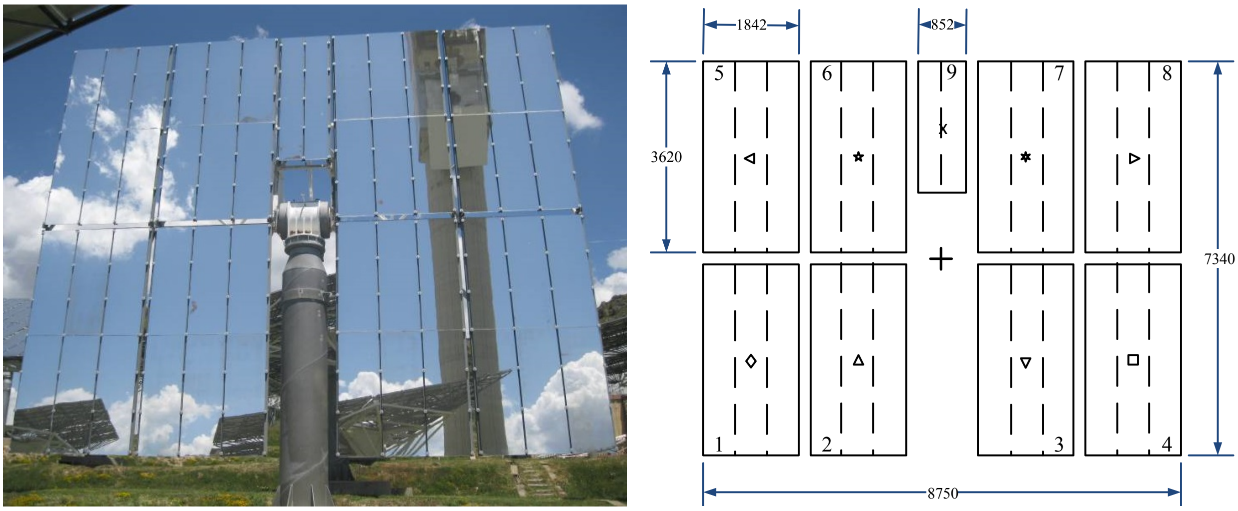

(a) Photograph of heliostat B10.

(b) Geometry. Dimensions in mm.

Figure 3.1: CETHEL heliostat.

Surface slope error (σ_{slp}), defined as the root mean square error of the mirror shape to the ideal, is not known. For CETHEL heliostats mirror slope error is expected to be around 1 mrad.

On the other hand, each module is supported on the rear heliostat structure in three points. Through adjustment of these three screw-nut assemblies, each module can be slightly tilted along its two axis; only one in the case of the complimentary module. This process is known as heliostat canting.

A heliostat is properly canted when the normal vectors of all the modules intersect in the same point. This point is the center of a sphere with radius $2 \cdot f_h$, being f_h the focal length of the heliostat. Figure 3.2 represents the geometry of CETHEL heliostat with modules canted towards the same point. This is called on-axis alignment, because it is optimized for the case of heliostat center, target and sun falling in the same line; otherwise, the term off-axis alignment is utilized (Jones, 1996*a*).

CETHEL heliostats were initially canted during THEMIS plant commissioning in early 80's. A bubble leveled tool was used to cant each module while the heliostat is in horizontal position. More than 30 years later, some of the heliostats have lost optical quality, according to flux images on the target plane; as will be shown in results Section.

The source of current lack of adjustment in some heliostats is not known with certainty, but some hypothesis can be made. An initial guess is the progressive loosen of screw nuts that keeps the module in a fixed position. Another hypothesis is the presence of permanent deformation in the supporting structure due to the impact of hail or even provoked by extreme wind gusts. Finally, heliostat deformation because of gravity sag (Yuan *et al.*, 2014) is presumed to have small influence on the optical quality of CETHEL heliostats, because of its structural stiffness.

Angular canting deviations, δ, are referred to the ideal orientation of the module occurring when it is properly canted. The reference coordinate system of the module with origin in its center is depicted in Figure 3.3; X is parallel to the module short side, Y is parallel to the long side, and Z is perpendicular to the mirror and oriented towards the center of the sphere with radius $2 \cdot f_h$.

On the basis of the coordinate system, two angles are defined to describe the error of canting in each

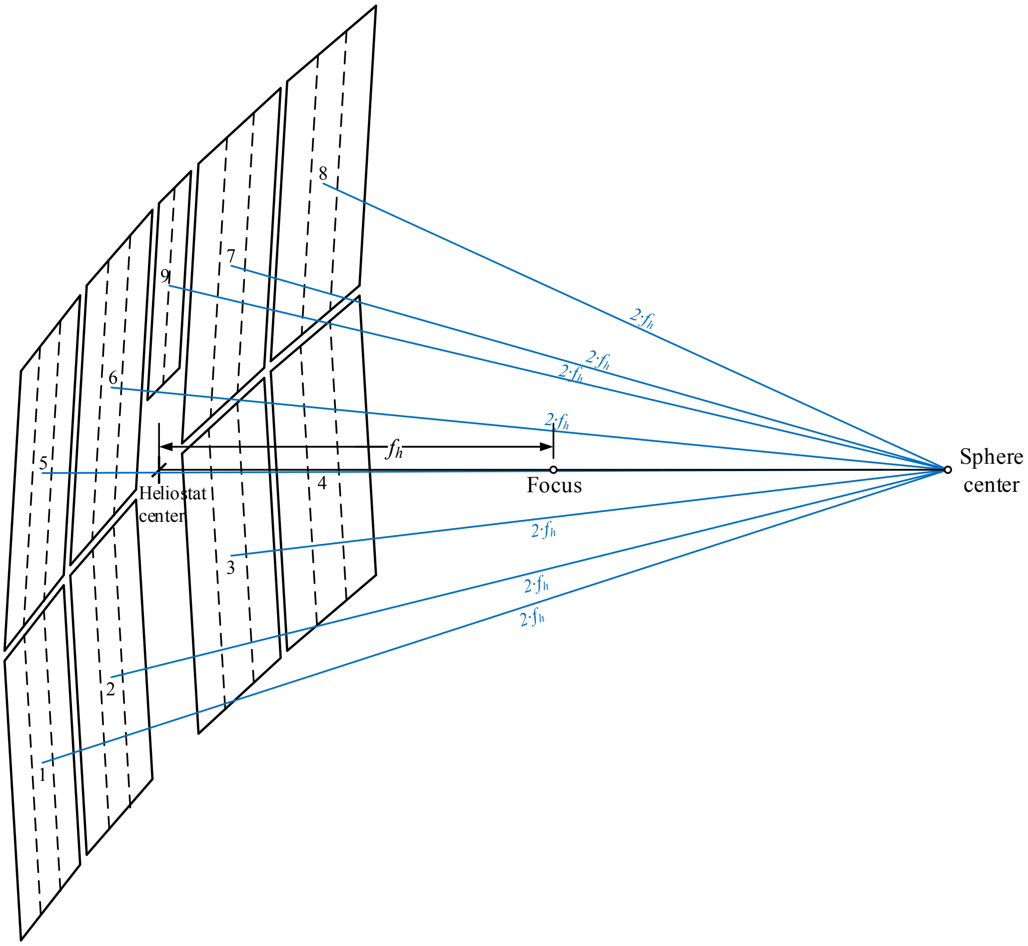

Figure 3.2: On-axis aligned CETHEL heliostat.

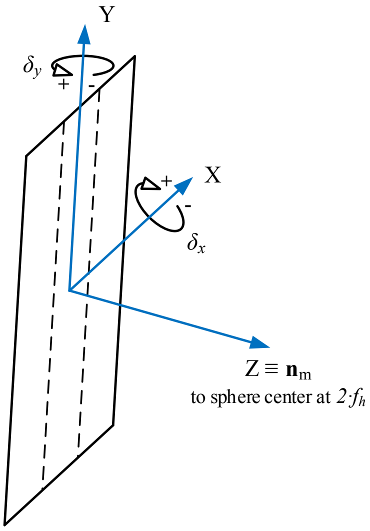

Figure 3.3: Module system of coordinates for angular canting errors.

module: δ_x rotation angle about X axis, and δ_y rotation angle about Y axis. In module 9, canting is only allowed about the horizontal axis, δ_x. Therefore, a total of 17 angular canting errors can be defined.

In this Chapter, it is exposed a methodology to find out those 17 canting errors for CETHEL heliostats. Slope error, assumed uniform for all the heliostat modules, is also unknown. In total, there are 18 unknowns in the problem. The proposed solution method is based on an optimization procedure which makes use of experimental images as the basic input in the model.

3.2.2 Experimental campaign

THEMIS plant is located in Targasonne, France, at 42°30' north latitude. THEMIS solar power tower plant was under commercial operation in the period 1983-1986, and currently is a solar research platform belonging to CNRS, PROMES laboratory.

THEMIS solar field consists of 107 CETHEL heliostats placed on a south oriented hillside. The heliostat field follows a radial staggered north field arrangement. On the top of a 100 m high tower, two open areas allow the testing of flat, cavity and volumetric receivers.

To analyze the optical quality of heliostats, they are aimed to the white target placed under the receiver apertures at 68.3 m from the base of the tower. The square lambertian target, 7.5 m side and tilted from the vertical 30° towards the heliostat field, has the property of diffusively reflecting flux, regardless of the point of view.

On the ground, in the middle of the heliostat field, a camera with CCD sensor is utilized to take pictures of the flux distribution reflected by the white target. The CCD camera with adapted filters has 1392 x 1040 pixels of spatial resolution and each pixel has 14 bits or, equivalently, 16384 levels. Rather than F flux density measurement in W/m^2, camera images provide intensity levels, IL. Dividing the level of intensity in each pixel by the maximum in an image, it is obtained an adimensional parameter equivalent to the normalized flux density, FN, defined as:

$$FN = \frac{F}{F_{\max}} \simeq \frac{IL}{IL_{\max}} \tag{3.1}$$

An experimental campaign was carried out along July 18, 2016. Several images from selected heliostats were captured on the white target. In the present Chapter, results from three heliostats are presented. These heliostats are placed in the fourth row of the field at positions A06, B10 and C04, according to THEMIS field notation. In the aerial photo of THEMIS field in Figure 3.4, the position of the three selected heliostats is marked.

As stated in heliostat design specifications, the heliostat and mirror focal lengths are respectively 100 and 103.6 m; the same for all three selected heliostats. Besides focal lengths, Table 3.1 lists the slant ranges, SLR, of the three heliostats to the center of the white target. Because of the difference between focal lengths and SLR, some defocus (around 12 m) is expected on the white target.

For each heliostat, a total amount of 28 images were recorded during 8 sunshine hours; on average, about one image every 20 minutes. This means more images than the 17 degrees of freedom in the optimization problem, which reduces the uncertainty in the solution and improves its reliability. In results Section, Figures 3.6, 3.8 and 3.10 show in dashed lines the experimental flux distributions at 11 instants of time by heliostats A06, B10 and C04, respectively.

Figure 3.4: Photograph of THEMIS heliostat field from the receiver. Selected heliostats are marked.

Table 3.1: Focal lengths of selected heliostats.

Heliostat	Focal of the heliostat f_h [m]	Focal of the modules f_m [m]	Distance to the target SLR [m]
A06	103.6	100	89.76
B10			87.86
C04			88.37

Image treatment

Subsequently, raw images were processed to be handled by the computational model. Image treatment involved the operations of window selection, reconstruction of bad pixels and resolution adjustment. These operations were automated in a computer code.

The frame of the camera was a bit larger than the 7.5 x 7.5 m of the white target, thus images were initially cropped to match the target extension. Since captured flux spots were smaller than the size of the target, a centered window frame of 5 x 5 m was finally taken. In this way, many pixels with zero intensity level are saved, as well as computation time later on with the model.

From detailed image inspection, it was detected a tiny group of camera pixels giving erroneous values; usually smaller than expected. Once these pixels were identified, their values were removed and interpolation from surrounding pixels was performed.

Finally, resolution of the experimental image was forced to match that computed later in the model. Using the same mesh, the calculation of differences between experimental and simulated maps is faster and more efficient.

3.3 Methodology

The method developed to find out canting errors in heliostats is based on fitting the flux distributions from an accurate optical model to match the experimental images. The optical model incorporates the canting errors, that are the unknowns to be determined using an optimization procedure.

The model presented in previous Chapter 2 is utilized (Sánchez-González & Santana, 2015). Now, instead of a single function evaluation per heliostat, the flux distribution by each module is computed separately and summed at the end. The angular canting errors in each module, δ_x and δ_y, are taken into account in the calculation. For the CETHEL heliostat with 9 modules, a total of 17 degrees of freedom are included in the model.

Besides steady geometric parameters like those presented in previous Section, the model is fed with the sun position vector, $\mathbf{s}$. From the local clock time at which each image was captured, solar position is gathered via the online calculator provided by the U.S. Naval Observatory (USNO, 2016).

For the sunshape, it was adopted a Gaussian distribution with standard deviation, σ_{sun}, 2.09 mrad, as used in other cone optics codes like HELIOS (Biggs & Vittitoe, 1979) and HFLCAL (Schmitz *et al.*, 2006).

In the following, it is first described the process to infer the last input parameter: heliostat target point at each instant of time. Later, the definition of the optimization method is presented: objective function, and selection of the optimization algorithm.

3.3.1 Inference of the target point

Canting angular errors are referred to the ideal orientation of the modules occurring when they are adjusted, as previously described in Subsection 3.2.1. Ultimately, angular errors are referenced to the heliostat normal, that is a vector changing in time because of solar tracking.

Heliostat control algorithm works with encoder counts in both azimuth and elevation axis, however the reference biases of each heliostat are ignored. Hence, an accurate measurement of heliostat orientation (i.e. azimuth and elevation) is absent. To solve the lack of such datum, an inference procedure was developed.

Given a solar position, defined by sun vector $\mathbf{s}$, the heliostat normal vector ($\mathbf{n}$) is found from the target vector ($\mathbf{t}$), and vice versa; Equation (2.3). The heliostat target point is in the intersection between vector $\mathbf{t}$ and the plane of the target. If the position of the heliostat target point could be deduced on the basis of the experimental image and the optical model, vectors $\mathbf{t}$ and $\mathbf{n}$ would be defined.

The procedure to infer the position of the target point, $\mathbf{TP}$, is based on matching the weighted centroids of the experimental image, $\mathbf{WC}_{exp}$, and the simulated flux map, $\mathbf{WC}_{mod}$. Taking $\mathbf{WC}_{exp}$ as the initial target point to compute the flux map, an iterative procedure is established to force $\mathbf{WC}_{mod}$ to coincide with $\mathbf{WC}_{exp}$. In practice, just a single iteration is enough to reach an accurate estimation of the target point. This process is made at each instant of time, since the target point may be shifted from one image to the next.

Thus, the procedure to infer the position of the aim point on the target at each time instant can be defined in a simple 3-step process, as follows:

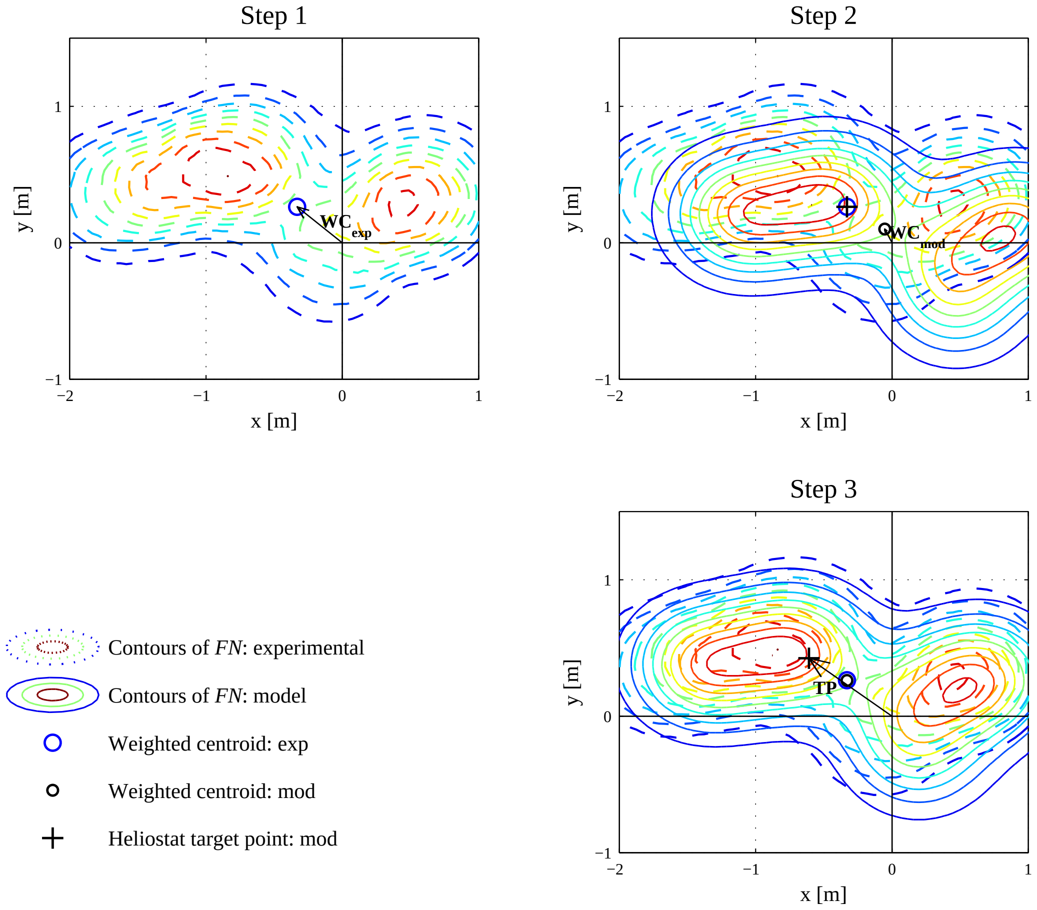

Figure 3.5: Inference of heliostat target point.

1. Calculate the centroid of the experimental image, $\mathbf{WC}_{exp}$.
2. With target point in $\mathbf{WC}_{exp}$, simulate the flux distribution and calculate its centroid, $\mathbf{WC}_{mod}$.
3. Shift the target point to $\mathbf{WC}_{exp} - \mathbf{WC}_{mod}$.

The 3-step procedure to infer the heliostat aim point on the target plane is graphically represented in Figure 3.5; where the experimental image corresponds to heliostat A06 at 11:36. Position vectors of the centroids and the target point are marked in the Figure. Taking advantage of vectorial notation, the position vector of the target point is therefore calculated with the following Equation:

$$\mathbf{TP} = 2 \cdot \mathbf{WC}_{\mathrm{exp}} - \mathbf{WC}_{\mathrm{mod}} \tag{3.2}$$

3.3.2 Objective function

When dealing with optimization problems, two major decisions must be carefully made: the choice of a convenient figure of merit, now discussed; and the selection of a suitable optimization algorithm, discussed in the next Subsection.

The figure of merit is the output parameter in the objective function that the optimization method attempts to minimize, or maximize. Single objective optimization is claimed by the present problem, therefore a single output parameter is minimized, or maximized.

The most straightforward figure of merit is the difference, or residual, between experimental and simulated flux images. More precisely, the residual is the sum of the differences of flux in each pixel or point of computation. However, this cost function has the disadvantage of depending on the size of the spot, which varies along the day. Consequently, the use of the residual was discarded.

To overcome the problem with the residual, two alternative figures of merit were subsequently considered: the root mean square error and the cross-correlation coefficient. Both of them are independent of beam size and image resolution. The cross-correlation coefficient is a parameter frequently used in pattern recognition, e.g. Theodoridis & Koutroumbas (2009), and was finally adopted in this study.

The cross-correlation coefficient (CCC) provides a measure of the fitting between experimental and simulated flux distributions. A CCC value equal to 1 represents a perfect matching between both distributions. The optimization objective is therefore to maximize the CCC or, similarly, minimize its negative.

The cross-correlation coefficient, also known as Pearson correlation coefficient, is calculated with Equation (3.3); where: FN is the 3D matrix of normalized flux densities on the target for all the times (third dimension); N_{elts} is the number of elements in the 3D matrix, which is equal to the number of pixels times the number of images (28 in the present case); SD is the standard deviation of the selected variable; and, subscripts *exp* and *mod* stand for experimental and model.

$$CCC = \frac{1}{N_{elts} - 1} \sum_{n=1}^{N_{elts}} \left(\frac{FN_{\exp,n} - \overline{FN_{\exp}}}{SD\left(FN_{\exp}\right)} \right) \left(\frac{FN_{\mathrm{mod}\ ,n} - \overline{FN_{\mathrm{mod}}}}{SD\left(FN_{\mathrm{mod}}\ \right)} \right) \tag{3.3}$$

3.3.3 Optimization algorithm

The selection of a suitable algorithm is critical to the success of the optimization problem, in order to find a reliable solution. The three major requirements that the optimization algorithm must meet are:

1. Global solution search, avoiding local minima findings;
2. Derivative-free; and
3. Non-linearity.

The two last requirements are dictated by the nature of the objective function.

Among the plethora of global optimization methods (Arora, 2012), the solution failed under metaheuristic algorithms. Particle swarm optimization and genetic algorithm were utilized but the solution resulted very sensitive to parameters tuning. Other stochastic methods, not nature inspired, were tested. Controlled random search (CRS2) with local mutation (Kaelo & Ali, 2006) performed fairly well, even though a high population size, more than 200 samples, is needed to reach a regular solution.

Deterministic global methods have the advantage of always providing the same solution and thus avoiding multiple runs, in contrast to stochastic algorithms. At first, the Nelder-Mead simplex algorithm (Nelder &

Mead, 1965) was used, leading to apparently feasible solutions in short computation time. However, simplex solution was dependent on the selected starting point, so that the first algorithm requirement was not met. Alternatively, simplex algorithm with random multistarts was tested, even though this is not a deterministic method and CRS2 with local mutation is more efficient.

The DIviding RECTangles (DIRECT) algorithm divides the search space into smaller hyper-cubes to find the global minimum (Jones *et al.*, 1993). The dimensions with the lowest objective function values are sequentially divided into thirds. DIRECT does not require parameter tuning and convergence speed is fast. In this study the Matlab® implementation by Finkel (2003) was utilized.

Because of its nature, DIRECT algorithm demands the definition of the bounding box within which the solution falls. Bounds in the search domain can be defined from the analysis of the experimental images. In heliostats where two flux spots emerge, the shift in the target points of the modules is expected to be lower than half of the distance between the two spots. As a result, for instance in heliostat A06, a maximum angular deviation of ±6 mrad was set as the bounds for all the modules in both directions, δ_x and δ_y. Regarding the slope error, 0.5 and 1.5 mrad were established as the lower and upper bounds.

3.4 Canting errors

The optimization procedure described in previous Section 3.3 was applied to the three heliostats introduced in Subsection 3.2.2, i.e. positions A06, B10 and C04. For each heliostat, all the 28 experimental images were considered in the optimization. The corresponding 28 instants of time were simulated with the optical model, now taking part of the objective function that is continuously called by the optimization algorithm.

Using DIRECT algorithm a convergent solution was reached after about 50 iterations, which represents around 10000 evaluations of the objective function. For the selected image resolution, each run of the cost function takes on average 0.67 s in an Intel® Core™ i7-870 microprocessor at 2.93 GHz. Then, less than 2 hours of computation time are enough to reach a convergent solution on the canting deviations in the modules of a CETHEL heliostat.

Table 3.2 summarizes the canting errors found for the three selected heliostats, using the proposed methodology. Canting deviation in each module is expressed with the two axes of orientation, δ_x and δ_y; except for central module 9 where solely adjustment around X is allowed. Sign convention was represented in Figure 3.3. Mirror slope error of the heliostat, initially unknown, is also collected in Table 3.2.

The following figures represent the distributions of normalized flux density, FN, on the white target at 11 of the 28 instants of time considered for each heliostat. In each instant, it can be compared the isolines of FN both measured, i.e. experimental (dashed lines), and simulated, i.e. model (solid lines). The nine FN contour levels, equally spaced between 0.1 and 0.9, are the same in both cases, as designated with the same color.

In Figures 3.6, 3.8 and 3.10, the experimental flux in heliostats A06, B10 and C04 is confronted against the ideal one computed with the optical model, considering that no canting deviations take place in any module; slope error is assumed equal to 1 mrad. From the inspection of these images, a visual assessment on the canting deviations in each heliostat can be made.

Table 3.2: Calculated canting deviations.

		Module								
Heliostat		1	2	3	4	5	6	7	8	9
A06	δ_x [mrad]	-0.64	0.64	0.20	-0.20	0.10	-0.10	0.84	0.64	1.23
	δ_y [mrad]	-2.02	-4.64	1.83	1.04	-3.36	-4.64	0.44	-1.14	-
	σ_{slp} [mrad]	1.00								
B10	δ_x [mrad]	0.40	-1.28	-1.38	-1.28	0.10	0.10	0.00	0.49	-0.20
	δ_y [mrad]	0.99	-0.20	-3.95	-1.38	0.10	0.49	-1.98	-2.77	-
	σ_{slp} [mrad]	1.06								
C04	δ_x [mrad]	0.59	-0.15	-0.74	0.00	0.59	1.48	0.59	0.74	2.07
	δ_y [mrad]	1.33	-1.48	-0.44	-1.19	2.22	0.15	0.74	0.00	-
	σ_{slp} [mrad]	0.93								

The largest discrepancy between measurements and ideal simulation is found in heliostat A06, Figure 3.6. In fact, cross-correlation coefficient is as low as 0.73 from the beginning. In experimental flux distributions, two spots emerge regardless of the time instant; at central hours, even two separate beams can be distinguished.

On the contrary, the flux distribution expected from adjusted heliostat A06 is grouped in a single spot. Only for instants of time near sunrise and sunshine, two peaks come up because of the increasing angle of incidence on the heliostat. Note that the lambertian target is positioned below the receiver position and, consequently, some defocus exists. This, together with the two-wings heliostat geometry, explains the two peaks emerging at some time instants.

Contrary to heliostat A06, where a clear canting problem is coming out, heliostats B10 (Figure 3.8) and C04 (Figure 3.10) present a much smaller deviation to the expected; *CCC* equal to 91.3% and 93.9%, respectively.

Besides flux maps, it is represented in the Figures the weighted centroids of the experimental and the simulated distributions. Following the instructions in Subsection 3.3.1, both points coincide in order to infer the position of the target point, also represented in the Figures with black + marker. Similarly, the target points of every module are subtly marked in the representations; symbols used for every module are those depicted in former Figure 3.1b.

Figures 3.7, 3.9 and 3.11 represent the distributions of normalized flux density both measured (*exp*) and simulated with the canting errors found (*mod*), again for heliostats A06, B10 and C04. The solutions found with the proposed optimization method reproduce fairly well the experimental images.

The cross-correlation coefficient *CCC* increases up to 95.8% (A06), 98.5% (B10) and 97.3% (C04). Ideally, the *CCC* should reach 1 to consider a perfect solution, however some factors prevent it. The optical model, grounded in UNIZAR (Collado *et al.*, 1986), considers an ideal spherical surface for each mirror, i.e. module. As pointed out in Subsection 3.2.1, CETHEL module consists of three strips of parabolic mirror. The flux distribution by a CETHEL module is very similar to that of an spherical mirror with the same dimensions, even though it was proved by MCRT simulation that both distributions are not exactly the

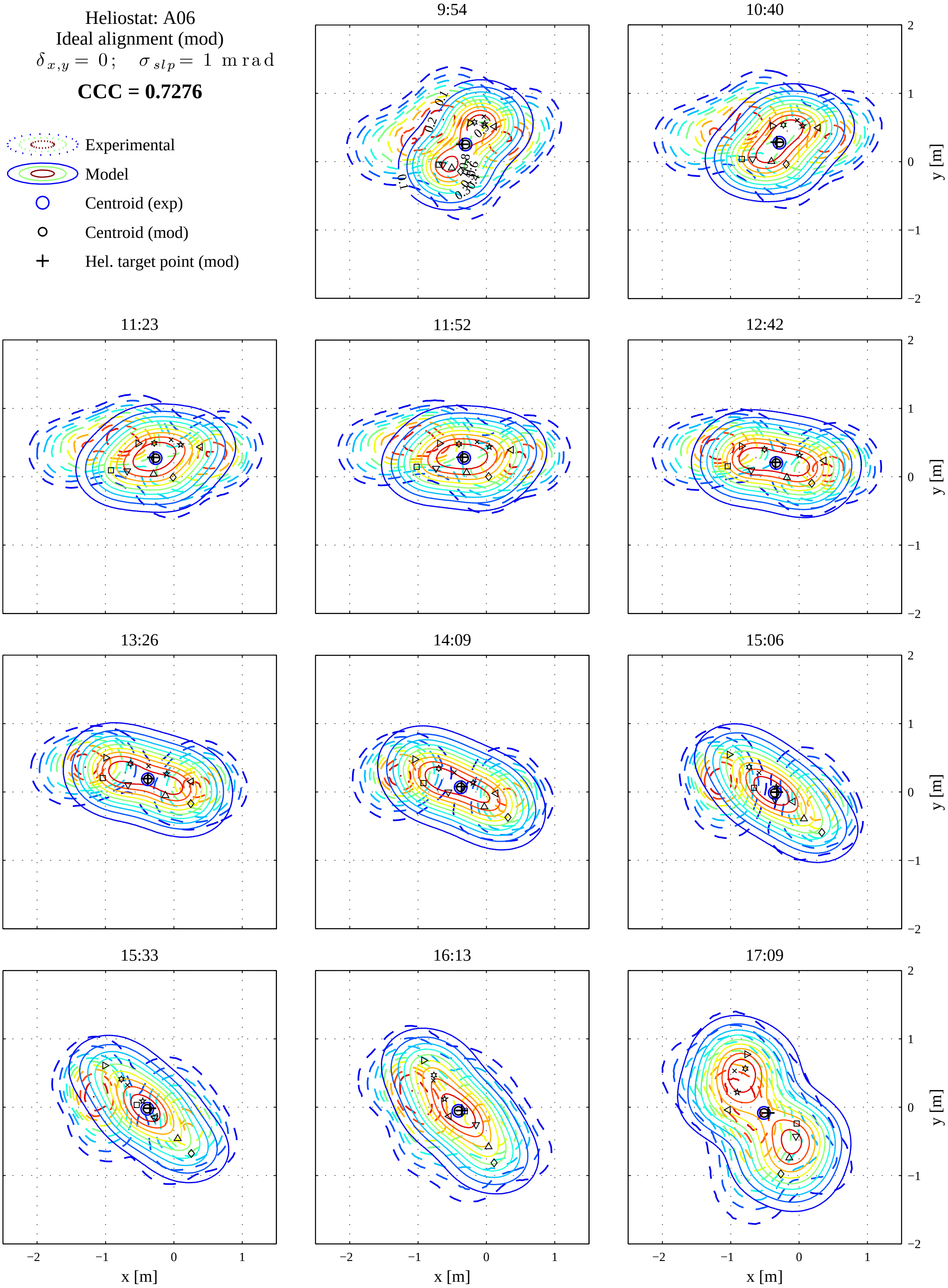

Figure 3.6: Contours of normalized flux density from heliostat A06 at different times in July 18, 2016. Experimental *vs.* model with ideal alignment.

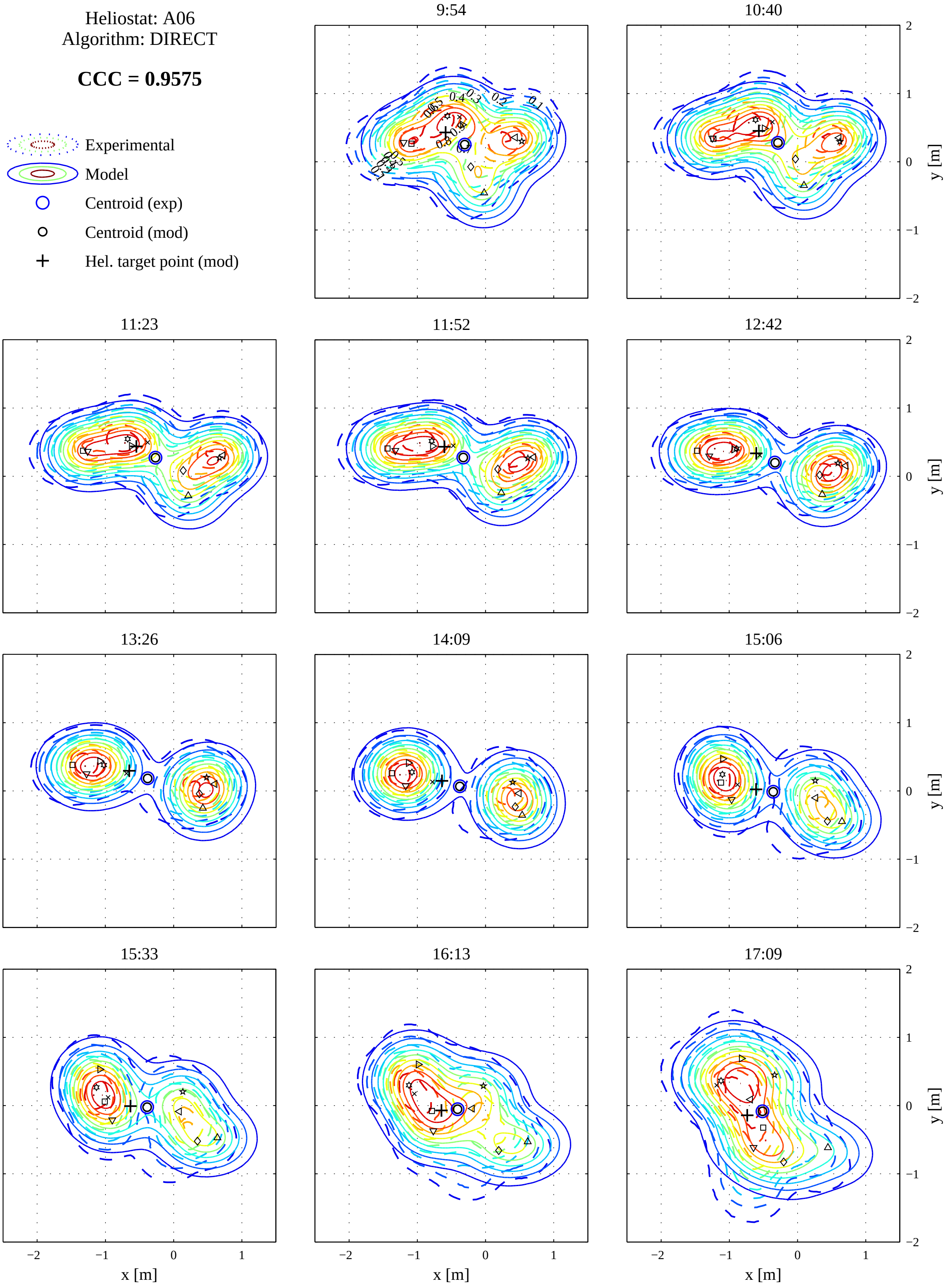

Figure 3.7: Contours of normalized flux density from heliostat A06 at different times in July 18, 2016. Experimental *vs.* model with optimized canting errors.

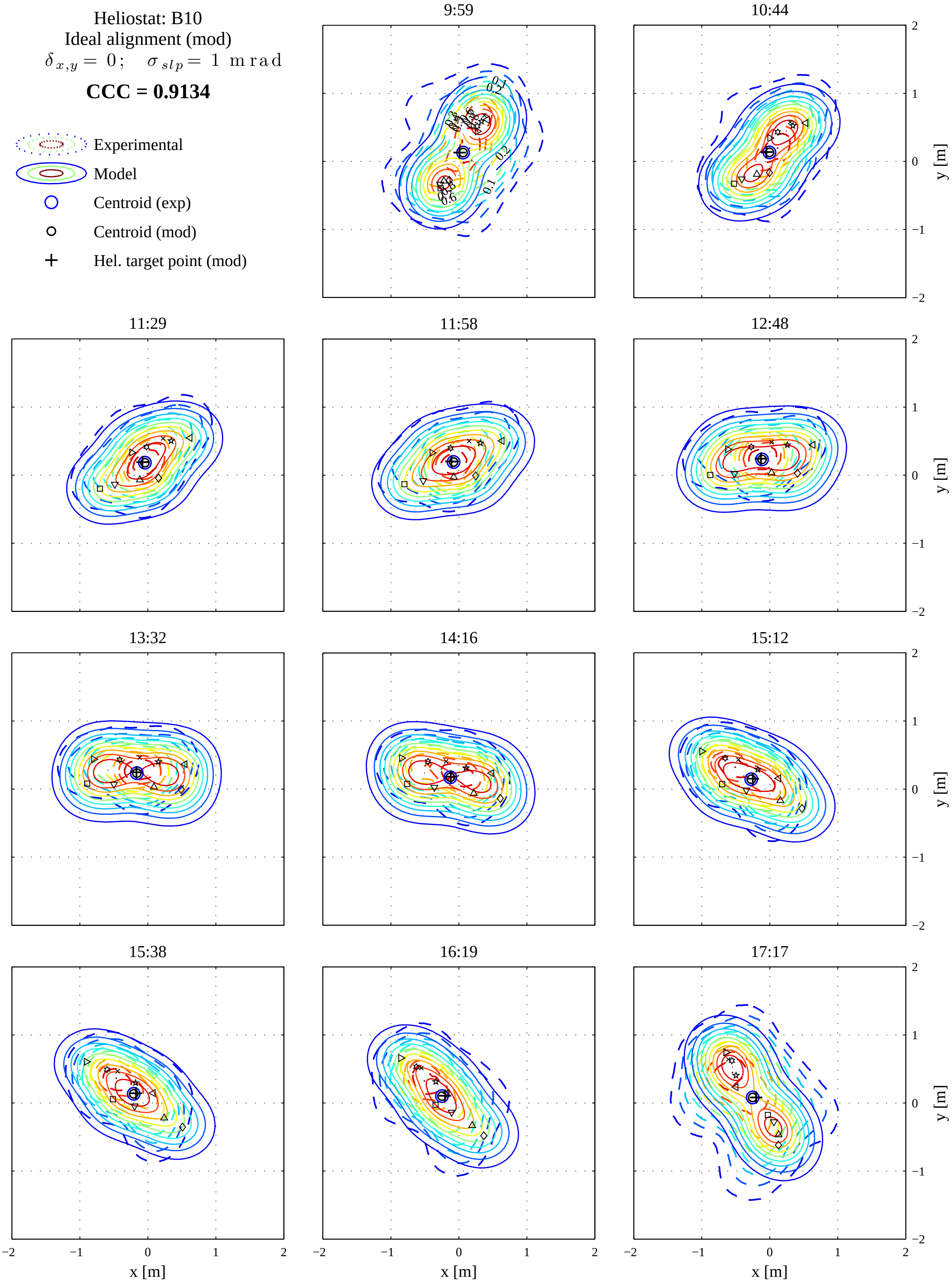

Figure 3.8: Contours of normalized flux density from heliostat B10 at different times in July 18, 2016. Experimental *vs.* model with ideal alignment.

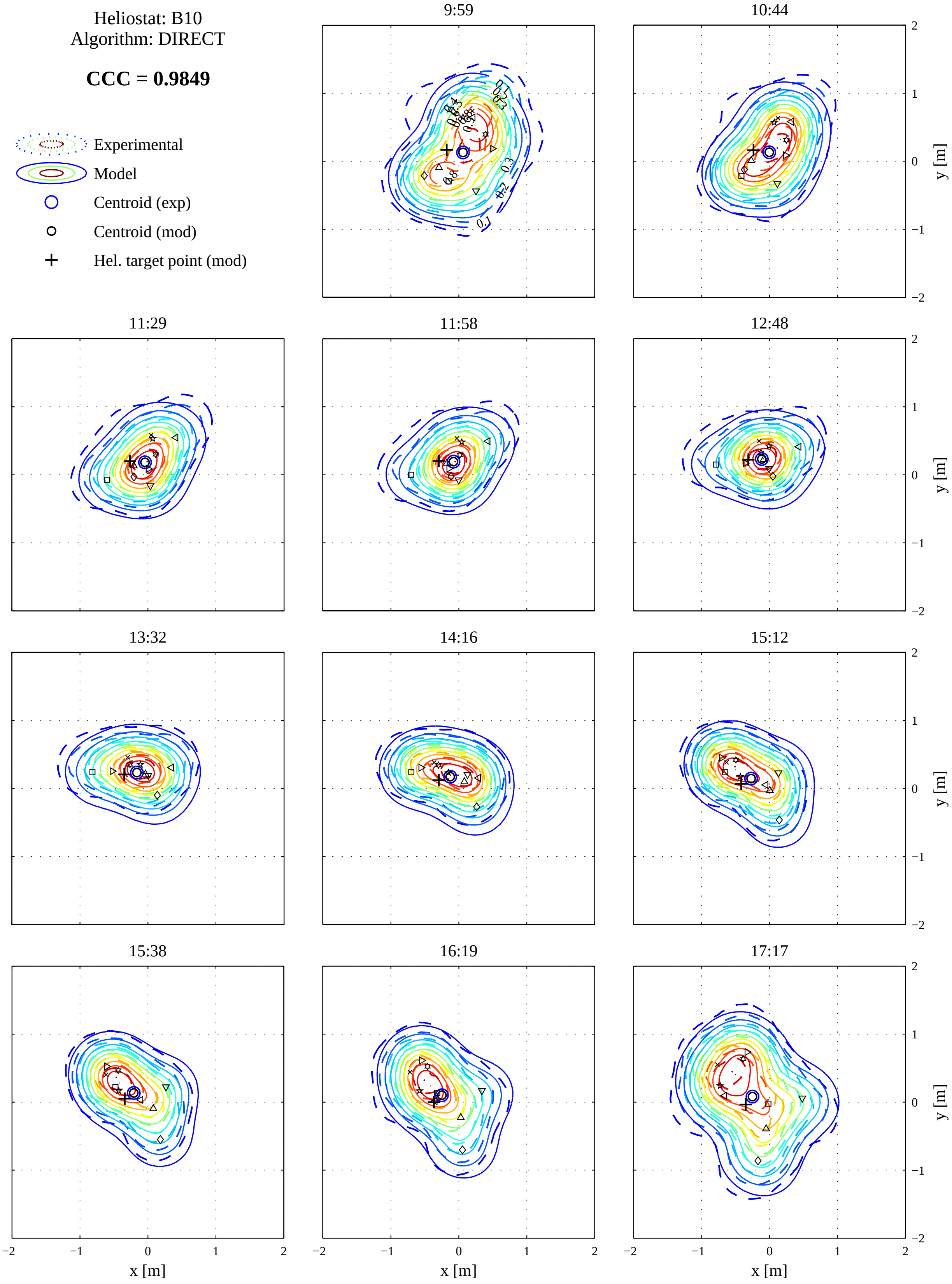

Figure 3.9: Contours of normalized flux density from heliostat B10 at different times in July 18, 2016. Experimental *vs.* model with optimized canting errors.

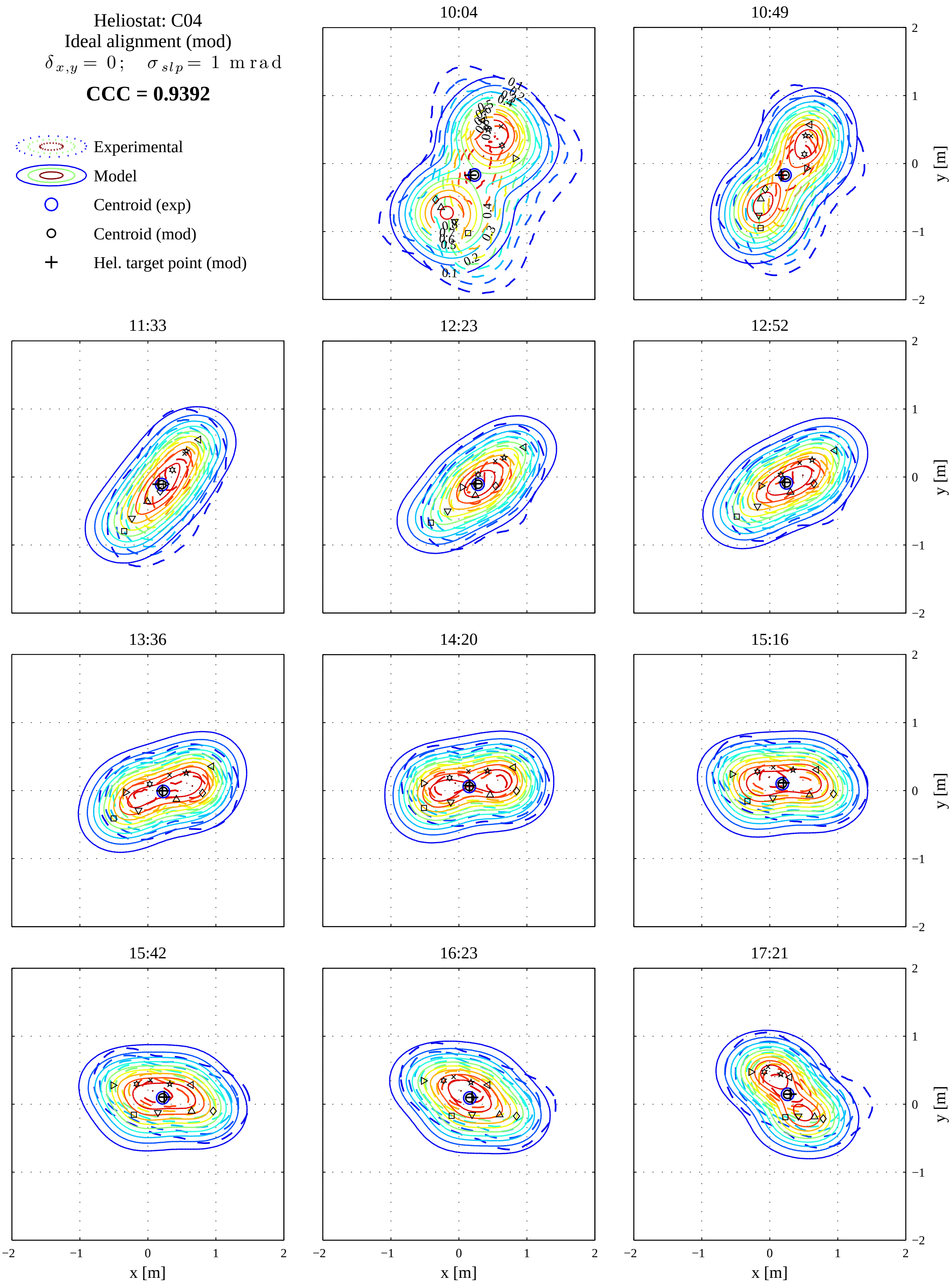

Figure 3.10: Contours of normalized flux density from heliostat C04 at different times in July 18, 2016. Experimental *vs.* model with ideal alignment.

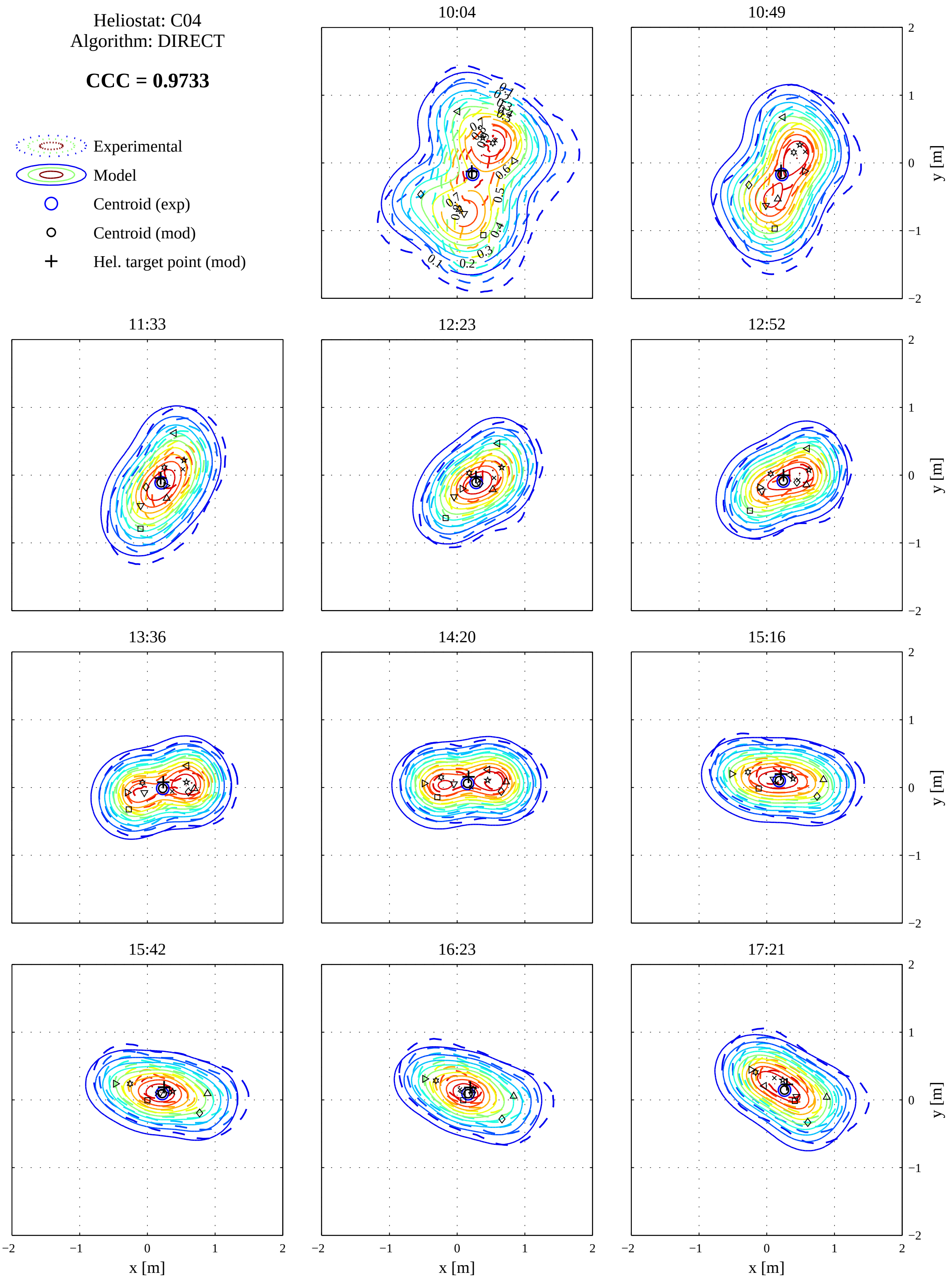

Figure 3.11: Contours of normalized flux density from heliostat C04 at different times in July 18, 2016. Experimental *vs.* model with optimized canting errors.

same. On the other hand, some defocus takes part on the target distribution, which can not be entirely handled by the optical model. In any case, correlation between experiment and model is reasonably high and the optimization algorithm provides a good estimation of the region of attraction to the perfect solution.

For A06, the heliostat with higher canting errors, the two-spot pattern is noticeably reproduced by the optimization method, Figure 3.7. From the inspection of the values in Table 3.2, it is seen that the major deviations are around the Y axes, i.e. δ_y. In addition to this, modules in the east wing are deviated to the east, while modules in the west wing are deviated to the west, except for module 8; as can be figured out from sign inspection in Table 3.2. This result is in agreement with the two lateral beams found in the central hours of the day.

3.5 Experimental validation

The validity of the proposed method to determine canting errors was assessed by *in situ* readjusting the mirror modules. The heliostat with higher canting deviations, heliostat A06, was selected to proof the validity of the methodology.

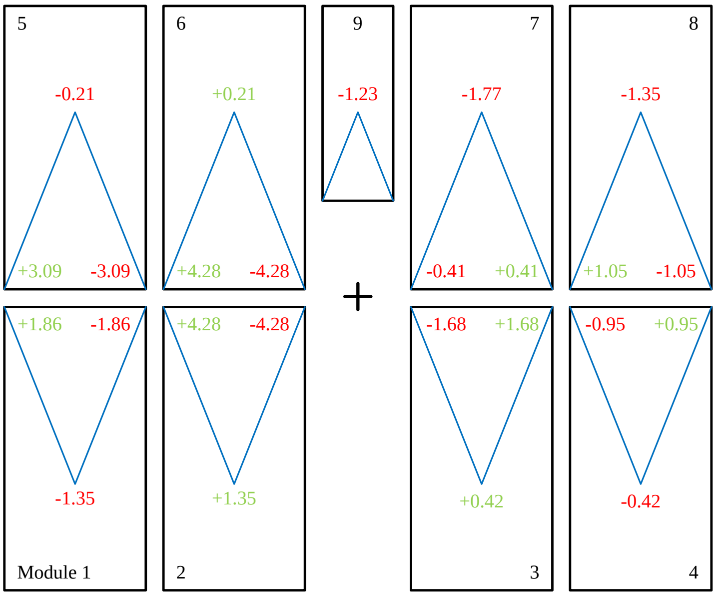

Sign convention: + forward (towards the tower); - backward (towards the ground)

Figure 3.12: Adjustment of nuts in heliostat A06. Linear movement in mm.

On the basis of the results presented in previous Section, the modules of heliostat A06 were canted in the field. This process was performed by turning the nuts that fasten the module frame to a fixed position. Each module is supported on the heliostat structure in three points by means of three screws, where the nuts are screwed. From the geometry of the module, angular errors in X and Y directions (Table 3.2) were transformed into linear movement of the nuts.

Figure 3.12 displays the displacement of the nuts prescribed for heliostat A06, with indication of the sign convention in accordance with that in Figure 3.3. Some of the movements are smaller than 1 mm, especially

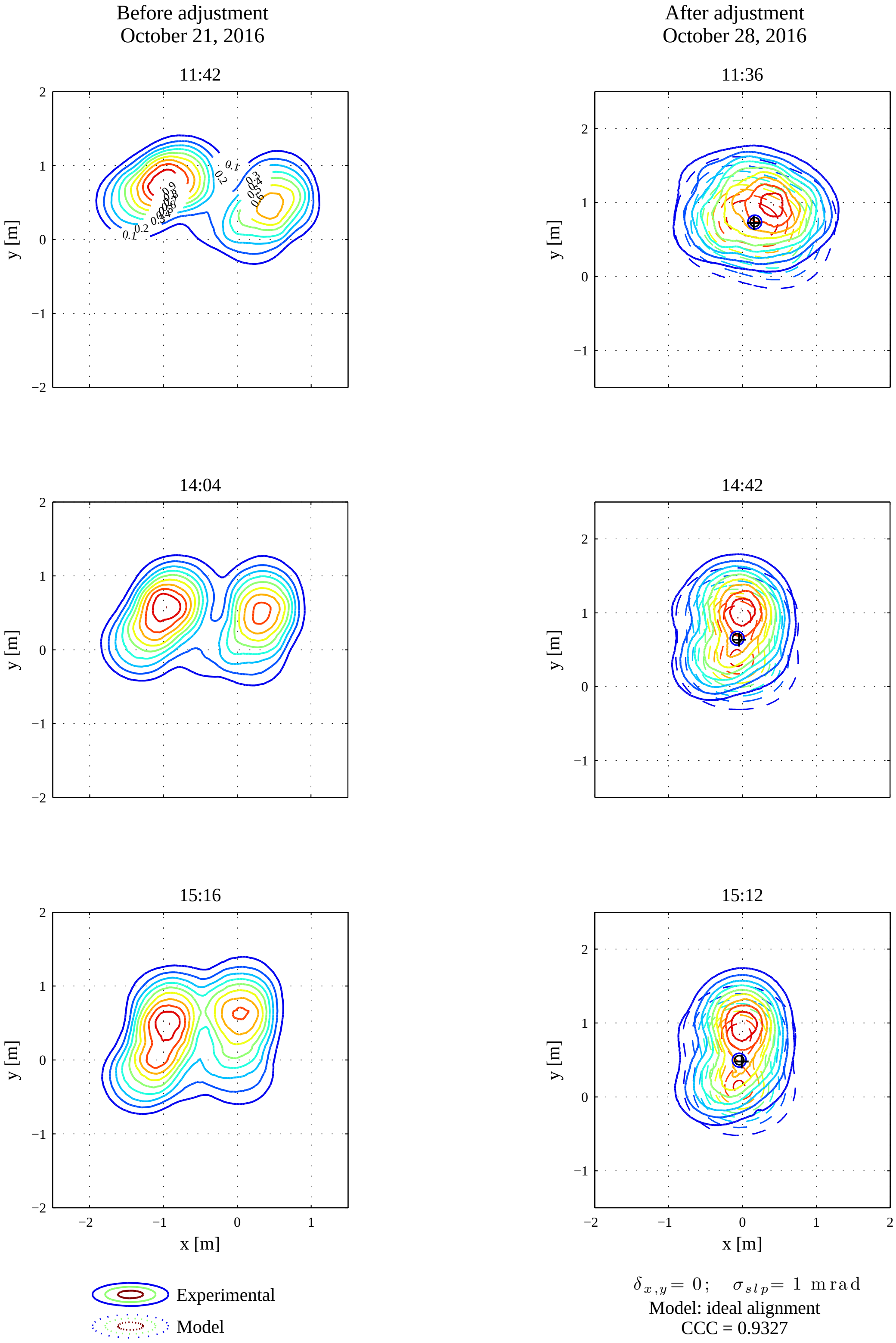

(a) Before recanting; experimental.

(b) After recanting; experimental *vs.* model.

Figure 3.13: Contours of normalized flux density from heliostat A06 before and after readjustment.

those in the central screws that modify δ_x. Such small resolution could result in execution inaccuracies, whose experimental error was estimated around 0.2 mm.

Adjustment of heliostat A06 was performed on October, 2016. To assess the validity of the methodology, images on the white target were captured before (October 21) and after (October 28) heliostat readjustment. Figure 3.13 shows the experimental contours of normalized flux density before (a) and after (b) adjustment at three similar instants of time.

Three months after the initial experimental campaign and without adjusting heliostat A06, the measured flux distribution was, as expected, still spread in two spots evolving along the day, Figure 3.13a. Once the heliostat was recanted, the optical quality of the heliostat significantly increased, leading to a single spot (i.e. more concentrated) on the white target, Figure 3.13b.

Besides the noticeable improvement in the beam quality of heliostat A06, experimental flux maps were compared to those simulated by the optical model for the case of ideal heliostat alignment. Figure 3.13b represents the contours of normalized flux density measured (solid lines) and simulated (dashed lines). Cross-correlation coefficient reaches a large value of 93.3%. Slight shift of the peak position respect to model prediction is found in the three instants of time. Sources of such deviation could be attributed to limitations of: the optical model that does not handle quasi-spherical mirror surface and astigmatism because of defocus; and, to a lesser extent, the optimization algorithm, and the imprecision in canting execution.

3.6 Conclusions

In this Chapter, a methodology to determine canting errors in real heliostats was established. On the basis of experimental flux distributions, an optimization procedure was defined to minimize the difference with simulated distributions. Angular deviations of mirror modules or facets were included in the optical model, on which an objective function was built up. The cross-correlation coefficient was used as the figure of merit in the cost function to maximize. Because of its deterministic approach and reliability, DIRECT algorithm was adopted to solve the optimization problem.

Such methodology was applied to three heliostats in THEMIS solar plant. For each heliostat, 28 images were captured on a white target along a whole day. In the absence of measurements of heliostat orientation, it was developed a procedure to infer the position of the target point, founded on matching the centroids of experimental and simulated maps. The optimization problem consisting in 18 unknowns (17 for the angular deviations and an extra one for the mirror slope error), was solved using DIRECT algorithm in less than 2 hours of computation. Substantial fitting between measured flux distribution and the solution was achieved with cross-correlation coefficients up to 98%.

Heliostat A06, with persistent two-spot flux pattern, was *in situ* readjusted according to the results obtained. Optical quality of heliotat A06 was remarkably improved, leading to a much more concentrated distribution with a single spot. Compared to the result expected by the optical model, *CCC* rose from 72.8% to 93.3%. As a consequence, the proposed methodology to find out canting errors has been validated for application to other heliostats.

Nomenclature

CCC	Cross-correlation coefficient [-]
F	Flux density [W/m^2]
FN	Normalized flux density [-]
IL	Intensity level [-]
N	Number [#]
$\mathbf{n}$	Heliostat normal vector
$\mathbf{s}$	Sun vector
SD	Standard deviation
SLR	Slant range [m]
$\mathbf{t}$	Target vector
$\mathbf{TP}$	Position of the target point
$\mathbf{WC}$	Position of the weighted centroid
X, Y, Z	Cartesian coordinate axes

Greek symbols

δ	Angular canting deviation [mrad]
σ	Gaussian error [mrad]

Subscripts

elts	Elements
exp	Experimental
max	Maximum
mod	Model
slp	Slope
sun	Sunshape

Acronyms

CCD	Charge-Coupled Device
CNRS	Centre National de la Recherche Scientifique
CRS2	Controlled Random Search, version 2
DIRECT	DIviding RECTangles
H-FACET	Heliostat Focusing And Canting Enhacement Technique
MCRT	Monte Carlo Ray Tracing
PROMES	PROcèdès, Matériaux et Energie Solaire
SNL	SANDIA National Laboratories
TOPCAT	Theoretical Overlay Photographic Heliostat Alignment Technique

References

Arora, J. S. 2012 Global Optimization Concepts and Methods. In *Introduction to Optimum Design*, chap. 18, pp. 681–712. Elsevier.

Biggs, F. & Vittitoe, C. N. 1979 Helios model for the optical behavior of reflecting solar concentrators. *Tech. Rep.*. Sandia National Laboratories, SAND-76-0347.

Chong, K. 2014 Non-imaging Focusing Heliostat. In *Advanced Energy Materials* (ed. Ashutosh Tiwari & Sergiy Valyukh), chap. 1, pp. 1–67. John Wiley & Sons, Inc.

Collado, F. J., Gómez, A. & Turégano, J. 1986 An analytic function for the flux density due to sunlight reflected from a heliostat. *Solar Energy* 37 (3), 215–234.

Finkel, D. E. 2003 DIRECT Optimization Algorithm User Guide.

Jones, D. R., Perttunen, C. D. & Stuckman, B. E. 1993 Lipschitzian optimization without the Lipschitz constant. *Journal of Optimization Theory and Applications* 79 (1), 157–181.

Jones, S. A. 1996*a* A comparison of on-axis and off-axis heliostat alignment strategies. In *American Solar Energy Society Conference*, pp. 95–100. Sandia National Laboratories, Asheville, NC (United States): SAND-96-0566C.

JONES, S. A. 1996*b* Annual performance prediction for off-axis aligned Lugo heliostats at Solar Two. In *American Society of Mechanical Engineers international solar energy conference*. Sandia National Laboratories, San Antonio, TX (United States): SAND-96-0212C.

JONES, S. A., EDGAR, R. M. & HOUSER, R. M. 1994 Recent results on the optical performance of solar two heliostats. In *American Society of Mechanical Engineers international solar energy conference*. Sandia National Laboratories, Lahaina, HI (United States): SAND-94-2776C.

KAELO, P. & ALI, M. M. 2006 Some variants of the controlled random search algorithm for global optimization. *Journal of Optimization Theory and Applications* 130 (2), 253–264.

NELDER, J. A. & MEAD, R. 1965 A Simplex Method for Function Minimization. *The Computer Journal* 7 (4), 308–313.

REN, L., WEI, X., LU, Z., YU, W., XU, W. & SHEN, Z. 2014 A review of available methods for the alignment of mirror facets of solar concentrator in solar thermal power system. *Renewable and Sustainable Energy Reviews* 32, 76–83.

SÁNCHEZ-GONZÁLEZ, A., CALIOT, C., FERRIERE, A. & SANTANA, D. 2017 Determination of heliostat canting errors via deterministic optimization. *Solar Energy* 150, 136–146.

SÁNCHEZ-GONZÁLEZ, A. & SANTANA, D. 2015 Solar flux distribution on central receivers: A projection method from analytic function. *Renewable Energy* 74, 576–587.

SCHMITZ, M., SCHWARZBÖZL, P., BUCK, R. & PITZ-PAAL, R. 2006 Assessment of the potential improvement due to multiple apertures in central receiver systems with secondary concentrators. *Solar Energy* 80 (1), 111–120.

SNL 2013 TOPHAT. *Theoretical Overlay Photographic Heliostat Alignment Technique* (https://ip.sandia.gov/technology.do/techID=16).

SPROUL, E., CHAVEZ, K. & YELLOWHAIR, J. 2011 The Development of the Heliostat Focusing and Canting Enhancement Technique: An Optical Heliostat Alignment Tool for the National Solar Thermal Test Facility. In *ASME 2011 5th International Conference on Energy Sustainability, Parts A, B, and C*, pp. 611–619. ASME.

THEODORIDIS, S. & KOUTROUMBAS, K. 2009 Template Matching. In *Pattern Recognition*, chap. 8, pp. 481–519. Academic press - Elsevier.

USNO 2016 Solar position. *Online calculator* (http://aa.usno.navy.mil/data/docs/AltAz.php).

YELLOWHAIR, J. & HO, C. K. 2010 Heliostat Canting and Focusing Methods: An Overview and Comparison. In *ASME 2010 4th International Conference on Energy Sustainability, Volume 2*, pp. 609–615. ASME.

YUAN, J. K., CHRISTIAN, J. M. & HO, C. K. 2014 Compensation of Gravity Induced Heliostat Deflections for Improved Optical Performance. *Journal of Solar Energy Engineering* 137 (2), 021016.

CHAPTER

FOUR

Symmetric flux maps from a field of heliostats: aiming factor approach

Contents

Summary

This Chapter presents a methodology to map the flux distribution on cylindrical receivers caused by a surrounding field of heliostats. The model validated in Chapter 2 was extended to superimpose the flux maps generated by every single heliostat in a field. All sources of optical losses were included in the code. Particular attention was paid to the computation of shading and blocking mirror areas, implemented by parallel projection of neighbor heliostats. Besides single equatorial aiming, it was developed a symmetric aiming strategy based on parameter k, named aiming factor. For the case study field consisting of 2650 heliostats, $k = 2$ yielded the most uniform distribution without substantial drop in the intercept factor. Required computation time is lower than one minute in a standard desktop computer.

4.1 Introduction

In Chapter 2 a model to accurately simulate the flux distribution from a single rectangular heliostat was introduced (Sánchez-González & Santana, 2015). In the present Chapter, that computational model is extended to the whole field of heliostats. All the optical loss factors are now considered, and special attention is paid to the computation of shading and blocking losses.

Two heliostat field aiming strategies for cylindrical receivers are presented: on one hand, the simplest strategy, single equatorial aiming; and, on the other hand, an original aiming strategy leading to symmetric flux maps.

In the symmetric aiming approach, heliostat target points are vertically shifted so that the beam is tangent to either the upper or the lower receiver edge. Such idea was firstly suggested by Vant-Hull (2002) and is further developed in the present Chapter.

Beam size is estimated on the basis of novel parameter k, named aiming factor and described in detail in Section 4.5. This parameter allows the mapping of different patterns of flux distributions with controlled spillage losses.

The field-receiver case study adopted throughout this work is presented in the next Section. The structure of the Chapter continues with the evaluation of optical losses, follows with the single aiming strategy and concludes with the symmetric aiming strategy based on k aiming factor.

4.2 Case study

The heliostat field and central receiver system of Gemasolar is used to illustrate the methodologies and results described in the following. Gemasolar, which is the first commercial solar power tower plant with molten salt storage, is sited in Fuentes de Andalucía, Spain, at 37.56° north latitude (Burgaleta *et al.*, 2011; Lata *et al.*, 2010).

Gemasolar field layout is surrounding and biased to the north, in correspondence with its cylindrical receiver and its northern hemisphere location. The field consists of an inner radial cornfield zone and two outer staggered zones. The coordinates of the 2650 heliostats were gathered through a scaled aerial photograph; land surface is supposed flat.

The layout of Gemasolar field is drawn in Figure 4.1. For cohesion and comparison purposes, Gemasolar heliostat field is considered in the remainder of this dissertation, even though other existing layouts were implemented such as Solar Two (Rodríguez-Sánchez *et al.*, 2015) and Crescent Dunes (Rodríguez-Sánchez *et al.*, 2014).

Gemasolar focusing heliostats are square with reflective mirror surface, AM, equal to 115.7 m^2 (Lata *et al.*, 2010). Mirror reflectivity is assumed ideal, $\rho = 1$, in the present Chapter for a better understanding of the rest of the optical loss factors.

Mirror slope error, σ_{slp}, is assumed to be 2.6 mrad (Augsburger & Favrat, 2013). On the contrary, tracking error is neglected, $\sigma_{trk} = 0$, since this parameter does not actually affect the flux distribution. The

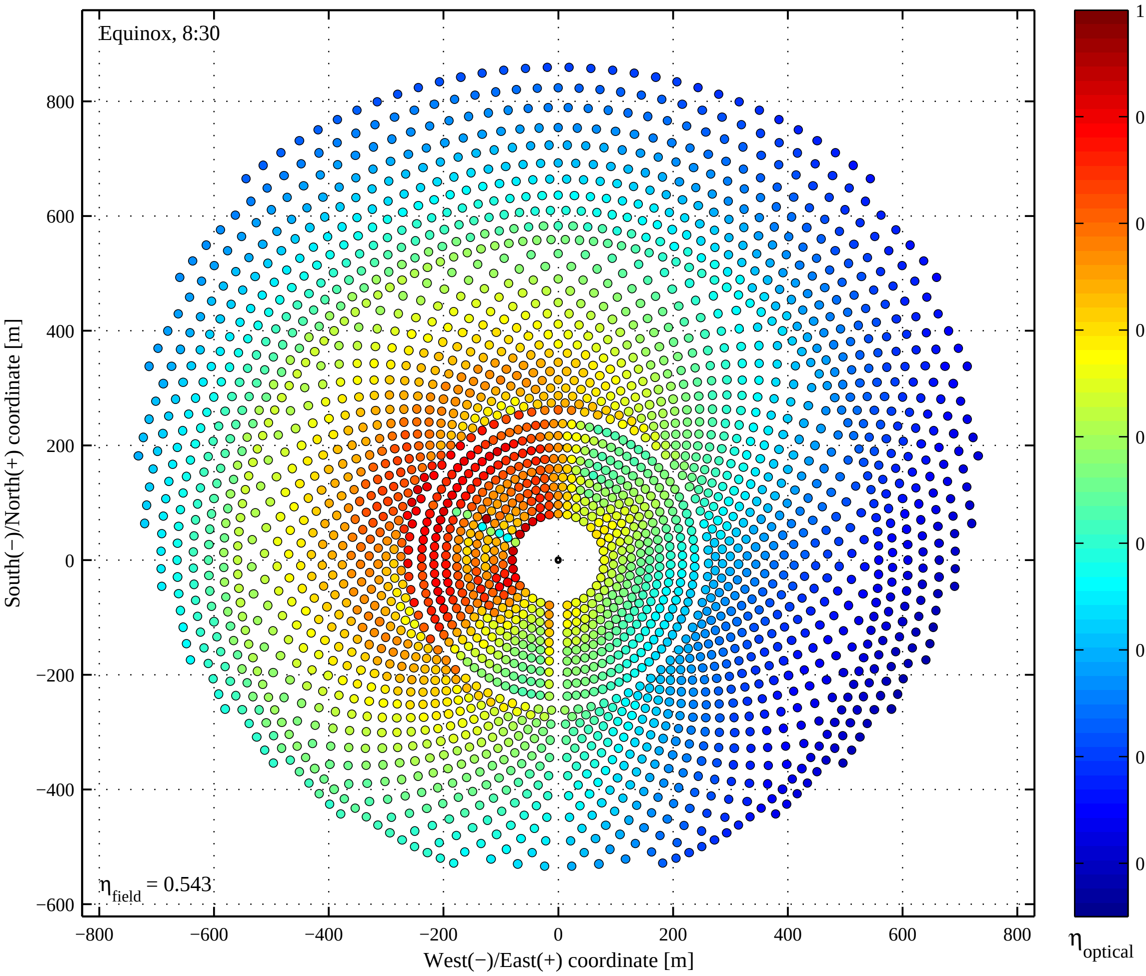

Figure 4.1: Layout of Gemasolar heliostat field and optical efficiencies at equinox at 8:30 solar time.

sunshape standard deviation σ_{sun} is that measured at PSA and equal to 2.51 mrad (Collado, 2008).

The central receiver is placed at the top of a tower, whose optical height (THT) is 120 m. The receiver comprises 18 panels (N_p) arranged around a cylindrical shell of 8.5 m in diameter (D) and 10.5 m in height (H). Receiver geometry is sketched in Figure 4.2. Each panel is named according to both the flow path (east and west) and the panel number from inlet to outlet.

4.3 Optical losses

The sources of optical losses in heliostats, depicted in Figure 4.3, are: the angle of incidence of solar radiation on the heliostat; mirror reflectivity; shading and blocking; atmospheric attenuation; and, spillage. For each of the just mentioned sources, an efficiency factor can be correspondingly defined: $\cos\omega_h$ (cosine factor); ρ; f_{sb}; f_{at}; and, f_{int} (intercept factor). The optical efficiency of a heliostat, η_h, is thus the product of all these factors:

$$\eta_h = \cos\omega_h \cdot \rho \cdot f_{sb} \cdot f_{at} \cdot f_{\text{int}} \tag{4.1}$$

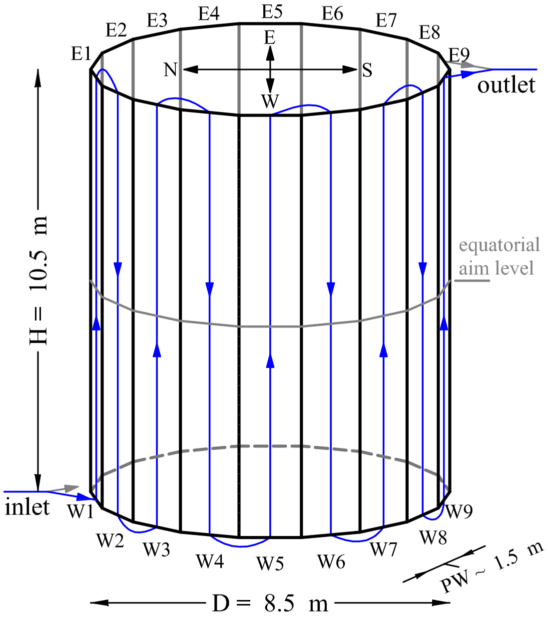

Figure 4.2: Receiver geometry. East and west panels are numbered from inlet (north) to outlet (south); west flow path is depicted in blue. Gray horizontal line designates the equatorial aim level.

The cosine factor, $\cos\omega_h$, and the intercept factor, f_{int}, were previously introduced in Chapter 2 in Equations (2.9) and (2.13). Their effect on the flux distribution is implicitly included in former Equation (2.11).

Mirror reflectivity, ρ, is not only a property of the mirror but also depends on its cleanliness, which is a parameter varying in time. The atmospheric attenuation factor, f_{at}, is primarily influenced by the distance of the heliostat to the target point, i.e. slant range (SLR); a detailed study of the effect of atmospheric attenuation can be found in Ballestrín & Marzo (2012). In the present study, it is adopted the following correlation (Leary & Hankins, 1979):

$$f_{at} = 0.99321 - 0.000176 \cdot SLR + 1.97 \cdot 10^{-8} \cdot SLR^2 \tag{4.2}$$

For the Gemasolar case study described in Section 4.2, Figure 4.1 shows the optical efficiency of the heliostats in the field at 8:30 on equinox. Optical losses were calculated with the aforementioned Equations. The computation of the shading and blocking factor, while considered in that Figure, is described in the following. The optical efficiency of the whole field of heliostats, 54.3%, results from the averaged heliostat efficiency:

$$\eta_{field} = \frac{\sum \eta_h}{N_h} \tag{4.3}$$

4.3.1 Shading and blocking

The shading and blocking factor, f_{sb}, is defined as the fraction of heliostat mirror that is neither shadowed nor blocked. Mathematically, it can be expressed through the following Equation; where AM_s stands for the area of the mirror that is shadowed, and AM_b, blocked.

$$f_{sb} = 1 - \frac{AM_s \cup AM_b}{AM} \tag{4.4}$$

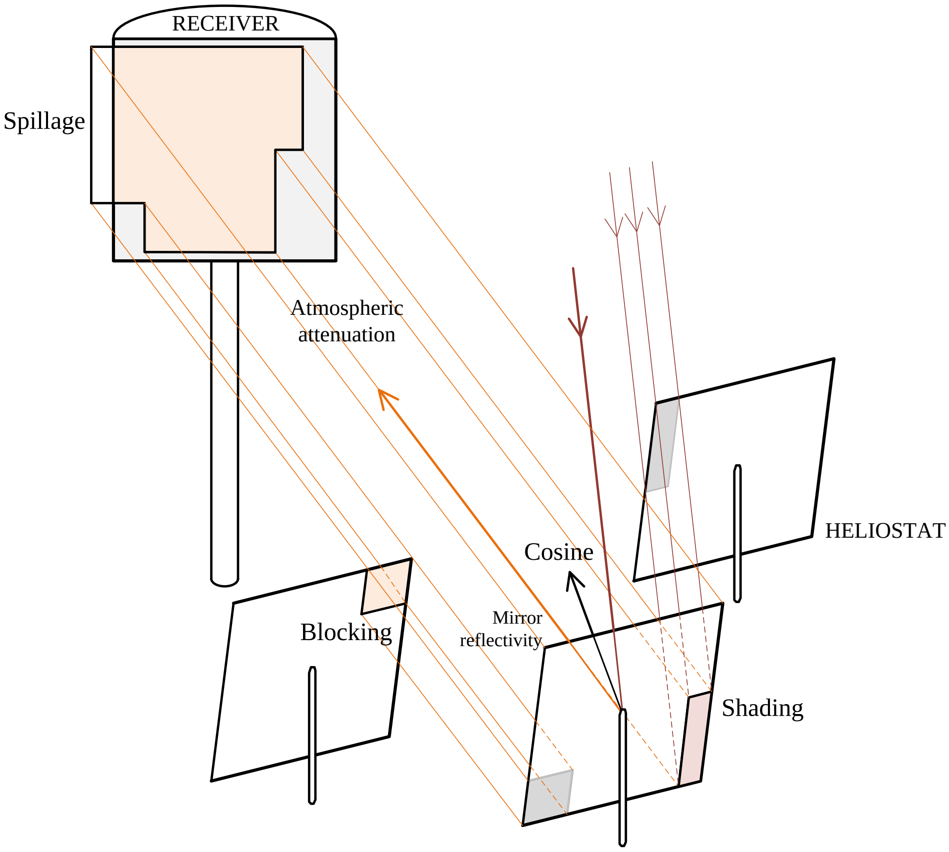

Figure 4.3: Heliostat optical losses. Adapted from Falcone (1986).

Several methods to evaluate shading and blocking areas have been reported (Huang *et al.*, 2013). Because of its speed of computation, parallel projection is utilized in this work. According to Lipps (1992), parallelism between neighbor heliostat planes may incur in a 7% maximum error in the conservative side.

The calculation of shadowing and blocking involves the projection of the rectangular outline of nearby heliostats in the directions of incident and reflected sun rays, respectively. Since angles and lengths are kept in parallel projection, just a single point must be cast. Basic vector operations for point projection are explained in detail in Collado & Guallar (2009).

Shading potential is initially assigned to fourteen neighbor heliostats, three of which may also block, similarly to Collado (2011). However, those neighbors behind the plane of the heliostat are finally removed, halving the number of neighbors projected. The shadowed/blocked mirror area is found in the intersection between the boundaries of the heliostat and those projected by its neighbors. Hence, a Boolean operation was progammed in the Matlab® code.

The computation of shadowed and blocked areas is uncomplicated in the plane of the heliostat. The transformation from global to heliostat coordinate system was stated in Equation (2.4). The calculation of shading and blocking factor was successfully compared with the results published in Collado & Guallar (2012).

Besides the shading of neighbor heliostats, the shadow projected by the tower on the heliostat field is

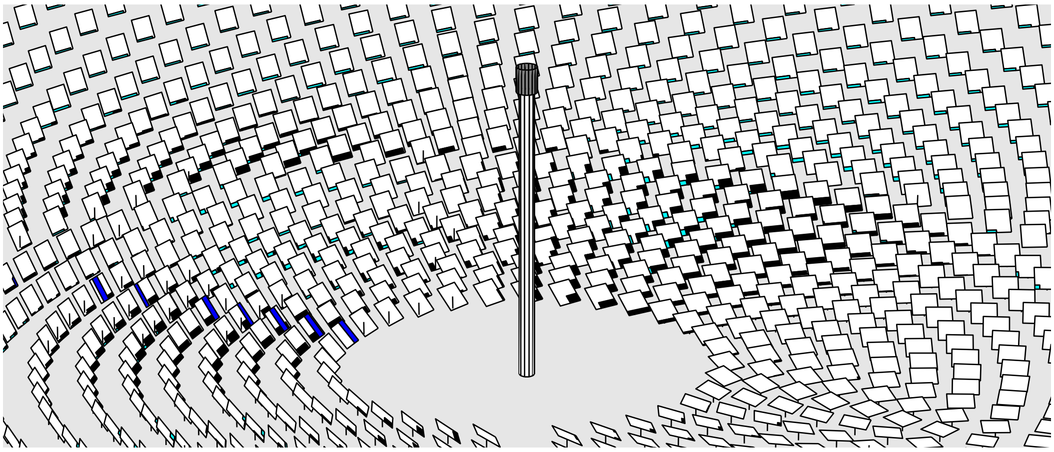

(a) 3D view from the south.

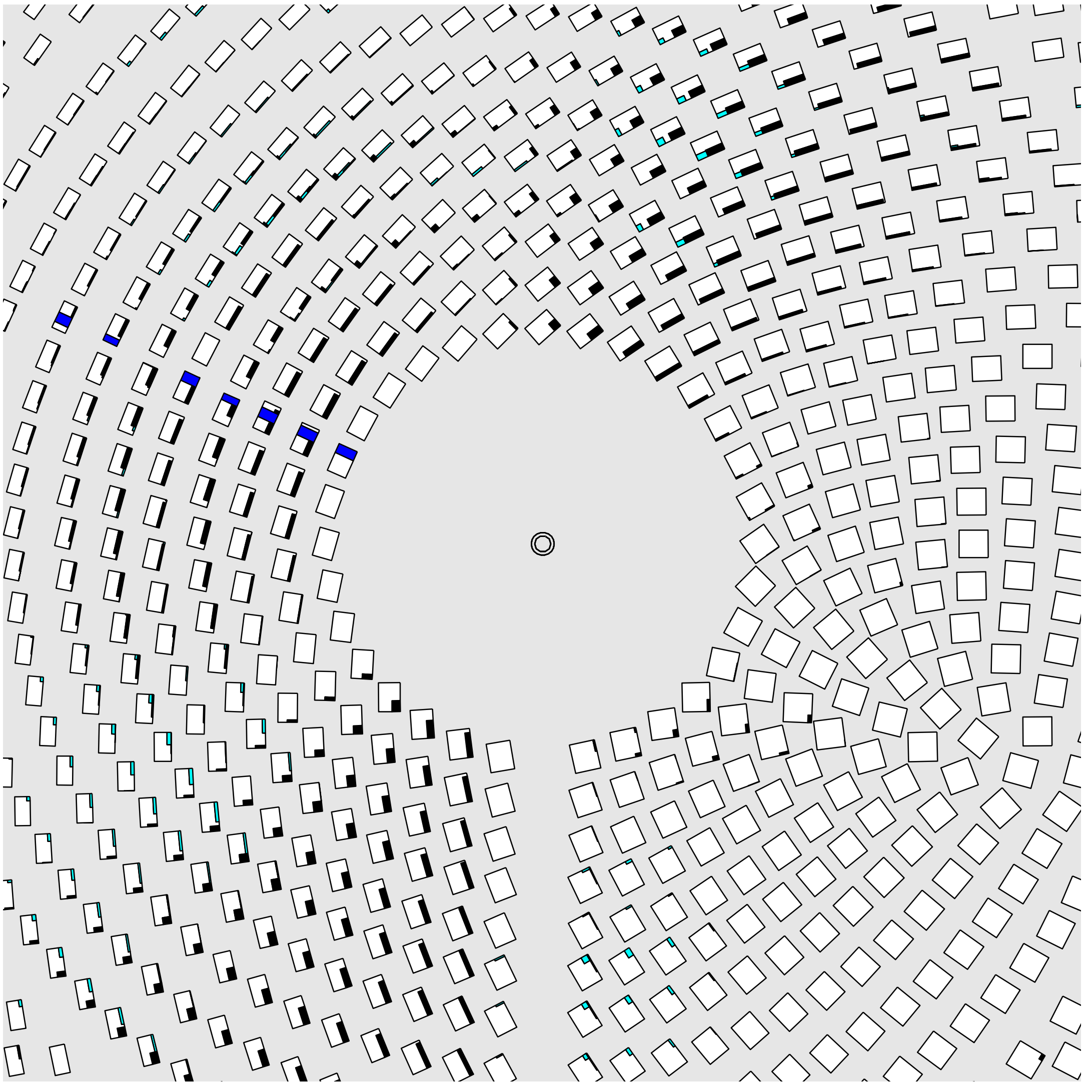

(b) Top view of the central region.

Figure 4.4: Shadings and blockings in Gemasolar field at equinox at 8:30 solar time. Mirror affected areas are colored in: blue (tower shadow); black (heliostat shadings); and cyan (heliostat bockings).

also computed in the code. Again for Gemasolar field at 8:30 on equinox, Figure 4.4 illustrates the shadowed and blocked areas in the heliostats. The color code is as follows: tower shadow in blue; heliostat shadings in black; and heliostat blockings in cyan.

4.4 Concentration map from a heliostat field

In Chapter 2 the calculation of the flux distribution from a single heliostat was introduced using the projection method. The validated model is now extended to integrate the distributions caused by a whole field of heliostats.

From Equation (2.11) it is gained the concentration ratio of flux density, $C_{i,j,p}$, on the receiver surfaces from a single heliostat; where $[i,j,p]$ stands for the nodes and panels of the receiver. That expression does not take into account the optical losses, except for cosine and spillage, which are implicitly included.

The concentration ratio considering optical losses, $C_{i,j,p}^{optloss}$, is calculated as the product of $C_{i,j,p}$ and the remaining optical loss factors; Equation (4.5). Therefore, this expression assumes that the concentration of flux is proportional to f_{sb}, which is feasible since shadowed and blocked mirror areas are usually small and the effective mirror boundary, rectangular or square, is almost unaltered during operation time.

$$C_{i,j,p}^{optloss} = \rho \cdot f_{sb} \cdot f_{at} \cdot C_{i,j,p} \tag{4.5}$$

To obtain the concentration ratio of flux density from a whole heliostat field, the concentration by each heliostat obtained from Equation (4.5) is summed in every single node on the receiver mesh. Since the receiver mesh is unique, the addition is direct and straightforward. Mathematically, this is expressed as:

$$C_{i,j,p}^{field} = \sum_{heliostats} C_{i,j,p}^{optloss} \tag{4.6}$$

Other simulation tools (e.g. RCELL, DELSOL3) consider a representative heliostat for a region (rectangular cell or circular sector) in the field (Lipps & Vant-Hull, 1978; Kistler, 1986). Contrary to the representative heliostat approach, the proposed model considers all the heliostats in the field for two reasons: the resulting flux distribution is more accurate; and it takes limited computation time for the whole field. For the Gemasolar case study, the computation last around 45 s in a standard desktop PC.

4.4.1 Single aiming

This is the simplest aiming approach, where the heliostats point at a fixed height level in the receiver. The aim level is the equatorial line, in the horizontal mid-plane of the receiver (see Figure 4.2). To minimize lateral spillage losses, the azimuth of the aim point in the receiver equator is that of the pointing heliostat; in other words, the reflected beam is coplanar with the vertical axis of the receiver and the tower.

Given the Gemasolar case study introduced in Section 4.2, the overall distribution of flux density on the receiver was computed by means of Equation (4.6). The map of concentration ratio at 8:30 on equinox is shown in Figure 4.5 both in a tridimensional view of the receiver (b), and in a 2D plot on the unfolded surface of the 18-panels cylindrical receiver (a). Each panel is named according to both the flow path (east and west) and the panel number from inlet to outlet.

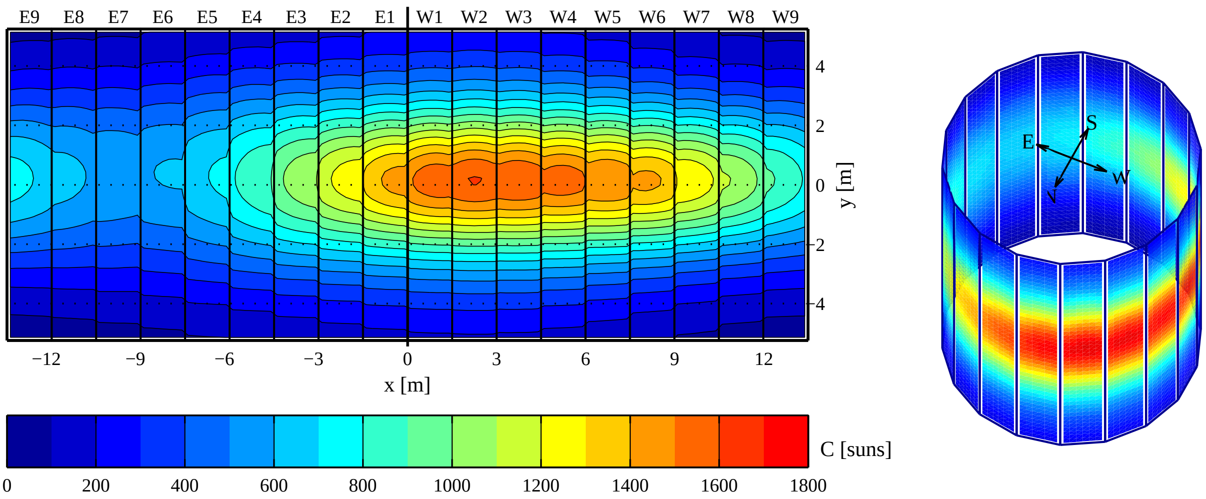

(a) Unfolded 2D view.

(b) 3D view.

Figure 4.5: Map of concentration ratio of flux density at equinox at 8:30 solar time for single equatorial aiming.

The mean concentration ratio of flux density on the receiver at equinox 8:30 is 588, which represents the flux density of 588 suns. If the direct normal irradiation, DNI, at that instant of time is known, the map of flux densities results from simple multiplication by the DNI; Equation (2.1). In the present Chapter, flux maps are represented in levels of adimensional concentration ratio of flux density, C.

The maximum flux concentration, 1604, is located in panel W2, indeed coinciding with the anti-sun location. Regarding optical losses in the field, intercept factor and optical efficiency are respectively 83.2% and 54.4%. These optical factors represent the upper limit for equinox at 8:30 since single aiming yields the lowest spillage in a field.

In the following, summer solstice day is considered. Similarly to the preceding Figure, the concentration map is shown in Figure 4.6, but now at summer solstice noon. On the right side of the Figure it is shown the vertical profile of flux concentration in the middle of the most irradiated panel in the receiver.

Symmetry about the north direction is found, as expected at noon for a surrounding heliostat field. Although all heliostats are aimed at the receiver equator, $y = 0$, for any x-coordinate the peak is found slightly above that line; see profile on the left side. This is because panels adjacent to the target one are reached somewhat above the aim level. This effect was also revealed for individual heliostats (e.g. Figure 2.11) and is also a constant for the whole field with single aiming (Figure 4.5).

Mean and maximum concentration ratios are 701 and 1694, respectively. Factor of interception and optical efficiency are respectively 84.7% and 64.8%. All these key values at summer solstice noon are higher than those above pointed out for 8:30 solar time at equinox, where solar altitude is 28.9° versus 75.9° at summer solstice noon. In consequence, cosine and shading and blocking factors of the field ($\cos\omega$ and f_{sb}) rise correspondingly from 75.5% and 94.6%, to 82.4% and 99.9%.

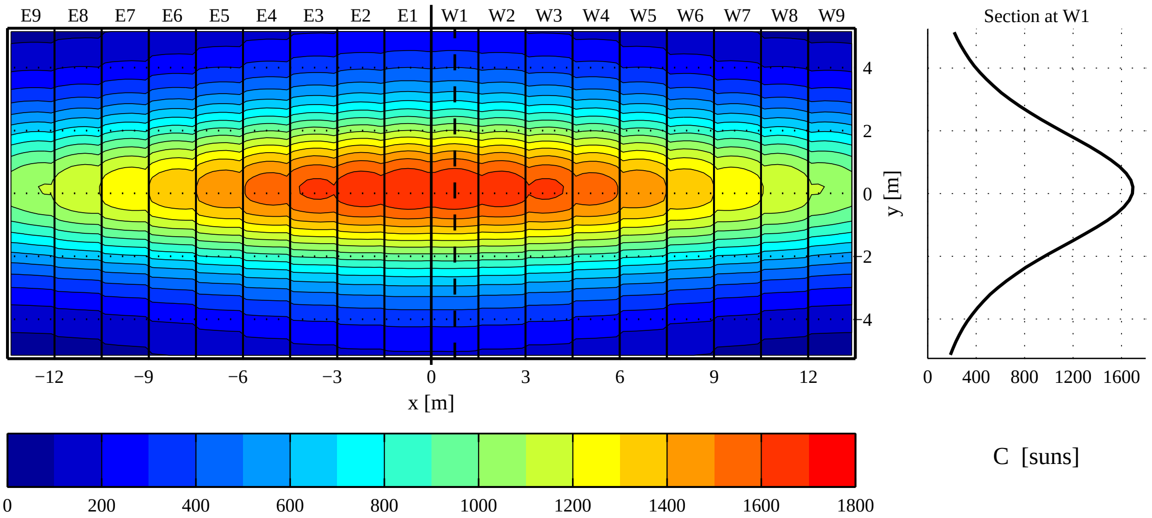

Figure 4.6: Map of concentration ratio of flux density at summer solstice noon for single equatorial aiming.

4.5 Symmetric aiming

Single aiming strategy leads to hot spots on the receiver, as has been shown in previous Section. Flux distributions that are markedly non-uniform induce extreme thermal gradients and stresses, which have to be avoided or minimized. Multi-aiming strategies seek to flatten the flux distribution on the receiver (Besarati *et al.*, 2014).

This Section puts forward a simple aiming strategy which results in flux maps that are nearly symmetric about the receiver equator. The proposed aiming strategy is build upon the concept of k aiming factor, which is explained in the next Subsection. Based on k parameter, different flux maps with different spillage losses are generated, as will be shown in the final Subsection for the whole field.

The present aiming strategy entails the adjustment of each heliostat target position along the vertical direction on the receiver surface. Azimuth of target points is that of its pointing heliostat. Thus, vertical shifting is only considered, in contrast to horizontal shift which is not allowed to minimize lateral spillage.

The proposed symmetric aiming strategy, graphically summarized in Figure 4.7, essentially consists in the following two steps:

1. The radius of the incident beam on the receiver vertical, BR_k, is estimated for a given k factor.
2. The target point T_k is vertically shifted so that the beam circumference on the receiver is tangent to either the upper or the lower receiver edge.

In order to procure nearly symmetric flux maps from the whole field, each row of heliostats is alternatively aimed to the top and to the bottom half of the receiver, as suggested by Vant-Hull (2002). Herein, even rows of heliostats aim tangentially to the lower edge, while odd rows to the upper edge; as pointed out in Figure 4.7.

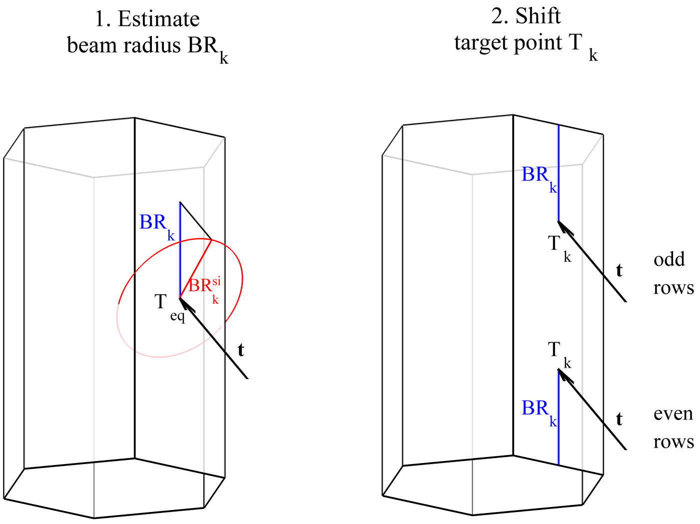

Figure 4.7: Symmetric aiming process.

When the beam diameter computed in step 1 is greater than the receiver height (H), the corresponding heliostat is aimed at the middle equatorial line. This fact typically takes place in heliostats far from the receiver. In this manner, spillage losses above and below the receiver are also reduced.

4.5.1 Beam size based on aiming factor

The proposed aiming strategy relies on a proper estimation of the size of the beam incident on the receiver (step 1). In the following, it is introduced a calculation procedure based on k aiming factor.

In Subsection 2.2.4 it was shown that the flux distribution on the image plane follows a rather circular Gaussian distribution with effective standard deviation, σ_e, according to Equation (2.10). By analogy with the normal distribution, 68%, 95% and 99.7% of the total flux is within a cone of aperture angle from heliostat center σ_e, $2\sigma_e$ and $3\sigma_e$, respectively.

Assuming circular normal distribution, the radius of the beam on the image plane (si) can be calculated with Equation (4.7) for a heliostat at distance SLR to the receiver (equatorial target point). The beam radius by Equation (4.7) depends on parameter k; the higher the k value, the larger the estimated beam circle is. Generally, k ranges between 0 and 3 in line with the 68-95-99.7 rule for normal distribution.

$$BR_k^{si} = SLR \cdot \tan\left(k \cdot \sigma_e\right) \simeq SLR \cdot k \cdot \sigma_e \tag{4.7}$$

Figure 4.8 shows the flux distribution on the image plane (left) and its cross-section (right) from a heliostat in Gemasolar field. Specifically, such flux distribution is produced at summer solstice noon by the heliostat placed in the first row and whose azimuth is true east. Beam circumferences at the image plane for three k values (1, 2 and 3) are drawn in Figure 4.8. The beam diameter ($BD = \frac{BR}{2}$) is calculated with Equation (4.7).

On the surface of the receiver, the flux distribution is projected from the image plane, as explained in Chapter 2. Similarly, the beam circumference is projected on the receiver panels, which is equivalent to the intersection of the cone of light and the receiver.

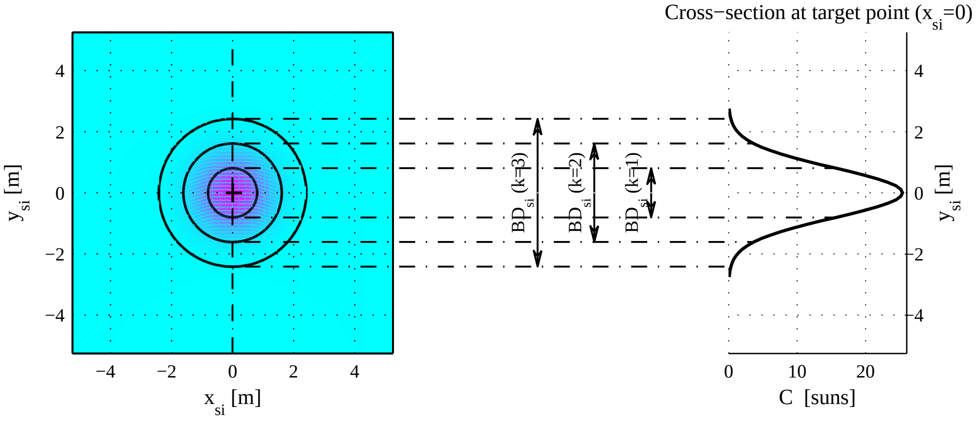

Figure 4.8: Beam diameter at image plane; estimation for several aiming factors.

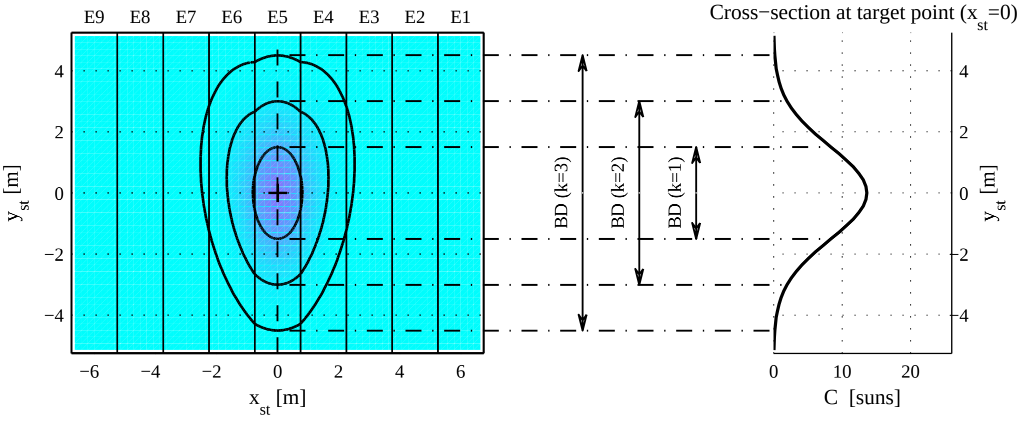

Figure 4.9: Beam diameter on receiver surface; estimation for several aiming factors.

Figure 4.8 shows the flux distribution on the half visible side of the receiver; east side for the previous sample heliostat. The projection from the image plane of the circumferences given three k values are marked in the Figure. The vertical cross-section of the concentration contours is again placed on the right of the Figure.

For the purposes of the symmetric aiming strategy in the present Chapter, rather than the calculation of the whole boundary of the beam cone, is only needed the beam size on the vertical of the receiver. Recall that in step 2 the beam spot is targeted tangentially to the upper or lower edge of the receiver by vertical shift.

Known the elevation angle of the target vector, ϵ_t, the radius of the beam on the receiver vertical BR_k can be easily calculated from that on the image plane:

$$BR_k = \frac{BR_k^{si}}{\cos \varepsilon_t} = \frac{SLR \cdot k \cdot \sigma_e}{\cos \varepsilon_t} \tag{4.8}$$

To sum up, step 1 in the aiming strategy implies the calculation of the beam radius on the receiver vertical, BR_k, according to Equation (4.8).

4.5.2 Targeting

In step 2, the heliostat is pointed at a distance BR_k from the edge. Equivalently, the target point is shifted at a vertical distance from the middle point equal to $\frac{H}{2} - BR_k$, where H is the receiver height.

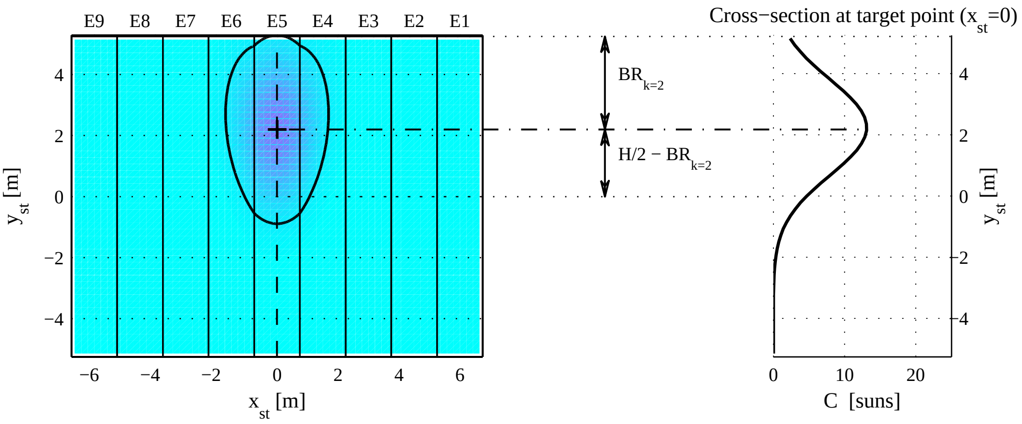

Figure 4.10: Shifted target point; beam tangent to upper edge ($k = 2$).

For the sample heliostat used in the preceding Subsection, Figure 4.10 illustrates the concentration map for $k = 2$. Again, on the right is shown the vertical profile of concentration ratio.

It can be easily deduced that the lower the value of k, the higher the spillage losses are. This is why parameter k was named aiming factor, since it affects the position of the target point. Actually, k aiming factor represents a parameter to control the spillage losses.

4.5.3 Symmetric maps from a field

The aiming strategy just explained for a single heliostat, is now extended to the whole field of heliostats. For any k aiming factor, beam radii of all the heliostats are calculated from Equation (4.8) (step 1) and their corresponding target points are set (step 2).

To achieve symmetric flux maps, heliostats in alternative rows are aimed to the top and bottom part of the receiver. For convention, heliostats in even rows are aimed to the top, and vice versa. For heliostats where the diameter of the beam is larger than the receiver height ($BD > H$), the target point is placed in the middle equatorial line.

In the following, it is presented the maps of concentration ratio for the Gemasolar case study at summer solstice at several solar times. Different aiming factors are considered and colormap scales are kept fixed for proper comparison.

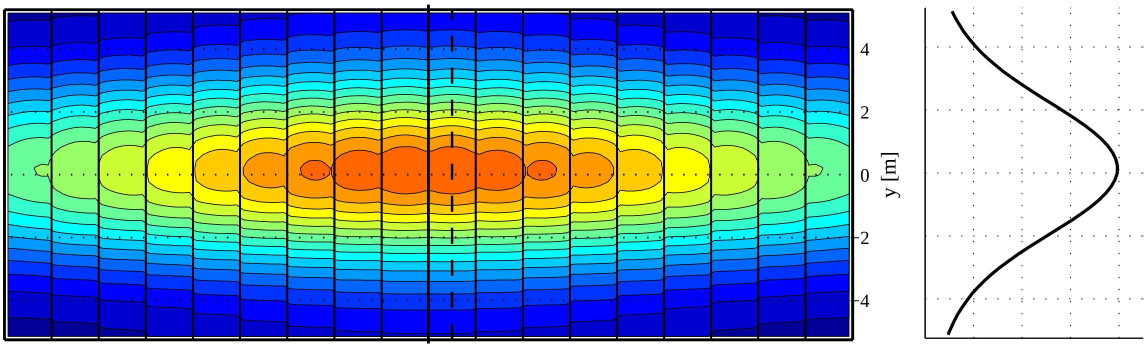

(a) $k = 3$

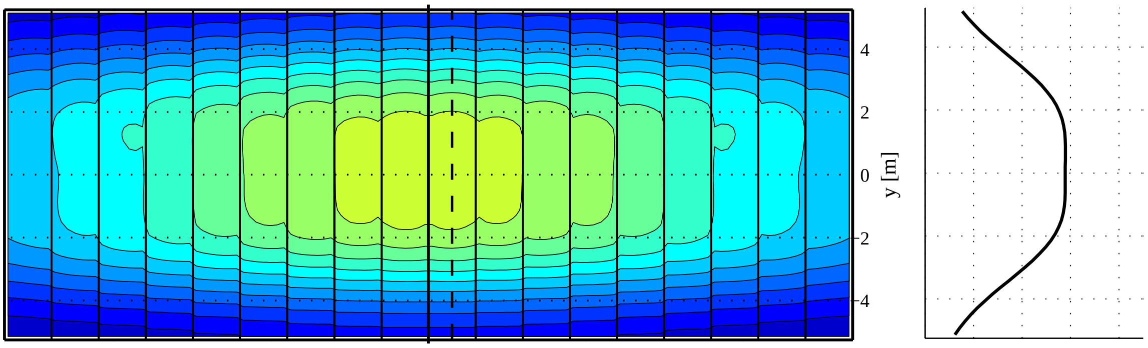

(b) $k = 2$

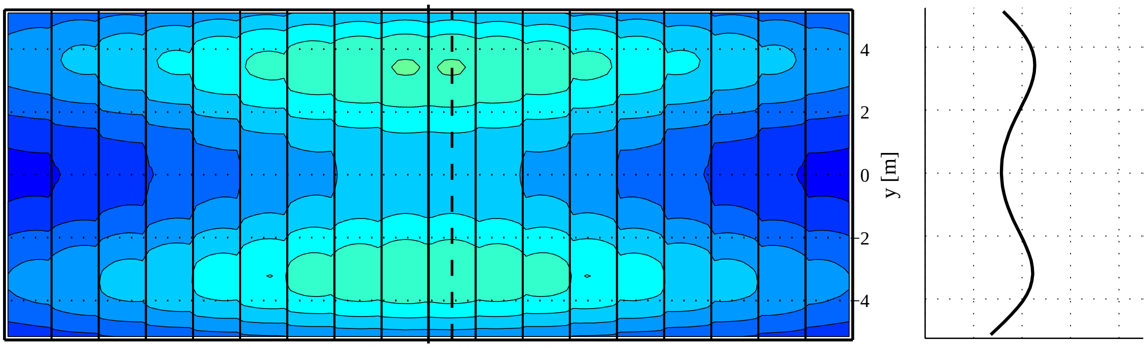

(c) $k = 1$

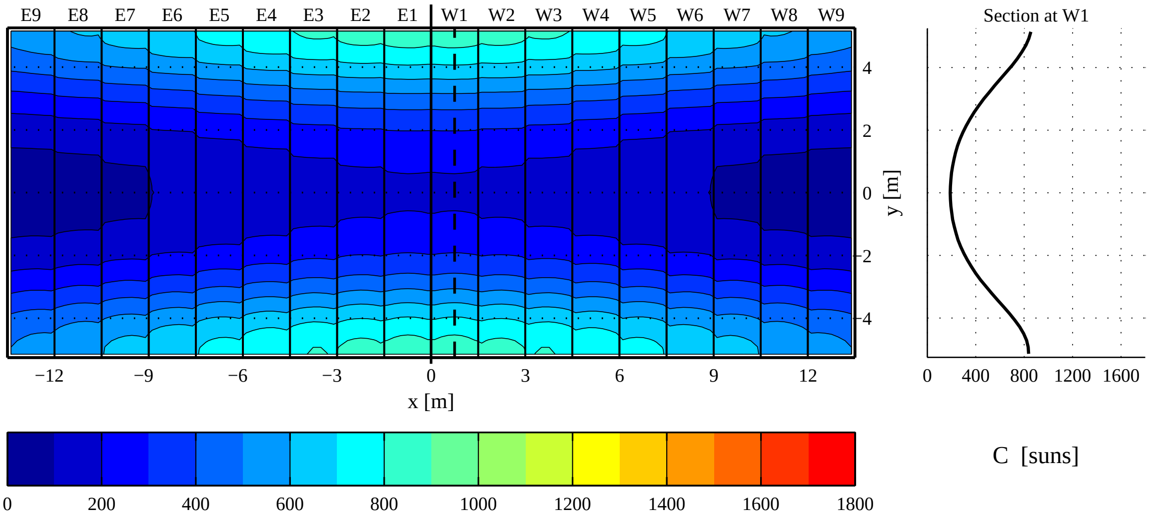

(d) $k = 0$

Figure 4.11: Maps of concentration ratio of flux density at summer solstice noon for different aiming factors.

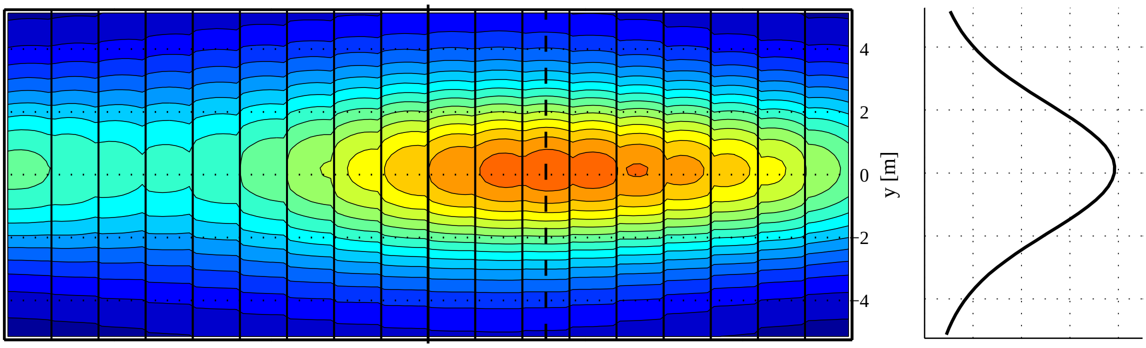

(a) $k = 3$

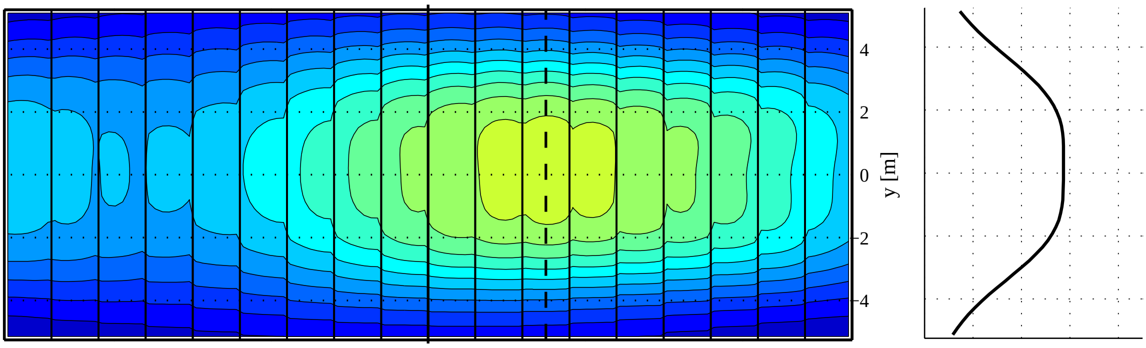

(b) $k = 2$

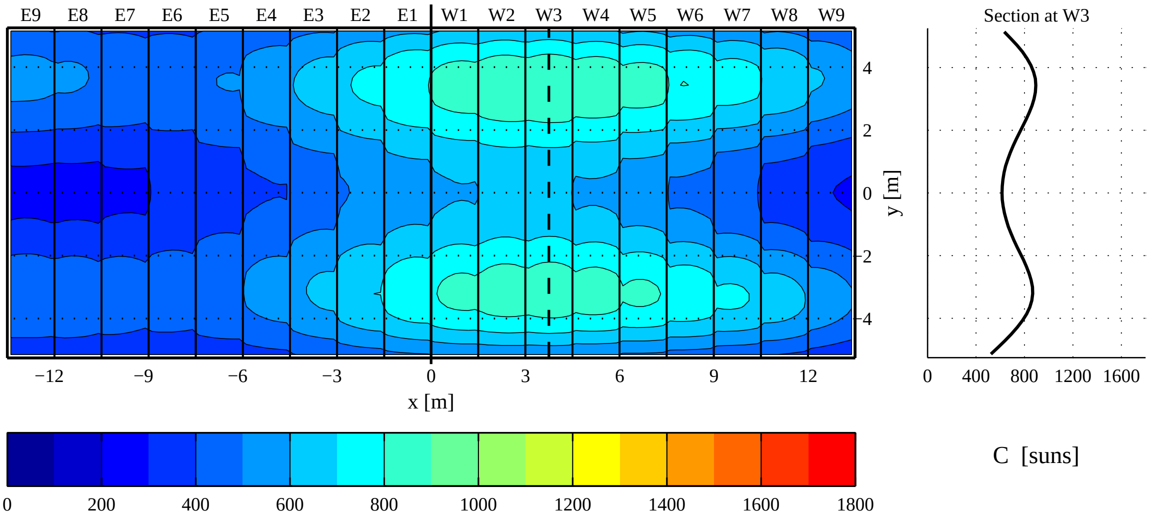

(c) $k = 1$

Figure 4.12: Maps of concentration ratio of flux density at summer solstice at 9:00 solar time for different aiming factors.

At summer solstice noon, 12:00 solar time, concentration maps are depicted in Figure 4.11. Four different aiming factors were considered (0, 1, 2 and 3). Flux map for $k = 3$ is similar to that with equatorial aiming in Figure 4.6 with a clear hot strip on the equatorial belt. However, peak concentration is reduced from 1694 to 1588, while the mean concentration, 701, is kept constant, as well as the intercept factor. This means that the total received flux is the same in both cases, equatorial and $k = 3$.

For $k = 0$, instead of a peak in the middle, two peaks emerge in the edges (see concentration profiles on

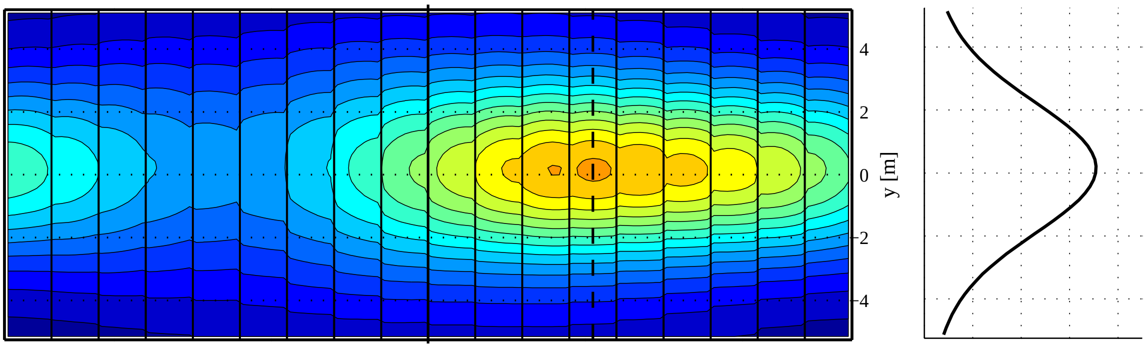

(a) $k = 3$

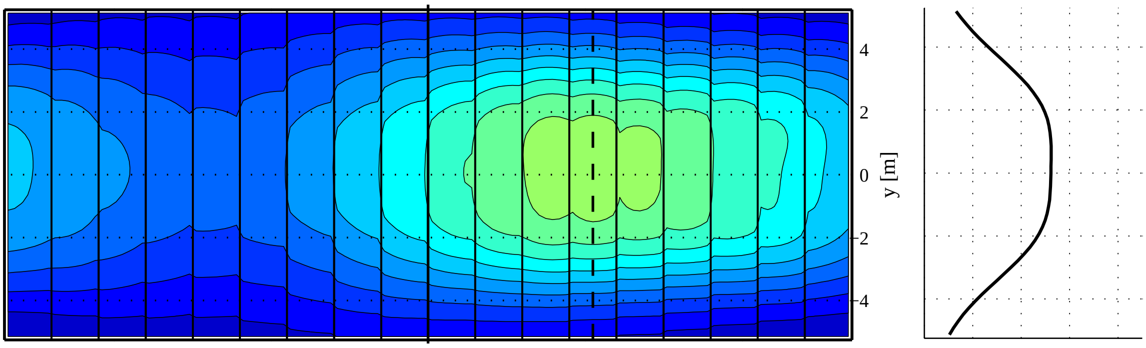

(b) $k = 2$

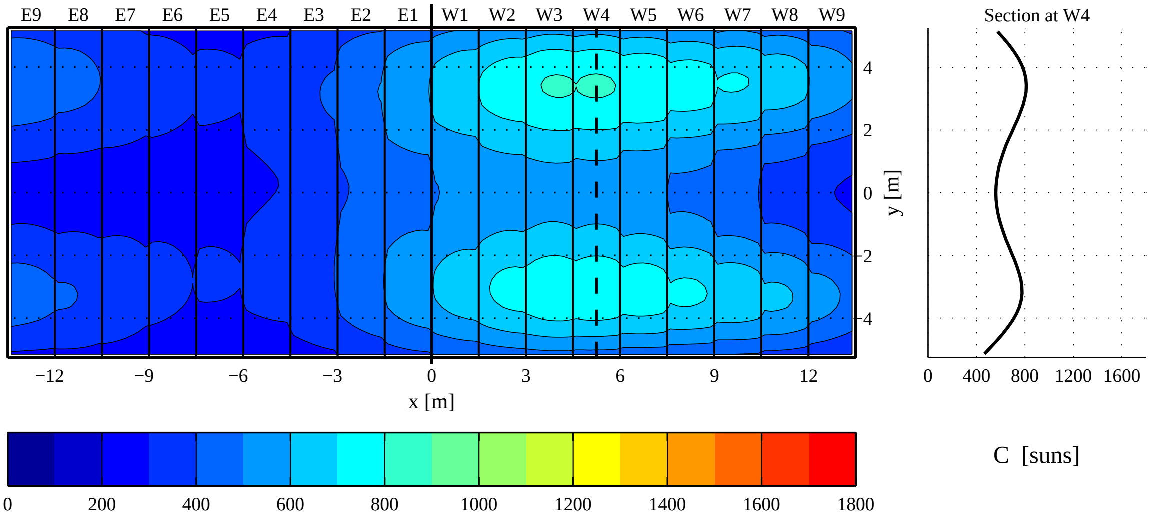

(c) $k = 1$

Figure 4.13: Maps of concentration ratio of flux density at summer solstice at 7:00 solar time for different aiming factors.

the right margin). This aiming strategy is fairly inefficient; less than 50% intercept factor. In the following, graphical results from such aiming factor are avoided.

Aiming factors between the extremes, i.e. 1 and 2, produce flux maps also in between. For $k = 1$, Figure 4.11(c), the two shoulders on the profile have just appeared. Meanwhile, $k = 2$ generates a noticeably flat distribution in the middle; which is beneficial in terms of thermal stress and uniform heating.

At 9:00 solar time, Figure 4.12, the patterns of flux distribution are similar to those at noon for every aiming factor. Naturally, the peak is horizontally displaced to the panel at the anti-sun location; panel W3. The peak and the mean concentrations are somewhat smaller than those at noon, as can be deduced from the profiles and the color levels. A smaller angle of incidence on the heliostats, ω_h, caused by a lower solar altitude ($\epsilon_s = 49.2°$) is the main reason behind such reduction.

At 7:00 solar time ($\epsilon_s = 25.5°$), flux levels are again smaller and the most irradiated panel is W4; Figure 4.13. In any case, the pattern of flux distribution on the receiver is fairly similar to those at other times. Flat profile in the central region is gained with $k = 2$.

Key figures for the three selected solar times and different aiming factors are listed in Table 4.1 for inspection. Field optical efficiency is fundamentally dependent on the intercept factor, which decreases with the aiming factor. Shading and blocking factor is virtually constant for a given time; because of parallel projection assumption between neighbor heliostats. Expectedly, the effect of rows alternatively aiming up and down is not captured by the model.

Table 4.1: Heliostat field optical losses and concentrations for different aiming factors.

Solar time	Aiming factor	f_{int}	f_{sb}	η	C_{max}	C_{mean}
12	(equatorial)	0.847	0.999	0.648	1694	701
	3	0.846	0.999	0.648	1588	701
	2	0.835	0.999	0.639	1159	691
	1	0.735	0.999	0.561	906	607
	0	0.446	0.998	0.340	856	368
9	(equatorial)	0.842	0.984	0.603	1669	652
	3	0.841	0.984	0.602	1571	651
	2	0.827	0.984	0.591	1148	640
	1	0.723	0.984	0.517	895	560
	0	0.445	0.983	0.316	853	342
7	(equatorial)	0.832	0.938	0.514	1508	556
	3	0.829	0.938	0.513	1420	555
	2	0.809	0.938	0.501	1049	543
	1	0.705	0.938	0.437	812	473
	0	0.441	0.938	0.271	779	294

Regarding the concentration ratios of flux density, the peak is rapidly reduced when moving from $k = 3$ to $k = 2$; while for smaller aiming factors the change is slower. On the contrary, the mean concentration ratio on the receiver drops quickly near the smaller aiming factors; in parallel to the behavior of intercept factor and optical efficiency.

For the Gemasolar case study herein presented, it could be said that elevated flux is collected for aiming factors higher than (or around) 2. However, from the point of view of the receiver integrity, aiming factors lower than (or around) 2 are safe; known that, broadly speaking, flux densities higher than 1 MW/m^2 induce tube thermal stresses near its limit. Those requirements, together with corrosion limitations, are addressed in the aiming strategy presented in the following Chapter (Sánchez-González *et al.*, 2016).

4.6 Conclusions

This Chapter presented the extension of the validated model in Chapter 2 to a whole field of heliostats. The resulting tool computes the flux maps from any heliostat field by superposition of the maps from every single heliostat in the field. Computation of optical loss factors was implemented in the Matlab® code, taking into account parallel projection for the computation of mirror shading and blocking. Less than 1 minute of computation time is required in a standard desktop PC, for the selected field of 2650 heliostats.

Firstly, results for the single aiming strategy were presented. For any vertical flux profile on the receiver, it was found that the peak flux is located slightly above the midpoint. Even aiming at the equatorial line of a panel, adjacent panels are impinged somewhere above; which explains that subtle effect.

Finally, a 2-step symmetric aiming strategy was developed on the basis of parameter k. Aiming factors around 3, or higher, generated flux maps equivalent to single equatorial aiming with a hot strip in the middle, while $k = 0$ oppositely generated maps with two peaks on the receiver edges and intercept factors lower than 50%. For the Gemasolar case study and at any solar time, an aiming factor equal to 2 yielded the most uniform flux maps with a flat central region. Advantageously, $k = 2$ significantly reduced the maximum flux on the receiver in comparison with single aiming, while the total intercepted flux was kept.

Nomenclature

AM	Area of heliostat mirror [m^2]
BD_k	Beam diameter based on k [m]
BR_k	Beam radius based on k [m]
C	Concentration ratio of flux density [-]
D	Receiver diameter [m]
DNI	Direct normal irradiance [W/m^2]
F	Solar flux density [W/m^2]
f	Optical loss factor [-]
H	Receiver height [m]
k	Aiming factor [-]
N	Number [#]
SLR	Slant range [m]
T	Target point
$\mathbf{t}$	Target vector
THT	Tower optical height [m]

Greek symbols

ϵ	Elevation angle [rad]
ρ	Mirror reflectivity [-]
σ	Error, standard deviation [mrad]
ω	Incidence angle [rad]

Subscripts

b	Blocking
e	Effective
eq	Receiver equator
h	Heliostat
i, j	Node index
int	Interception
optloss	With optical losses
p	Panel in the receiver
pt	Target panel
ref	Reflected
s	Shading
sb	Shading and blocking
si	Image plane system of coordinates
slp	Mirror slope
st	Target system of coordinates
sun	Sunshape
trk	Tracking

References

Augsburger, G. & Favrat, D. 2013 Modelling of the receiver transient flux distribution due to cloud passages on a solar tower thermal power plant. *Solar Energy* 87, 42–52.

Ballestrín, J. & Marzo, A. 2012 Solar radiation attenuation in solar tower plants. *Solar Energy* 86 (1), 388–392.

Besarati, S. M., Yogi Goswami, D. & Stefanakos, E. K. 2014 Optimal heliostat aiming strategy for uniform distribution of heat flux on the receiver of a solar power tower plant. *Energy Conversion and Management* 84, 234–243.

Burgaleta, J. I., Arias, S. & Ramirez, D. 2011 Gemasolar, the first tower thermosolar commercial plant with molten salt storage. In *SolarPACES*.

Collado, F. J. 2008 Quick evaluation of the annual heliostat field efficiency. *Solar Energy* 82 (4), 379–384.

Collado, F. J. 2011 Design of solar power tower plants heliostat by heliostat: The shadowing and blocking factor. In *SolarPACES*. Granada, Spain.

Collado, F. J. & Guallar, J. 2009 Design of solar tower plants heliostat by heliostat: The blocking factor. In *SolarPACES*. Berlin, Germany.

Collado, F. J. & Guallar, J. 2012 Campo: Generation of regular heliostat fields. *Renewable Energy* 46, 49–59.

Falcone, P. K. 1986 A handbook for solar central receiver design. *Tech. Rep.*. Sandia National Laboratories, SAND-86-8009.

Huang, W., Li, L., Li, Y. & Han, Z. 2013 Development and evaluation of several models for precise and fast calculations of shading and blocking in heliostats field. *Solar Energy* 95, 255–264.

Kistler, B. 1986 A user's manual for DELSOL3: Computer code for calculating the optical performance and optimal system design for solar thermal central receiver plants. *Tech. Rep.*. Sandia National Laboratories, SAND-86-8018.

Lata, J. M., Alcalde, S., Fernández, D. & Lekube, X. 2010 First surrounding field of heliostats in the world for commercial solar power plants - Gemasolar. In *Proceedings of SolarPACES*.

Leary, P. L. & Hankins, J. D. 1979 User's guide for MIRVAL: a computer code for comparing designs of heliostat-receiver optics for central receiver solar power plants. *Tech. Rep.*. Sandia National Laboratories, SAND-77-8280.

Lipps, F. W. 1992 Computer Simulation of Shading and Blocking : Discussion of Accuracy and Recommendations. *Tech. Rep.* April 1992. NREL, National Renewable Energy Laboratory, Golden, Colorado.

Lipps, F. W. & Vant-Hull, L. L. 1978 A cellwise method for the optimization of large central receiver systems. *Solar Energy* 20 (6), 505–516.

Rodríguez-Sánchez, M., Sánchez-González, A., Marugán-Cruz, C. & Santana, D. 2014 Saving assessment using the PERS in solar power towers. *Energy Conversion and Management* 87, 810–819.

Rodríguez-Sánchez, M., Sanchez-Gonzalez, A. & Santana, D. 2015 Revised receiver efficiency of molten-salt power towers. *Renewable and Sustainable Energy Reviews* 52, 1331–1339.

Sánchez-González, A., Rodríguez-Sánchez, M. & Santana, D. 2016 Aiming strategy model based on allowable flux densities for molten salt central receivers. *Solar Energy* In press (http://dx.doi.org/10.1016/j.solener.2015.12.055).

Sánchez-González, A. & Santana, D. 2015 Solar flux distribution on central receivers: A projection method from analytic function. *Renewable Energy* 74, 576–587.

Vant-Hull, L. L. 2002 The Role of "Allowable Flux Density" in the Design and Operation of Molten-Salt Solar Central Receivers. *Journal of Solar Energy Engineering* 124 (2), 165.

CHAPTER

FIVE

Aiming strategy for molten salt receivers: allowable flux density approach

Contents

Summary

This Chapter presents an aiming model to properly point heliostats at cylindrical molten salt receivers in Solar Power Tower plants. By means of two iterative algorithms (search and fit), the proposed strategy attempts to maximize the receiver thermal power output while preserving the receiver operational limits. Corrosion and thermal stress constraints are translated into allowable flux densities (AFD) that are handled by the model. The computer code accommodates the flux images produced by each heliostat in a field to accurately fit the AFD limit. A Gemasolar-like field-receiver system serves to illustrate the aiming model. Compared to the equatorial aiming, receiver interception is slightly lower using the proposed strategy, but the receiver integrity is ensured; peak flux is significantly reduced up to 23%. It was found that a favorable flux density profile generally has its peak displaced to the salt entrance at each receiver panel. Since external cylindrical receivers consist of a combination of up-flow and down-flow panels, the optimal flux profile is challenging for contiguous panels with contrary demands. In spite of that, remarkable matching is achieved by the fit algorithm. Because of its fast computation and automatic operation, the resulting tool can be

applied to real-time control of existing heliostat fields and the integrated design of the coupled systems field and receiver.

5.1 Introduction

In Central Receiver Systems, also called Solar Power Tower plants, thousands of heliostats concentrate sunlight at the central receiver (Vant-Hull, 2012). The interaction between heliostat field and thermal receiver plays an important role in the design and operation of Central Receiver Systems (CRS). Since single aiming usually leads to exceed the receiver technical limits, the development of multi-aiming strategies is fundamental.

Several researchers have recently developed aiming strategy models based on metaheuristic techniques. Salomé *et al.* (2013) used a TABU algorithm to flatten the flux distribution on THEMIS flat plate receiver, while minimizing the spillage loss. Besarati *et al.* (2014) addressed the same problem but employing a genetic algorithm (GA). An ant colony optimization (ACO) metaheuristic was adapted by Belhomme *et al.* (2013) to maximize the electrical output of a concentrated photovoltaic receiver.

Other aiming approaches put the emphasis on meeting the operational limits of the receiver. García-Martín *et al.* (1999) developed a closed-loop control algorithm for TSA volumetric receiver. Air temperature was measured at different points in the receiver, and then the algorithm adjusted the position of five aim points and the heliostat tracking in order to comply with the temperature limits.

Vant-Hull (2002) introduced the concept of allowable flux density (AFD) dependent on heat transfer fluid (HTF) temperature and flow rate, which was quantified for the cylindrical molten salt receiver at Solar Two plant. When overflux conditions were detected by RCELL code (Lipps & Vant-Hull, 1978), the dynamic aim processing system (DAPS) was responsible for: a) identifying the heliostats producing the greatest flux peak at the hot spots, and b) removing them from tracking. Given an outlet set point temperature, the receiver control system consequently decreases the mass flow rate, which in turn lowers the AFD limit. Occasionally, numerous heliostats had to be removed from tracking, leading to instability (Pacheco, 2002).

In the present research, an alternative aiming approach was developed based on the allowable flux density limit. The proposed model selects the heliostats' aim points that provide a good enough solution that maximizes the thermal power output from a cylindrical molten salt receiver. To meet the goal, a recursive algorithm was implemented. A general overview of the proposed aiming strategy model is firstly given in the following section.

5.2 General description

The objective of the proposed aiming strategy model is to point the heliostats in a way that looks for collecting as much as possible solar flux on the receiver, while maintaining its structural integrity. In external cylindrical receivers, aim points are vertically shifted. Heliostat flux images superpose so that the whole flux map keeps within the allowable flux density limits. The inputs required by the aiming model are provided by an optical model and a database of allowable flux densities. These inputs are depicted in the general flowchart in Figure 5.1, along with the initial input data: heliostat field configuration, receiver geometry, material properties and boundary conditions (i.e. solar time, DNI, and ambient temperature).

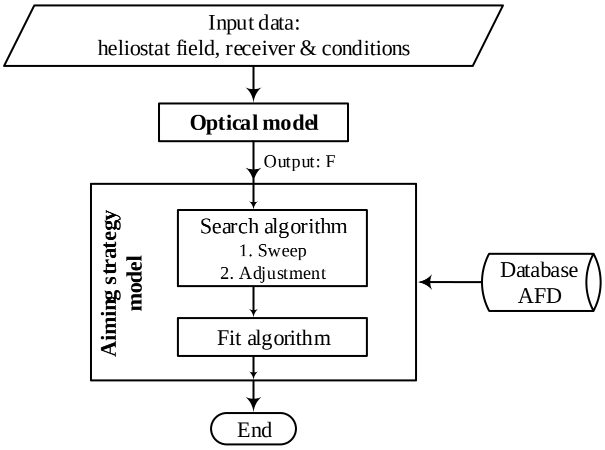

Figure 5.1: General flowchart of the whole model.

The optical model previously validated by the author in Chapter 2 (Sánchez-González & Santana, 2015) will be herein utilized. This model computes the flux density distribution caused by a whole field of heliostats, taking into account optical losses: shading, blocking, cosine, attenuation, reflectivity, and spillage (Chapter 4). The basis of the model is on the oblique projection, from image plane into receiver surfaces, of the flux distribution predicted by an analytic function; in this instance UNIZAR function by Collado *et al.* (1986). The effective error σ_e derives from the convolution of three circular Gaussian distributions: sunshape σ_{sun}, mirror slope error σ_{slp} and heliostat tracking error σ_{trk}; according to Equation (2.10).

The concept of aiming factor introduced in previous Chapter 4 is again utilized. In terms of the k aiming factor, the radius of the reflected beam on the receiver, BR_k, is estimated according to Equation (4.8). The use of beam radius dependent on k aiming factor, BR_k, is crucial in order to control the spillage losses in the strategy proposed in the present Chapter. Details will be described in algorithms Section 5.4.

On the other hand, the receiver must comply with some limitations in order to operate reliably and safely. The two main constraints are corrosion of metal tubes, and excessive thermal stress. Tube corrosion in the presence of high temperature molten salt can be prevented by limiting the maximum film temperature. Likewise, receiver failure can be avoided by reducing the thermal gradient on the tube.

Since the output parameter controlled by an aiming strategy is the flux distribution on the receiver, rather than film temperature or thermal gradient in the tubes, both restrictions (i.e. corrosion and thermal stress) are translated into a maximum allowable flux density, AFD, incident on the receiver. This approach, previously reported by Vant-Hull (2002) has been adopted in the model. For the corrosion constraint, such AFD depends on the HTF mass flow rate and temperature, which in turn depend on the receiver geometry: diameter D, height H, number of panels N_p, and tube diameter d. A detailed description of the methodology to generate a database of AFD is presented in Section 5.3.

The proposed aiming model consists of two sequential algorithms, see Figure 5.1. The objective of the first one, named search algorithm, is to find the maximum aiming factor with which the AFD limit could be accomplished using a symmetric aiming strategy with respect to the equator. Then, the fit algorithm is responsible for selecting the aim points so that the flux profiles match the AFD limit which is usually non-symmetric. In Section 5.4 both algorithms are described.

In addition to the optical model of the heliostat field, a thermal model of the receiver is required to predict the heat exchange processes taking place in the central receiver. Such a receiver model is essential not only to generate the database of AFD, but also to calculate the mass flow and temperature of the HTF at different stages during the aiming strategy calculation procedure.

The receiver model, previously reported in Rodríguez-Sánchez *et al.* (2014*b*,*a*), is herein utilized. This model considers temperature variations in both axial and circumferential directions; i.e. 2D discretization of the tubes. The heat flux absorbed by each cell is calculated by means of the Net Radiation Method by Modest (2003), taking into account the view factors computed with the crossed-string method. The external convective heat coefficient is obtained from Siebers & Kraabel (1984). For any receiver design, the core of the model computes the heat fluxes and temperatures at each cell node, given an incident solar flux density distribution and a HTF mass flow rate. Setting the HTF temperatures at inlet and outlet, the model also recomputes the mass flow rate at each iteration, as shown in the receiver flowchart in Figure 5.2 and according to the following Equation:

$$\dot{m}_{s,new} = \frac{Q_{rec}}{Cp_s\left(T_{s,out} - T_{s,in}\right)} \tag{5.1}$$

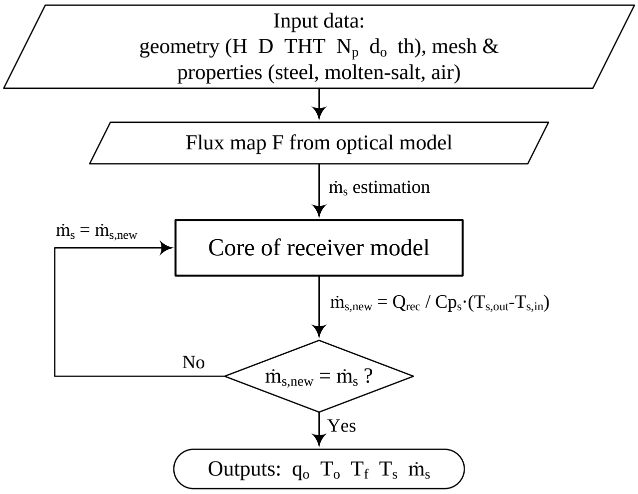

Figure 5.2: Flowchart of the receiver model.

Prior to explaining the AFD database generation and the main algorithms in Section 5.3 and Section 5.4 respectively, the case study used throughout this Chapter to illustrate the model is presented in the following subsection. Results for different solar times are exposed and discussed at the end of the Chapter.

5.2.1 Case study

Gemasolar solar tower power plant, Figure 5.3, is again utilized to illustrate the model proposed in the present Chapter. The description and parameter values previously stated in Section 4.2 are herein used, unless otherwise specified. For instance, mirror reflectivity and cleanliness adopt conservative values of 0.88 (Collado & Guallar, 2013) and 0.95 (Sargent & Lundy, 2003), respectively; therefore, effective reflectivity, ρ, equals 83.6%.

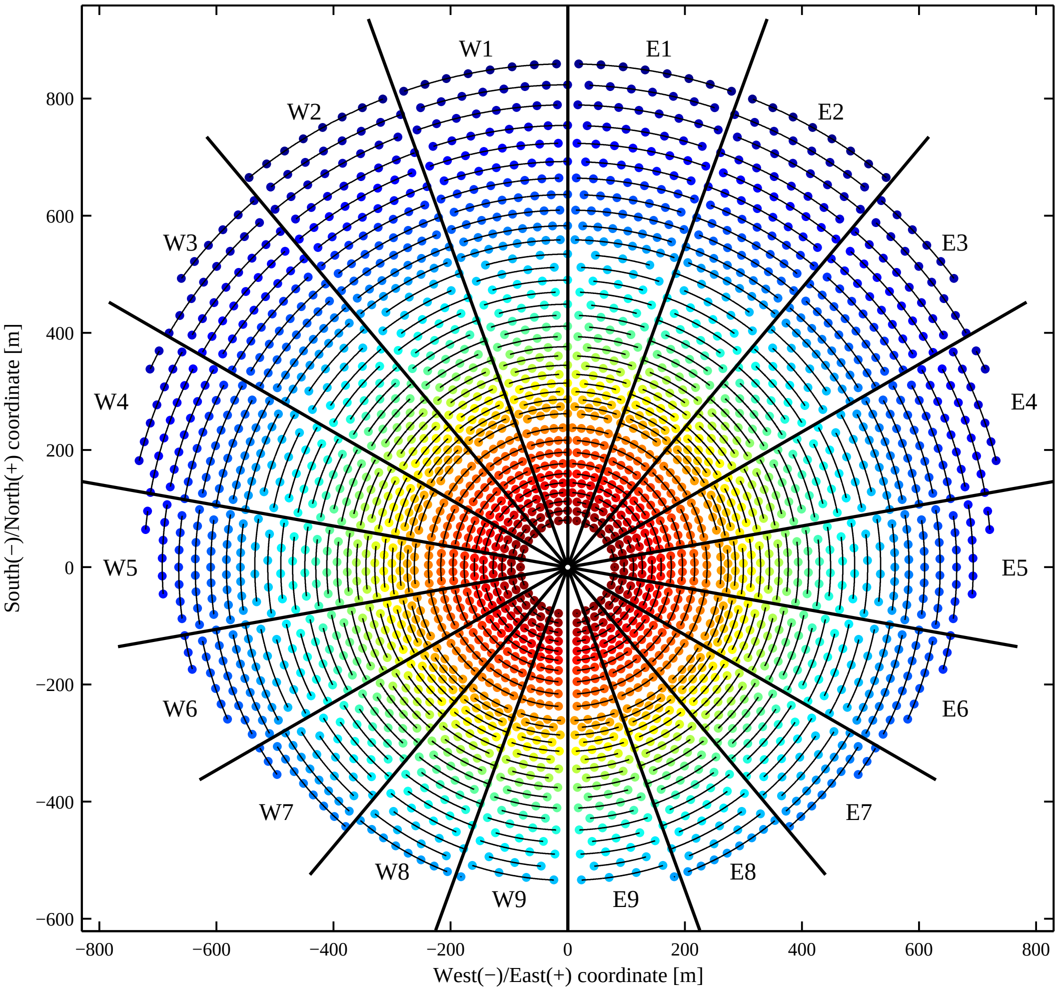

Figure 5.3: Layout of Gemasolar heliostat field. Heliostats are colored by distance to the tower. Sectors are labeled corresponding to receiver panels and row-sector arc-lines are plotted.

The receiver comprises 18 panels (N_p) arranged around a cylindrical shell of diameter 8.5 m (D) and 10.5 m high (H), as depicted in Figure 5.4. Outer diameter of tubes (d_o) is assumed to be 45 mm and its wall thickness (th), 1.5 mm; optimal tube parameters according to Rodríguez-Sánchez *et al.* (2014*b*). Given 2 mm separation between tubes, each panel comprises 31 tubes within its 1.5 m width. Receiver tubes, which are made of Incoloy 800H, are coated with black Pyromark paint. Obviously, the computer code can handle input parameters other than those indicated for this case study.

The heliostat field is divided into 18 sectors corresponding to each of the panels where the heliostats aim to. Figure 5.3 depicts the Gemasolar field layout displaying the sectors. As will be discussed later, these sectors are used in the aiming strategy.

The HTF is molten nitrate salt, whose properties were reported in Zavoico (2001). Under normal operation, salt inlet and outlet temperatures at the receiver are 290 and 565 °C, respectively. The receiver

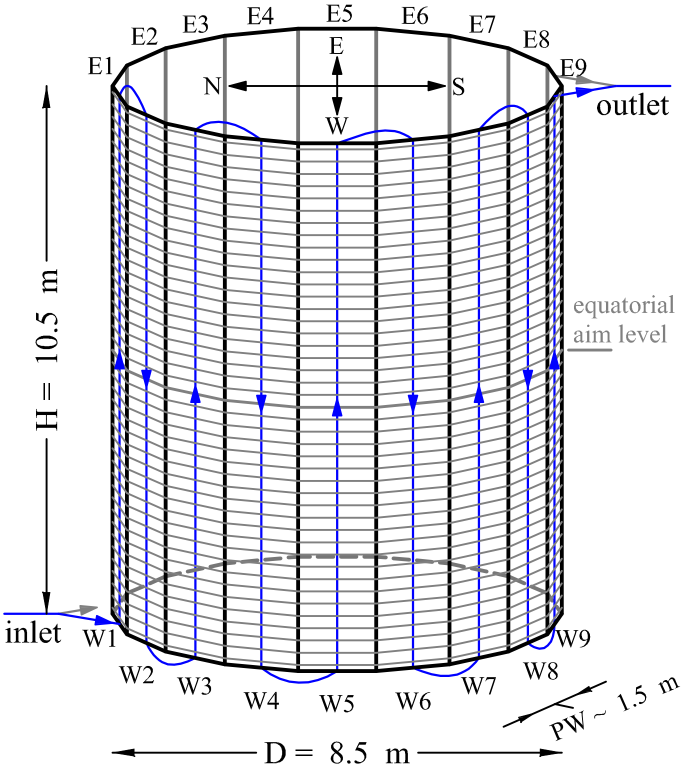

Figure 5.4: Receiver geometry. East and west panels are numbered from inlet (north) to outlet (south); and west flow path is depicted. Gray horizontal lines designate the aim levels.

inlet is at the north, where the flow is divided in two flow paths following a serpentine (up and down) flow pattern. Figure 5.4 shows the west flow path in the receiver, where each panel is named according to both the flow path (east and west) and the panel number from inlet to outlet. No crossover was considered as recommended in Rodríguez-Sánchez *et al.* (2015).

5.3 Allowable flux density

Corrosion and thermal stress are the most critical issues in the operation of molten salt receivers. Both restrictions can be translated into maximum allowable flux densities (AFD) incident on the receiver, which is a parameter directly controllable by the aiming strategy. The ultimate allowable flux density is the minimum between corrosion (AFD_{corr}) and thermal stress (AFD_{strs}). In this section, a methodology to determine the allowable flux density in any receiver tube section is presented. Such methodology is illustrated for the case study plant at noon time of summer solstice ($DNI = 930$ W/m^2, $T_{amb} = 35$ °C).

5.3.1 Corrosion limit

Molten nitrate salts become corrosive at high temperature. The film temperature, defined as that at the inner surface of the tube, is the limiting factor. For Incoloy 800H the maximum film temperature $T_{f,lim}$ is 630 °C, according to Bradshaw (1987).

The corrosion temperature limit can be translated into a maximum flux density incident on the tube, i.e. an allowable flux density due to corrosion (AFD_{corr}). The receiver thermal model (Rodríguez-Sánchez *et al.*, 2014*b*) is used to generate a database of AFD_{corr} depending on molten salt bulk temperature T_s and mass flow rate in the tube $\dot{m}_{s,t}$. The sequence of HTF mass flow rates hereafter used ranges from 0.6 to 5 kg/s in increments of 0.4 kg/s. By means of an iterative procedure, the flux density provoking a film temperature equal to the limit is found at each slice of a tube with a priori undefined length. The inlet and outlet temperatures of that virtual tube are 290 and 565 °C, respectively. The database generation procedure is indicated in Figure 5.5.

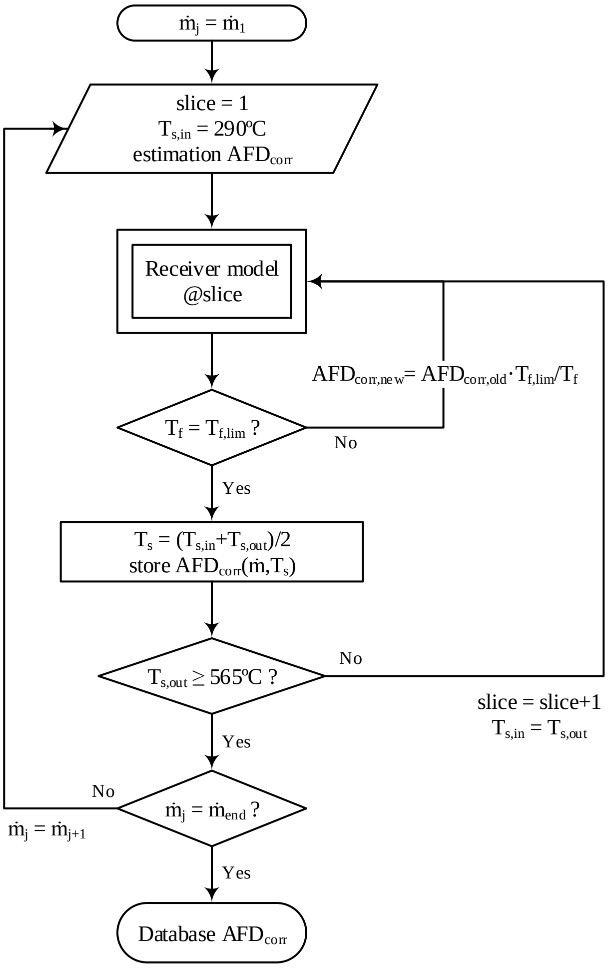

Figure 5.5: Algorithm to generate the database of allowable flux densities due to corrosion.

Figure 5.6 illustrates the resulting AFD_{corr} curves for Incoloy 800H. Clearly, the higher the mass flow rate, the higher the AFD_{corr} at a given salt temperature. The AFD_{corr} decreases when the molten salt bulk temperature increases; such decrement is more pronounced at higher mass flow rates.

Once the database of AFD_{corr} is generated, it can be applied to any flux density distribution on the receiver in order to verify compliance with the corrosion limit. To determine the AFD_{corr} limit under a given flux map, the receiver model is run to find out both the molten salt mass flow rate and its temperature evolution along the receiver flow path. For the case study at summer solstice noon with single aiming, the

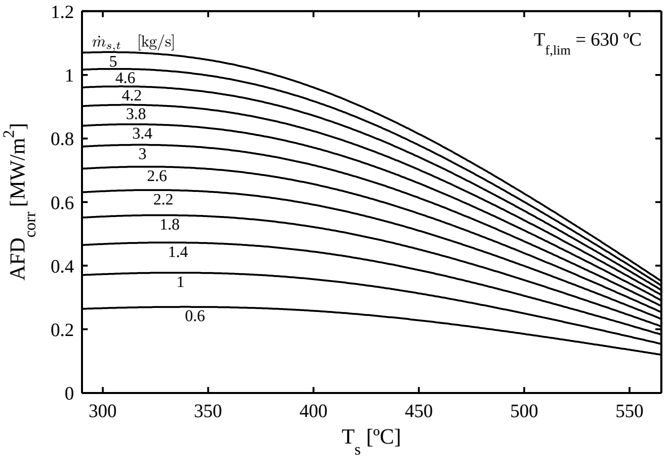

Figure 5.6: Allowable flux density due to corrosion as a function of salt temperature and mass flow rate, given a maximum film temperature of 630 °C for alloy 800H. Valid for outer tube diameter 45 mm and wall thickness 1.5 mm.

mean flux density F profiles at each panel are shown in Figure 5.7 (top), as well as the HTF temperature profile throughout the west flow path (bottom); east flow path is essentially symmetrical at noon. From the temperature profile and the mass flow rate, the AFD_{corr} red line is dictated. As can be checked in Figure 5.7, film temperature at the intersections between F and AFD_{corr} is equal to 630 °C, which serves as verification of the calculation procedure for the AFD_{corr} database.

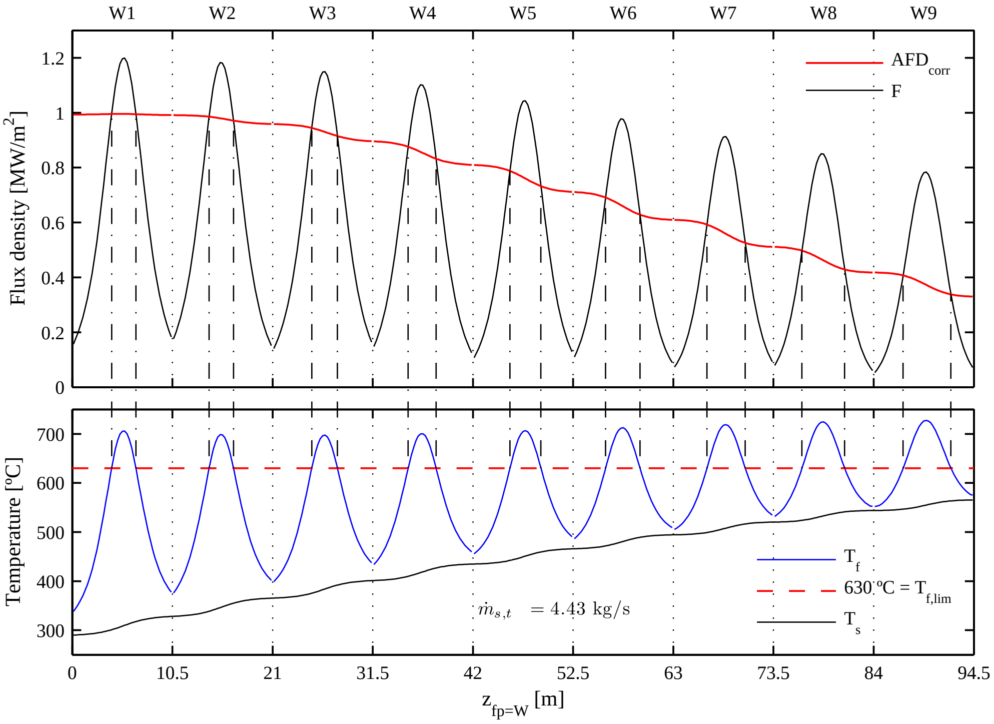

Figure 5.7: Flux density (top) and salt and film temperature (bottom) throughout west flow path with equatorial aiming at summer solstice noon. Red lines designate allowable flux density due to corrosion and maximum film temperature.

5.3.2 Thermal stress limit

The main source of thermal stress in receiver tubes is the radial temperature gradient, because it is high in comparison with axial and circumferential temperature gradients, as Irfan & Chapman (2009) pointed out. Under a thermal gradient in the radial tube direction ΔT_r, longitudinal and tangential stresses S in the outer surface satisfy Equation (5.2) (Young & Budynas, 2002). On the other hand, the conductive heat flux density at the outer tube surface q_o caused by a temperature difference in its thickness ΔT_r satisfies Equation (5.3).

$$S_o = \frac{\Delta T_r \gamma E}{2\,(1-\nu)\ln\left(d_o/d_i\right)}\left(1-\frac{2d_i^2}{d_o^2-d_i^2}\ln\frac{d_o}{d_i}\right) \tag{5.2}$$

$$q_o = \frac{2\cdot TC\cdot \Delta T_r}{d_o\cdot \ln\left(d_o/d_i\right)} \tag{5.3}$$

Combining Equations (5.2)-(5.3) (by elimination of ΔT_r) and using the ultimate tensile strength UTS of the tube material for S_o, the maximum allowable heat flux density to the tube, $q_{o.lim}$, can be formulated as follows:

$$q_{o,lim} = \frac{4\cdot TC\cdot UTS\,(1-\nu)}{\gamma\cdot E\cdot d_o\left(1-\frac{2d_i^2}{d_o^2-d_i^2}\ln\frac{d_o}{d_i}\right)} \tag{5.4}$$

According to subsection NH of ASME Boiler and Pressure Vessel Code (ASME, 2004), long-time elevated temperature service reduces the tensile strength TS by a factor of one-third. For alloy 800H, Figure 5.8 plots TS and the resulting UTS depending on the tube wall temperature, along with the rest of mechanical properties, taken from ASME Code. Substituting these values into Equation (5.4), the maximum heat flux density to the tube $q_{o.lim}$ is determined as a function of the outer surface temperature; which is represented by the dashed line in Figure 5.9.

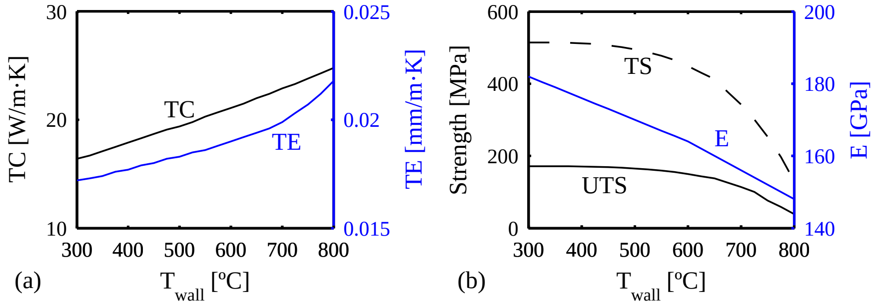

Figure 5.8: Mechanical properties of alloy 800H as a function of wall temperature: (a) thermal conductivity and thermal expansion; and (b) tensile strength, ultimate tensile strength and Young's modulus.

Because the maximum tube temperature takes place at the crown, radiation losses are to the surroundings, and the calculation is straightforward by means of Stefan-Boltzmann law. Convection losses are again estimated in accordance with Siebers & Kraabel (1984). The flux density limit, $F_{lim,strs}$, incident on the receiver results from adding radiation and convection losses to the maximum heat flux to the tube $q_{o,lim}$. The solid line in Figure 5.9 represents such flux density limit.

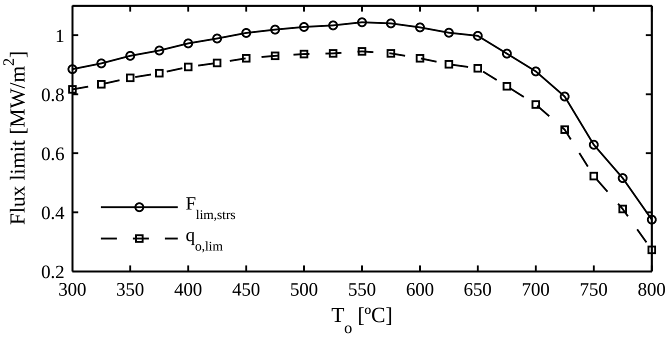

Figure 5.9: Maximum flux density incident on ($F_{lim,strs}$) and absorbed by ($q_{o,lim}$) the tubes due to thermal stress, depending on the outer temperature of the tube.

Allowable flux densities due to thermal stress, AFD_{strs}. are found in the intersection between the profile of incident flux density F and the above described $F_{lim,strs}$. For the case study at summer noon, both profiles are shown in Figure 5.10 (top) when equatorial aiming is set. The blue $F_{lim,strs}$ curve derives from the crown temperature T_o profile shown below, which is an output of the receiver model. Several flux maps (i.e. aiming strategies) should be needed in order to determine enough points of the AFD_{strs}, however it was proved that intersection points for different F profiles have almost constant vertical coordinate in each panel; i.e. the AFD_{strs} is almost uniform. Therefore, the AFD_{strs} is set constant and equal to that found in the intersection between $F_{lim,strs}$ and F with single aiming. The horizontal magenta segments in Figure 5.10 indicate the AFD_{strs} at each panel.

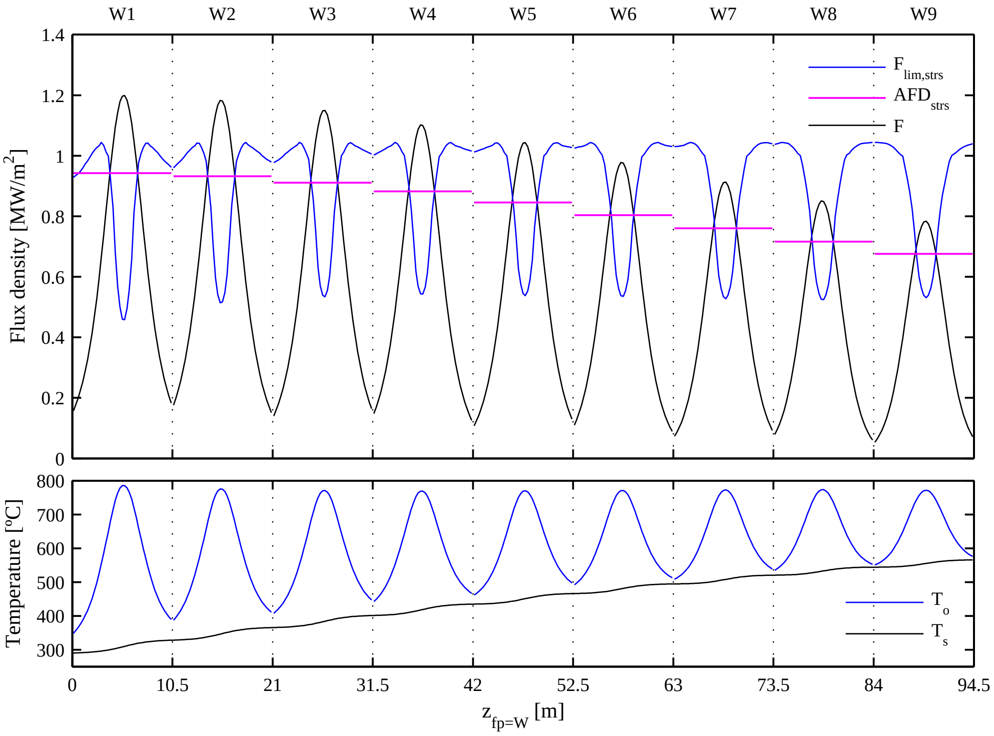

Figure 5.10: Flux density (top) and salt and outer wall temperature (bottom) throughout west flow path with equatorial aiming at summer solstice noon. Horizontal magenta lines designate the allowable flux density due to thermal stress at each panel, obtained through the intersection between actual flux density and stress limit.

5.4 Algorithms

The objective of the aiming strategy model is to automatically aim heliostats in a way that attempts to collect as much as possible solar flux on the receiver. This is equivalent to reduce spillage losses, which in turn protects the oven covers from overheating. At the same time, the flux distribution must not exceed the allowable flux density limits due to corrosion and thermal stress, presented in the previous section.

An odd number of horizontal target lines is established, since heliostats can be vertically aimed at discrete points in cylindrical receivers. For instance, these aim levels can coincide with the receiver mesh, as herein used. Given a nodal spacing of about 25 cm, it results in the 43 vertical aim levels depicted in Figure 5.4. Treated as a classical combinatorial problem, the total amount of possible aiming combinations equals 43^{2650}, for the heliostat field in the case study consisting in 2650 heliostats.

In the present study, the heliostats in each row-sector are aimed at the same height level. Such row-sectors are plotted with arc-lines in layout Figure 5.3, where each field sector is labeled in correspondence with its target panel. From 602 row-sectors, 43^{602} aiming combinations are still feasible. Evaluating each possible combination (i.e. exhaustive search) is intractable in terms of computation time. A fast algorithm to reach the main goal is also another objective. These purposes are accomplished by means of the two algorithms, search and fit, described in this section.

5.4.1 Search algorithm

The purpose of the search algorithm is to find the higher aiming factor for each field sector, k^{sector}, with which the AFD limit could be met. Aiming factors are calculated on the basis of the symmetric aiming strategy presented in previous Chapter 4.

The azimuth angle of the aim point is kept equal to that of the heliostat, therefore only vertical shift is considered in the proposed strategy. For cylindrical receivers, that centered azimuth angle diminishes spillage losses, which otherwise would increase.

The search algorithm is divided into two sequential parts named: sweep and adjustment routines, described in the following.

Sweep routine

As the name suggests, this algorithm performs a sweep of aiming factors starting from a high k value (i.e. low spillage). The purpose is to find for each field sector the first (highest) aiming factor that does not exceed the allowable flux density limit. The AFD profile limit throughout each flow path is kept fixed, even though this profile changes with the aiming. This way a preliminary k factor is quickly found for each field sector.

The sequence of k aiming factors swept in this algorithm is defined on the basis of the aim levels. A high number of k factors would result in heliostats aiming at the same height level, along with a large computation time. On the contrary, a small number of k factors would result in low accuracy. It was proved that a number of aiming factors equal to half the aim levels provides a favorable sweep resolution when the k values are logarithmically spaced; note that the cumulative energy within half of a beam as a function of its radius follows a rather logarithmic distribution. Starting from k=3, which is almost equivalent to equatorial aiming, and until k=0.2 (heliostats aiming at the receiver edge would mean k=0), the sequence of 22 aiming factors used in the case study is: k_j = [3 2.64 2.32 2.04 1.79 1.57 1.38 1.22 1.07 0.94 0.83 0.73 0.64 0.56 0.49 0.43 0.38 0.34 0.29 0.26 0.23 0.2].

Figure 5.11 depicts the detailed flowchart of the sweep routine. The receiver model is run only once in order to establish the AFD profile limit, which corresponds to the higher aiming factor (i.e. k=3). Using the symmetrical aiming strategy the whole flux map is assembled for each aiming factor following the sequence stated above. If the flux profile is under the AFD limit for any receiver panel, such k factor is stored for the corresponding field sector. This acceptance criterion is formulated as $F_{k,p} < AFD_p$. The calculation procedure stops when k values are assigned to every field sector, avoiding the computation of unnecessary cases.

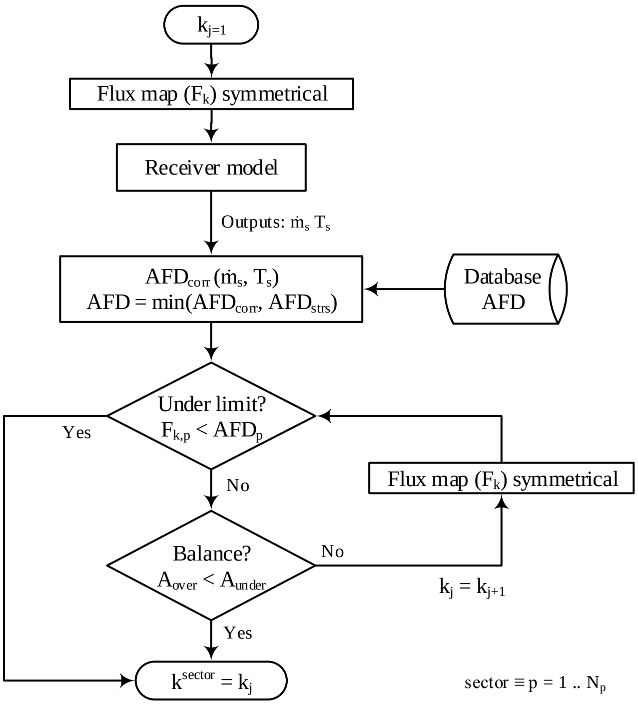

Figure 5.11: Flowchart of the sweep routine.

Because a symmetric aiming strategy with respect to the equator is used at this stage, it is known that two shoulders emerge in the flux density profile when the aiming factor is low enough. In some cases, aim points could be redistributed to balance the energy flux surpassing the AFD limit. Finding the outermost intersection point between F and AFD, and defining a vertical range between that point and its symmetrical about the middle point in the panel, the difference between F and AFD profiles is computed within that range. From the graphical interpretation shown in detail 2 within Figure 5.12, if the area of the region over the AFD limit, A_{over}, is smaller than the area of the region under, A_{under}, the balance is presumed. Hence, the alternative acceptance criterion is defined as $A_{over} < A_{under}$, as stated in flow chart Figure 5.11.

For the case study at summer noon, Figure 5.12 represents the profiles of flux density along the sweep calculation throughout the west flow path. For the 22 aiming factors defined above, the corresponding F profiles are depicted in the Figure. The allowable flux density is represented for both the corrosion and the thermal stress limits, although the actual AFD limit (plotted as solid line) is the lower of the two. In subsequent Figures, only the actual AFD will be displayed.

The selected F profile at each panel is indicated by blue thick line and its corresponding sector aiming factor k^{sector} is displayed at the bottom. The under limit criterion is met in the first five panels, whereas for panels 6 to 9 the balance is achieved. A caption of the flux density profiles in the last panel is shown in Detail 1 (Figure 5.12). F profiles corresponding to the last nine aiming factors are also represented, even though their computation is unnecessary.

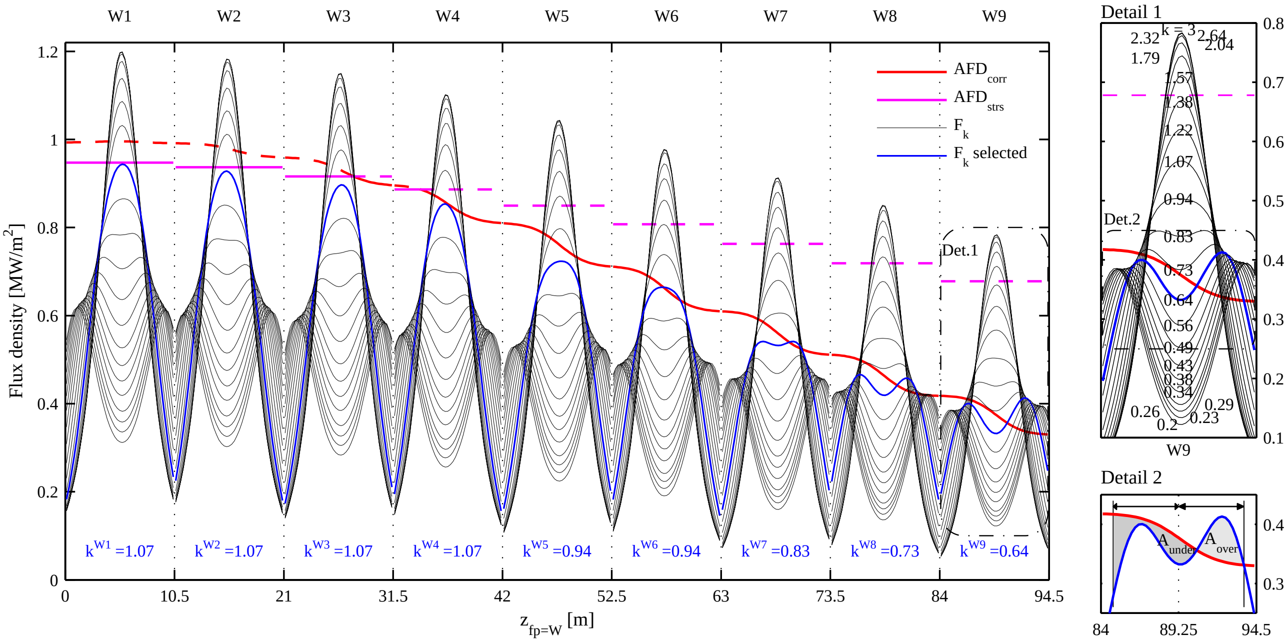

Figure 5.12: Profiles of flux density, throughout west flow path at summer solstice noon, generated for different aiming factors (sweep). Selected profile at each panel and its corresponding aiming factor are colored in blue. On the right, detail 1 enlarges the sweep on the last panel and detail 2 stands for the balance between flux over and under the limit. Allowable flux densities due to corrosion and thermal stress are colored in red and magenta, respectively; the most restrictive limit is plotted as solid line.

Adjustment routine

In general, a modification of the aim points changes the molten salt mass flow rate and its temperature evolution through the flow path, because of the outlet set point temperature (565 °C). Consequently, the AFD_{corr} limit is modified. In the preceding sweep routine the AFD corresponded to that for the higher aiming factor (k=3). The adjustment routine precisely adjusts the preliminary aiming factors from the sweep routine taking into account the real AFD limit.

The adjustment routine (Figure 5.13) checks the same acceptance criteria than the sweep routine, but updating the AFD using the receiver model and the AFD database. Besides, the aiming factor is only increased in those sectors in which neither the under limit criterion nor the balance are met.

Figure 5.14(a)(top) shows the actual AFD limit along with the F profile for the aiming factors obtained from the sweep routine. However the acceptance criteria is not met in the last two panels, since the AFD

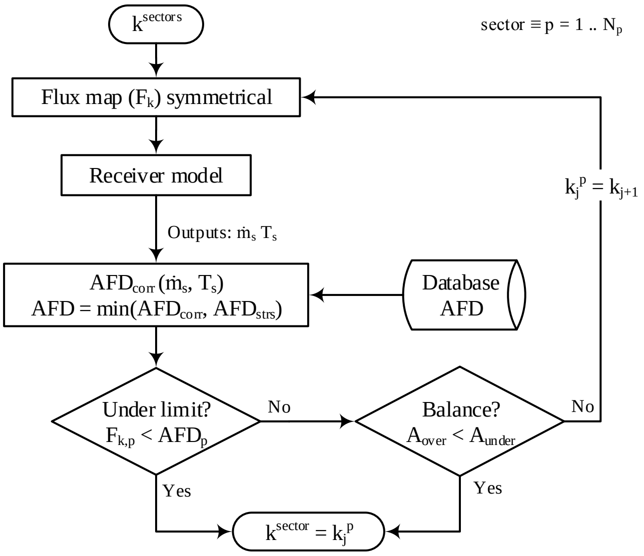

Figure 5.13: Flowchart of the adjustment routine.

has been lowered; $\dot{m}_{s,t}$ has changed from 4.43 to 4.27 kg/s.

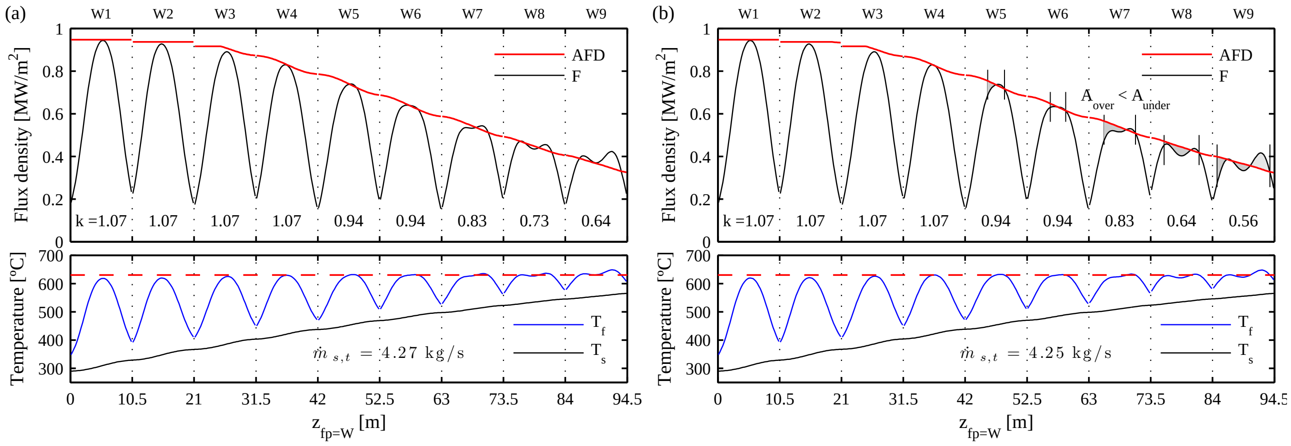

Figure 5.14: Flux density (top) and salt and film temperature (bottom) throughout west flow path at summer solstice noon for: (a) aiming factors resulting from the sweep routine, and (b) aiming factors after performing the adjustment routine.

Once the adjustment routine has been applied, the aiming factor in the last two sectors decreases until the *AFD* limit, recomputed in each iteration, is achieved (Figure 5.14). As a consequence, interception slightly decreases, likewise mass flow rate. Now the under limit criterion is met in panels 1 to 4 and the balance is achieved in the last 5 panels.

5.4.2 Fit algorithm

In the previous search algorithm a symmetrical aiming strategy was utilized to quickly find preliminary aiming factors at each field sector $k^{sectors}$. The flux density vertical profile in each panel is consequently symmetric respect to the equator, as opposed to the AFD profile which decreases along the flow path.

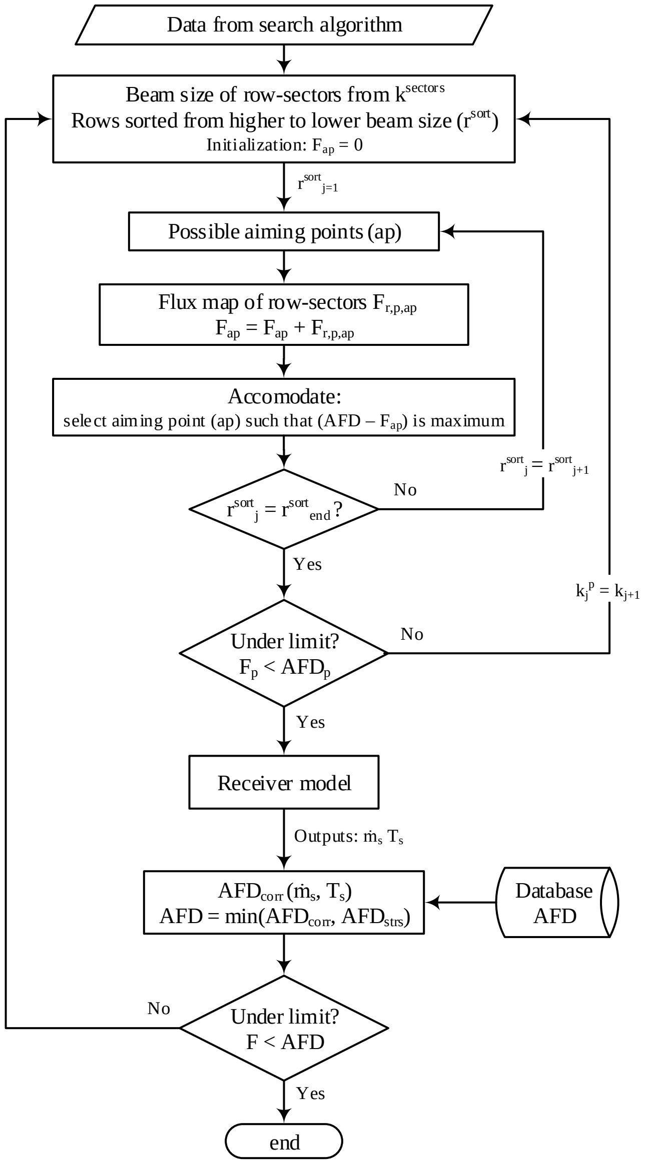

Figure 5.15: Flowchart of the fit algorithm.

The purpose of the fit algorithm (Figure 5.15) is to select the heliostat target points such that the flux F profile properly fits the AFD limit. The range of aim levels that can be targeted for each row-sector is established from the $k^{sectors}$ obtained in the search algorithm. Among the possible aiming points, the fit algorithm selects that one which maximizes the difference between F and AFD. In other words, the fit algorithm deals with accommodating the flux profiles for each row-sector in such a way that the subtraction $AFD - F$ is the maximum possible.

The order in the superposition of the flux maps produced by each heliostat is a key factor to the success of the algorithm. Since the flux reflected by a heliostat impacts into not only the panel corresponding to its field sector, but also the nearby panels, the possible images by a whole row of heliostats must be added together, although the accommodation is performed row-sector by row-sector. It is favorable to sort the rows depending on the number of feasible aim levels, seen as degrees of freedom. Accordingly, rows are sorted from higher to lower beam radius (r^{sort}).

Figure 5.15 represents the detailed flowchart of the fit algorithm, where the acceptance criterion is restricted to not surpassing the AFD limit. In case of rejection, the aiming factor is lowered to the next in the k_j list. At the end, the receiver model is run and the AFD updated to check whether this limit remains not disrupted.

For the case study presented in this study, Figure 5.16 represents the profile of flux density in the west flow path resulting from the fit algorithm. The cumulative F profiles after each row addition are colored according to the code in heliostat field Figure 5.3 on page 77. The last curve corresponds to the final flux density profile that never surpasses the AFD boundary. The F profile tends to match the AFD limit in the central region of the panel.

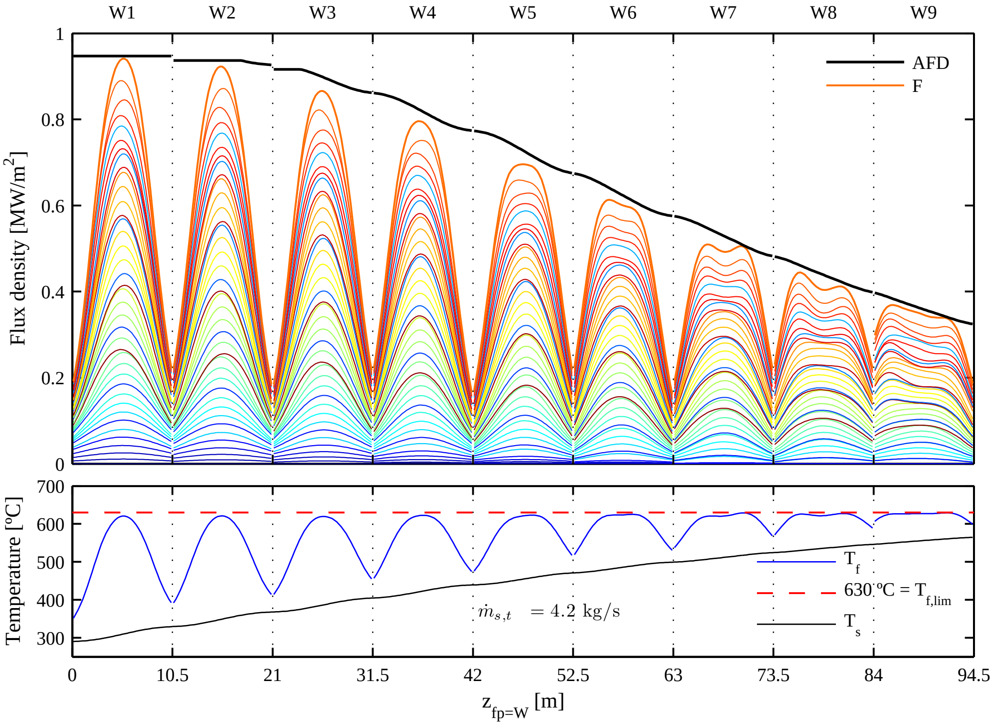

Figure 5.16: Profiles of flux density (top) and salt and film temperature (bottom) throughout west flow path at summer solstice noon. Each heliostat row image is added during the fitting process in the order denoted by the color that corresponds to those in Figure 5.3

A single node on an Intel® Core™ i5-2400 microprocessor (3.1 GHz) with 4 GB memory was used to perform the simulation. For the case study, the fit algorithm required on average 54.4 s of CPU time, and the search algorithm (sweep plus adjustment), 72.3 s.

5.5 Results and discussion

In this Section, the outputs from the proposed aiming strategy model are presented and discussed. Using the Gemasolar-like case study presented in Subsection 5.2.1, the results at different solar times of the summer

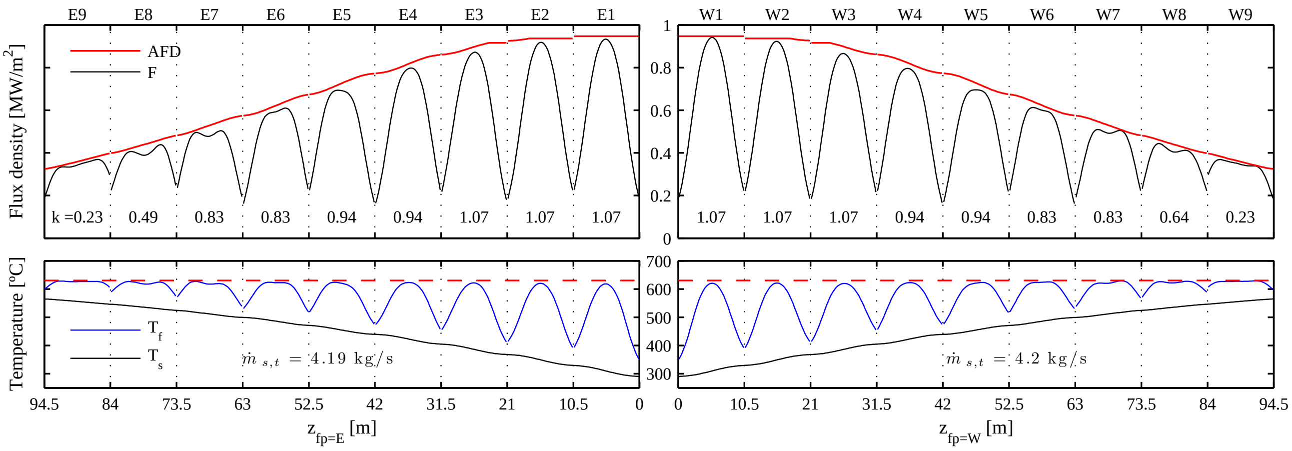

Figure 5.17: Flux density (top) and salt and film temperature (bottom) throughout east (left) and west (right) flow path at summer solstice noon (DNI = 930 W/m^2).

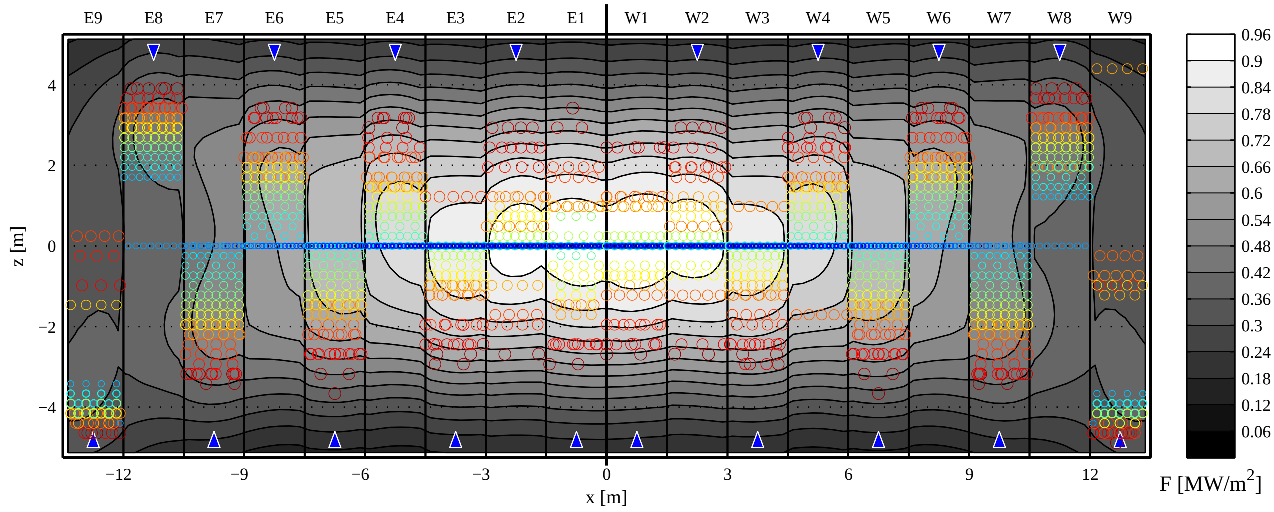

Figure 5.18: Flux density distribution at summer solstice noon (DNI = 930 W/m^2). Circles represent the aim point of each heliostat colored by its distance to the receiver, according to Figure 5.3. Triangles point out the direction of the flow at each receiver panel.

solstice are examined. Along with the profiles of flux density and temperatures throughout the two flow paths, the heliostat aim points and the resulting flux maps are reported.

For the noon time case used to illustrate the algorithms in the preceding section, the profiles of flux density and temperature (bulk and film) are represented in Figure 5.17 for east (left) and west (right) flow path. As expected, results for both flow paths are noticeably symmetrical; negligible difference exists between both mass flow rates.

The aiming point of each heliostat in the field is marked in Figure 5.18, where the 3D surface of the receiver is unfolded. The heliostat corresponding to each aim point can be identified with the aid of Figure 5.3 on page 77, attending to the color of the row and the heliostat sector or azimuth. At the same time, the distribution of flux densities on the receiver is plotted in the background. This grayscale flux map complements the mean F profiles shown in previous Figure 5.17.

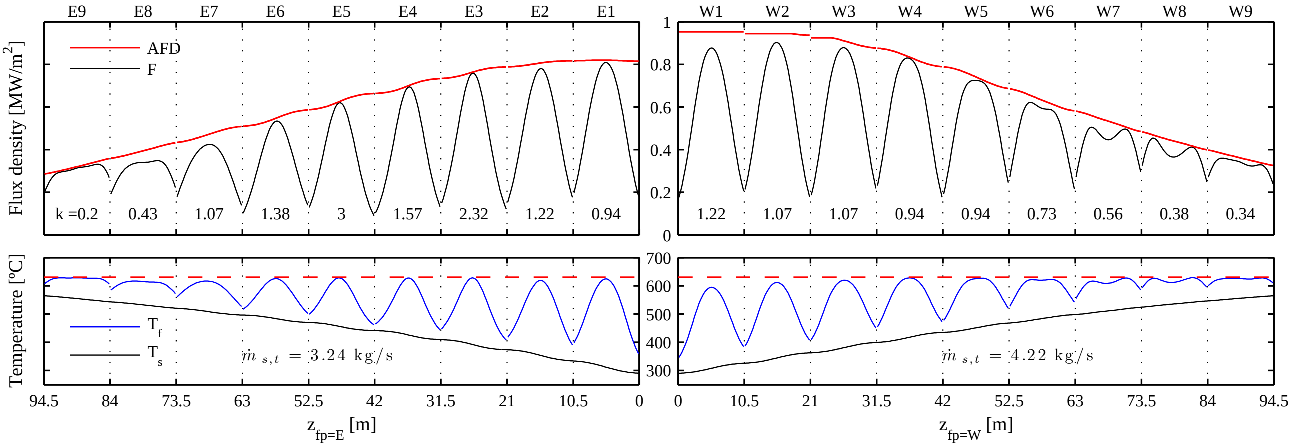

Figure 5.19: Flux density (top) and salt and film temperature (bottom) throughout east (left) and west (right) flow path at 9:00 solar time at summer solstice ($DNI = 910$ W/m^2).

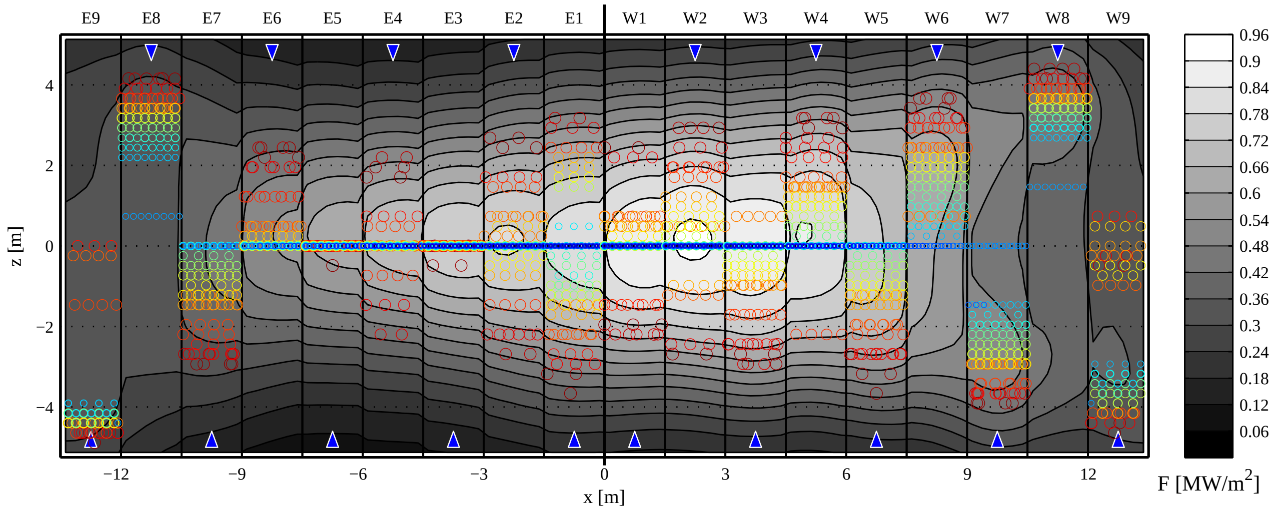

Figure 5.20: Flux density distribution at 9:00 solar time at summer solstice ($DNI = 910$ W/m^2). Circles represent the aim point of each heliostat colored by its distance to the receiver, according to Figure 5.3. Triangles point out the direction of the flow at each receiver panel.

Paying attention to the aim points, these are located in the equatorial belt or evenly spread around it for the first two panels in both circuits. In the rest of the panels, target points tend to distribute unequally. Heliostats far from the receiver aim to the equator, whereas aim points in near heliostats are shifted to the panel entrance; top for downstream and bottom for upstream panels. Roughly speaking, the closer the heliostat is to the receiver, the farther the aim point from the middle is.

At solar times other than noon, outputs are different for east and west flow path. Before noon higher radiation is received from the west side of the heliostat field, and vice versa. At 9:00, receiver west flow path captures 30% more thermal energy than east side, as can be inferred from the mass flow rates displayed on Figure 5.19. Just because of higher $\dot{m}$ in the west circuit, its AFD_{corr} limit is also higher compared to the east for the same z_{fp} distance.

Flux profiles perfectly fit the AFD limit in the central region of each panel, except for panels 7 and 8 in west side where valleys are formed. It must be pointed out that adjacent panels demand opposed flux

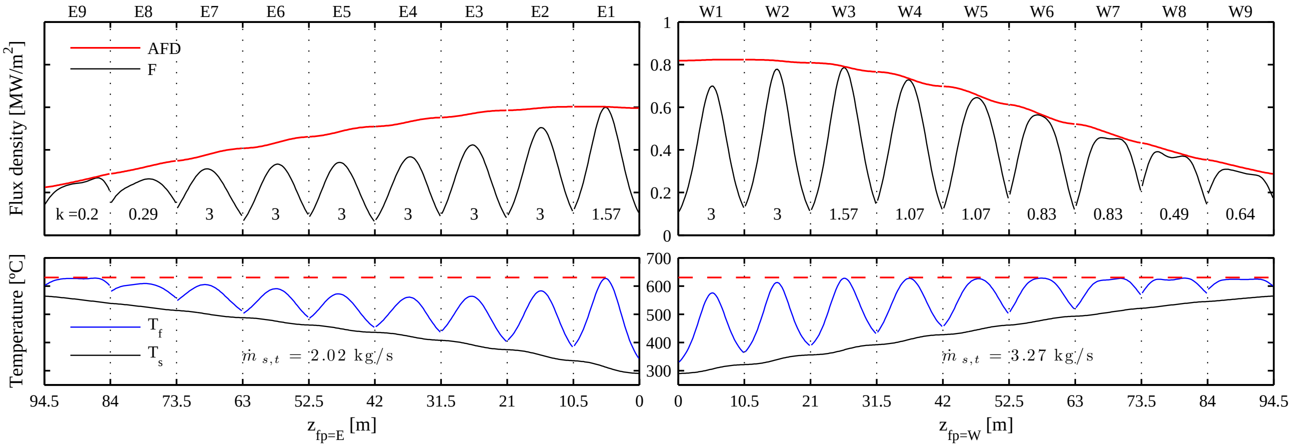

Figure 5.21: Flux density (top) and salt and film temperature (bottom) throughout east (left) and west (right) flow path at 7:00 solar time at summer solstice (DNI = 770 W/m^2).

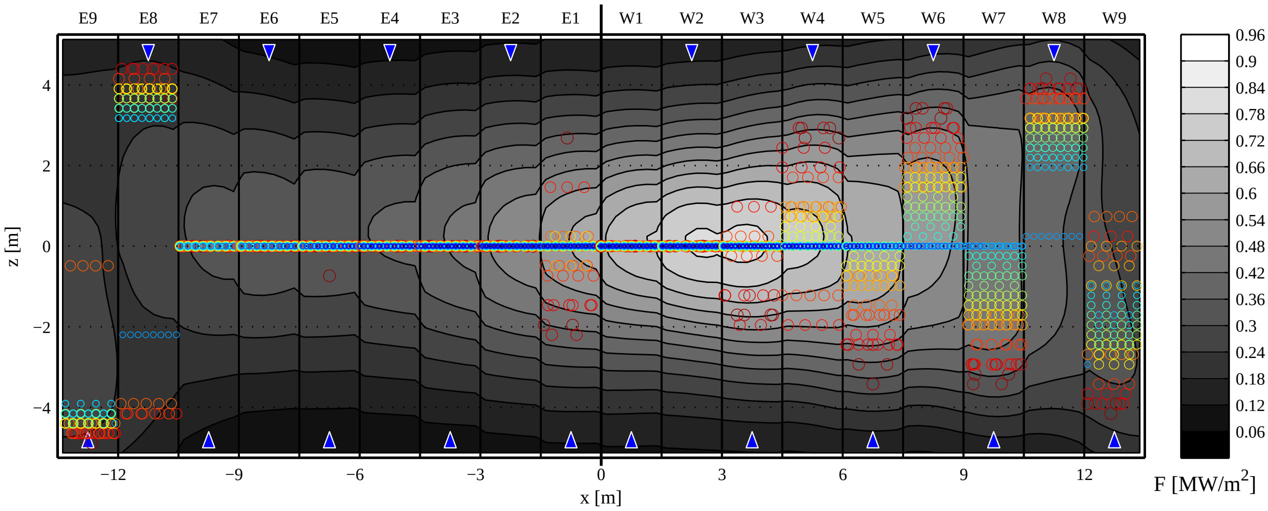

Figure 5.22: Flux density distribution at 7:00 solar time at summer solstice (DNI = 770 W/m^2). Circles represent the aim point of each heliostat colored by its distance to the receiver, according to Figure 5.3. Triangles point out the direction of the flow at each receiver panel.

patterns since the flow path is serpentine-like and the higher AFD is usually located at the entrance of each panel. Meeting contrary requirements is occasionally unattainable, as occurs for panels 7 and 8. The last panel of both flow paths is less affected by this issue due to their coincident flow direction.

Aiming factors, displayed in Figure 5.19, in the west side are regularly smaller than in the east. Consequently, greater vertical shifting of aim points is found in the west, see Figure 5.20. As expected, the peak flux density (0.91 MW/m^2) is detected at the anti-sun location.

Earlier in the morning, at 7:00, solar radiation incident on the receiver is lower, since direct normal irradiance (770W/m^2) is reduced, as well as the optical field efficiency mostly due to cosine and shading losses. As a consequence, the thermal power output from the receiver diminishes, as can be deduced from the mass flow rates displayed in Figure 5.21.

The AFD is not reached in most of the east side panels, even aiming at the equator. On the contrary, to

Table 5.1: Equatorial versus optimized aiming strategy. Output parameters for summer solstice.

Solar time	DNI [W/m^2]	$T_{f,max}$ [°C]		F_{max} [MW/m^2]		f_{int}		Q_{rec} [MW]	
		Eq.	Opt.	Eq.	Opt.	Eq.	Opt.	Eq.	Opt.
12	930	727	629	1.208	0.948	0.819	0.786	114.7	108.7
11	930	731	629	1.210	0.934	0.818	0.783	113.7	107.4
10	920	734	629	1.188	0.928	0.817	0.780	109.2	103.0
9	910	736	629	1.157	0.910	0.813	0.777	102.7	96.7
8	860	733	630	1.060	0.902	0.809	0.774	90.3	85.2
7	770	725	628	0.880	0.795	0.802	0.774	71.7	68.4
6	600	699	628	0.533	0.526	0.793	0.777	42.3	41.2

match the boundary in the west side, heliostats have to aim at different levels, as can be seen in Figure 5.22. Regardless of solar time, the last panels of both flow paths always require considerable vertical aim shifting which results in significant spillage loss.

The corrosion limiting film temperature of 630 °C is nowhere exceeded, as seen in previous Figures, which confirms the validity of the model. For different solar times at summer solstice, the maximum film temperature $T_{f,max}$ along with other key outputs are summarized in Table 5.1, which compares the model with the equatorial aiming. To meet the corrosion and thermal stress limits, the peak flux density becomes drastically reduced in the achieved aiming up to 23%. Nonetheless, the interception factor f_{int} falls no more than 0.04 points, because of the vertical spreading of aim points. The model ensures that the minimum possible spillage losses are added and the receiver output is thus maximized. Compared to the unfeasible single aiming, the receiver thermal power Q_{rec} is slightly reduced up to 6%.

5.6 Conclusions

In this Chapter it was exposed a model to determine nearly optimal aimings in molten salt CRS. The model consists of two iterative algorithms that search the aim points for the heliostats in a field. The objective is to maximize the interception and hence the receiver thermal power output, while preserving the integrity of the receiver. For the Gemasolar-like case study herein presented, the spillage factor falls just 0.04 points compared to the unreliable equatorial aiming.

The two major constraints in molten salt receivers, corrosion and thermal stress, were translated into allowable flux densities. The model uses these AFD limits within which heliostat flux densities are favorably accommodated. Besides the main algorithms, a calculation procedure to generate a database of AFD due to corrosion was successfully developed. The model also computes the thermal stress limits that can be predominant in the first receiver panels, where a rather flat flux profile is preferred in the central region.

It was found that, for most of the panels, the expected flux density profile has its peak displaced to the entrance of each receiver panel. This favorable flux profile has a slope towards the panel outlet that is more pronounced in the middle panels; those oriented to east and west. Serpentine flow pattern in cylindrical multi-panel receivers entails contrary requirements for adjacent panels, since the peak flux is expected at opposite heights. Despite this conflicting demand, the fit algorithm is capable of substantially matching the AFD profile.

The resulting tool is capable of accurately determining the optimal aim points for the heliostats in any field at any time. Because of its automatic and fast computation (around 2 minutes in a single core standard CPU), this aiming tool can be applied to the open-loop control and real-time operation of heliostat fields. Furthermore, an integrated design of heliostat field and central receiver is feasible on the basis of the developed aiming model.

Nomenclature

A	Difference between F and AFD profiles along the vertical [W/m]
AFD	Allowable flux density [W/m^2]
BR_k	Beam radius based on aiming factor [m]
C_p	Specific heat [J/kg·K]
D	Receiver diameter [m]
d	Tube diameter [m]
DNI	Direct normal irradiance [W/m^2]
E	Modulus of elasticity [Pa]
F	Solar flux density [W/m^2]
f	Optical loss factor [-]
H	Receiver height [m]
k	Aiming factor [-]
$\dot{m}$	Mass flow rate [kg/s]
N	Number [-]
PW	Panel width [m]
Q	Heat rate [W]
q	Heat flux density [W/m^2]
r	Row number
S	Stress [Pa]
SLR	Slant range [m]
T	Temperature [°C]
$\mathbf{t}$	Target vector
TC	Thermal conductivity [W/m·K]
TE	Coefficient of thermal expansion [m/m·K]
th	Tube thickness [m]
THT	Tower optical height [m]
TS	Tensile strength [Pa]
UTS	Ultimate tensile strength [Pa]
x, y	Coordinates [m]

Greek symbols

ΔT_r	Radial temperature difference [°C]
ε	Elevation angle [rad]
η	Efficiency [-]
ν	Poisson’s ration [-]
ρ	Mirror reflectivity [-]
σ	Error, standard deviation [rad]
ω	Incidence angle [rad]

Subscripts

amb	Ambient
conv	Convection
corr	Corrosion
e	Effective
f	Film
fp	Flow path
i	Inner tube surface
in	Inlet
int	Interception
j	Index (iteration)
lim	Limit
max	Maximum, peak
o	Outer tube surface
out	Outlet
p	Panel
r	Row
rad	Radiation
rec	Receiver
s	Molten salt
slp	Mirror slope
strs	Thermal stress

sun	Sunshape
t	Tube
trk	Tracking

Acronyms

CPU	Computer's central process unit
CRS	Central receiver system
HTF	Heat transfer fluid

References

ASME 2004 *ASME Boiler and Pressure Vessel Code*. New York: American Society of Mechanical Engineers.

Belhomme, B., Pitz-Paal, R. & Schwarzbözl, P. 2013 Optimization of Heliostat Aim Point Selection for Central Receiver Systems Based on the Ant Colony Optimization Metaheuristic. *Journal of Solar Energy Engineering* 136 (1), 011005.

Besarati, S. M., Yogi Goswami, D. & Stefanakos, E. K. 2014 Optimal heliostat aiming strategy for uniform distribution of heat flux on the receiver of a solar power tower plant. *Energy Conversion and Management* 84, 234–243.

Bradshaw, R. W. 1987 Thermal Convection Loop Study of the Corrosion of Incoloy 800 in Molten NaNO3-KNO3. *Corrosion* 43 (3), 173–178.

Collado, F. J., Gómez, A. & Turégano, J. 1986 An analytic function for the flux density due to sunlight reflected from a heliostat. *Solar Energy* 37 (3), 215–234.

Collado, F. J. & Guallar, J. 2013 A review of optimized design layouts for solar power tower plants with campo code. *Renewable and Sustainable Energy Reviews* 20, 142–154.

García-Martín, F., Berenguel, M., Valverde, A. & Camacho, E. F. 1999 Heuristic knowledge-based heliostat field control for the optimization of the temperature distribution in a volumetric receiver. *Solar Energy* 66 (5), 355–369.

Irfan, M. a. & Chapman, W. 2009 Thermal stresses in radiant tubes due to axial, circumferential and radial temperature distributions. *Applied Thermal Engineering* 29 (10), 1913–1920.

Lipps, F. W. & Vant-Hull, L. L. 1978 A cellwise method for the optimization of large central receiver systems. *Solar Energy* 20 (6), 505–516.

Modest, M. F. 2003 *Radiative heat transfer, Second edition*. Amsterdam: Academic press.

Pacheco, J. E. 2002 Final Test and Evaluation Results from the Solar Two Project. *Tech. Rep.* January. Sandia National Laboratories, SAND2002-0120.

Rodríguez-Sánchez, M., Marugan-Cruz, C., Acosta-Iborra, A. & Santana, D. 2014*a* Comparison of simplified heat transfer models and CFD simulations for molten salt external receiver. *Applied Thermal Engineering* 73, 991–1003.

Rodríguez-Sánchez, M., Sánchez-González, A., Marugán-Cruz, C. & Santana, D. 2015 Flow patterns of external solar receivers. *Solar Energy* 122, 940–953.

Rodríguez-Sánchez, M., Soria-Verdugo, A., Almendros-Ibáñez, J. A., Acosta-Iborra, A. & Santana, D. 2014*b* Thermal design guidelines of solar power towers. *Applied Thermal Engineering* 63 (1), 428–438.

Salomé, A., Chhel, F., Flamant, G., Ferrière, A. & Thiery, F. 2013 Control of the flux distribution on a solar tower receiver using an optimized aiming point strategy: Application to THEMIS solar tower. *Solar Energy* 94, 352–366.

Sánchez-González, A. & Santana, D. 2015 Solar flux distribution on central receivers: A projection method from analytic function. *Renewable Energy* 74, 576–587.

Sargent & Lundy 2003 Assessment of Parabolic Trough and Power Tower Solar Technology Cost and Performance Forecasts. *Tech. Rep.*. NREL, Golden, CO (United States).

Siebers, D. L. & Kraabel, J. S. 1984 Estimating convective energy losses from solar central receivers. *Tech. Rep.*. Sandia National Laboratories, SAND84-8717.

Vant-Hull, L. L. 2002 The Role of "Allowable Flux Density" in the Design and Operation of Molten-Salt Solar Central Receivers. *Journal of Solar Energy Engineering* 124 (2), 165.

Vant-Hull, L. L. 2012 Central tower concentrating solar power (CSP) systems. In *Concentrating solar power technology: principles, developments and applications*. Woodhead Publishing.

Young, W. C. & Budynas, R. G. 2002 *Roark's formulas for stress and strain*, , vol. 7. McGraw-Hill, New York.

Zavoico, A. B. 2001 Solar power tower: Design basis document. *Tech. Rep.* July. Sandia National Laboratories, SAND2001-2100.

CHAPTER

SIX

Concluding remarks

Deployment and consolidation of solar power tower technology demand, among other things, the development of models and tools to assist in design and operation phases. To a certain extend, accurate and reliable tools for SPT design and operation guarantee the success and positive attention in this technology.

This thesis essentially dealt with the development of optical models for SPT plants. The developed models allow the fast and accurate computation of:

- flux distributions on any kind of central receiver caused by a single heliostat or a field of them;
- canting errors from a few heliostat images on a lambertian target;
- symmetric flux maps with controlled spillage losses; and
- optimized aim points for molten salt central receivers.

Chapter 2 presented a 4-step methodology to determine flux density distributions on flat and cylindrical receivers. The procedure relies on the oblique projection of the receiver nodal mesh to the image plane, where an accurate analytic function, e.g. UNIZAR (Collado, 1986), is evaluated. Oblique projection is accomplished by transformation of coordinates system.

The projection method, in combination with UNIZAR analytic function, remarkably reproduces the distorted spot by rectangular focusing heliostats when incidence angle on the receiver is large. Validation succeeded against PSA measurements and MCRT simulations. Compared to SolTrace, the model lasts 50 times less and understimates intercept factor up to 2%, even though spatial resolution is higher in the model.

The rest of the models developed in this thesis were build upon the basic one described in Chapter 2. Even though the validated model is very accurate, further research would be required to implement astigmatic aberrations.

Chapter 3 presented an optimization procedure to determine alignment errors in the facets or modules of a heliostat. Taking advantage of a deterministic optimization algorithm named DIRECT, actual canting errors are found by minimizing the difference between experimental and computed flux distributions. For THEMIS heliostat, less than 2 hours of computation are required to find out the 17 angular deviations of the modules, achieving cross-correlation coefficients up to 98%. From the results, one of the heliostats was *in situ* readjusted, noticeably improving its optical quality. Compared to aligned flux maps predicted by the optical model, correlation coefficient rose from 72.8% to 93.3%, validating the proposed methodology.

In Chapter 4, the basic model was extended to account for a whole field of heliostats. In addition to the superposition of flux maps from single heliostats, the model computes optical loss factors. Shading and blocking losses are found by parallel projection of neighbor heliostats. CPU computation time is smaller than 1 minute in an standard PC, for a field of 2650 heliostats.

A 2-step methodology was developed to obtain flux maps symmetric about the receiver equator. Single parameter k, aiming factor, is needed to qualitatively control spillage losses and generate different patterns of flux distributions. Nearly equatorial aiming is gained through $k = 3$, whereas $k = 0$ leads to two peaks on upper and lower receiver edges, and spillages losses above 50%. For the Gemasolar case study, $k = 2$ yielded the most uniform flux maps, where the vertical profile is flat in the central region, and with negligible increase in spillage losses compared to single aiming.

Chapter 5 exposed an optimal aiming strategy for molten salt central receivers. Corrosion and thermal stress constrains were translated into allowable flux densities. An algorithm was developed to maximize receiver interception, while corrosion and stress limits are met at the same time. Compared to unreliable single aiming, the optimized aiming strategy increases spillage losses in 4 percentage points even though receiver integrity is maintained for the selected case study.

Based on the AFD approach, it was found that for most of the panels in a cylindrical receiver the optimal peak is not in the center but slightly shifted towards the panel entrance. This favorable flux profile has slope towards the panel outlet, which is more pronounced in the panels around the middle, i.e. broadly oriented to east and west. However, serpentine flow pattern in cylindrical multi-panel receivers entails contrary demands for adjacent panels, which are difficult to meet, specially near the boundary between them. Despite this conflicting demand, fit algorithm achieves great matching to the AFD profile.

The model described in Chapter 5 takes around 2 minutes in an ordinary PC to compute the optimal aiming points for the Gemasolar-like heliostat field. The resulting code was automated, so that it can be applied to nearly real-time control of heliostat fields and molten salt receivers.

In addition to the control of existing SPT plants, the developed models are suitable for the integrated design of the group heliostat field and central receiver. Given their close interaction, as revealed in Chapter 5, both subsystems might be analyzed jointly.

Alphabetical list of references

Arora, J. S. 2012 Global Optimization Concepts and Methods. In *Introduction to Optimum Design*, chap. 18, pp. 681–712. Elsevier.

ASME 2004 *ASME Boiler and Pressure Vessel Code*. New York: American Society of Mechanical Engineers.

Augsburger, G. & Favrat, D. 2013 Modelling of the receiver transient flux distribution due to cloud passages on a solar tower thermal power plant. *Solar Energy* 87, 42–52.

Ballestrín, J. & Marzo, A. 2012 Solar radiation attenuation in solar tower plants. *Solar Energy* 86 (1), 388–392.

Baum, V. A., Aparasi, R. R. & Garf, B. A. 1957 High-power solar installations. *Solar Energy* 1 (1), 6–12.

Belhomme, B., Pitz-Paal, R. & Schwarzbözl, P. 2013 Optimization of Heliostat Aim Point Selection for Central Receiver Systems Based on the Ant Colony Optimization Metaheuristic. *Journal of Solar Energy Engineering* 136 (1), 011005.

Belhomme, B., Pitz-Paal, R., Schwarzbözl, P. & Ulmer, S. 2009 A New Fast Ray Tracing Tool for High-Precision Simulation of Heliostat Fields. *Journal of Solar Energy Engineering* 131.

Besarati, S. M., Yogi Goswami, D. & Stefanakos, E. K. 2014 Optimal heliostat aiming strategy for uniform distribution of heat flux on the receiver of a solar power tower plant. *Energy Conversion and Management* 84, 234–243.

Biggs, F. & Vittitoe, C. N. 1979 Helios model for the optical behavior of reflecting solar concentrators. *Tech. Rep.*. Sandia National Laboratories, SAND-76-0347.

Blair, N., Dobos, A. P., Freeman, J., Neises, T., Wagner, M., Ferguson, T., Gilman, P. & Janzou, S. 2014 System advisor model, SAM 2014.1. 14: General description. *Tech. Rep.*. NREL & DoE, TP-6A20-61019.

Blanco, M. J., Amieva, J. M. & Mancillas, A. 2005 The tonatiuh software development project: An open source approach to the simulation of solar concentrating systems. In *ASME Conference Proceedings*. ASME.

Bradshaw, R. W. 1987 Thermal Convection Loop Study of the Corrosion of Incoloy 800 in Molten NaNO3-KNO3. *Corrosion* 43 (3), 173–178.

Braun, J. E. & Mitchell, J. C. 1983 Solar geometry for fixed and tracking surfaces. *Solar Energy* 31 (5), 439–444.

Burgaleta, J. I., Arias, S. & Ramirez, D. 2011 Gemasolar, the first tower thermosolar commercial plant with molten salt storage. In *SolarPACES*.

Chen, Y., Kribus, A., Lim, B., Lim, C., Chong, K., Karni, J., Buck, R., Pfahl, A. & Bligh, T. P. 2004 Comparison of Two Sun Tracking Methods in the Application of a Heliostat Field. *Journal of Solar Energy Engineering* 126 (1), 638.

Chong, K. 2014 Non-imaging Focusing Heliostat. In *Advanced Energy Materials* (ed. Ashutosh Tiwari & Sergiy Valyukh), chap. 1, pp. 1–67. John Wiley & Sons, Inc.

Collado, F. J. 2008 Quick evaluation of the annual heliostat field efficiency. *Solar Energy* 82 (4), 379–384.

Collado, F. J. 2010 One-point fitting of the flux density produced by a heliostat. *Solar Energy* 84 (4), 673–684.

Collado, F. J. 2011 Design of solar power tower plants heliostat by heliostat: The shadowing and blocking factor. In *SolarPACES*. Granada, Spain.

Collado, F. J., Gómez, A. & Turégano, J. 1986 An analytic function for the flux density due to sunlight reflected from a heliostat. *Solar Energy* 37 (3), 215–234.

Collado, F. J. & Guallar, J. 2009 Design of solar tower plants heliostat by heliostat: The blocking factor. In *SolarPACES*. Berlin, Germany.

Collado, F. J. & Guallar, J. 2012 Campo: Generation of regular heliostat fields. *Renewable Energy* 46, 49–59.

Collado, F. J. & Guallar, J. 2013 A review of optimized design layouts for solar power tower plants with campo code. *Renewable and Sustainable Energy Reviews* 20, 142–154.

Cooper, P. I. 1969 The absorption of radiation in solar stills. *Solar energy* 12 (3), 333–346.

Falcone, P. K. 1986 A handbook for solar central receiver design. *Tech. Rep.*. Sandia National Laboratories, SAND-86-8009.

Finkel, D. E. 2003 DIRECT Optimization Algorithm User Guide.

Galtier, M., Blanco, S., Caliot, C., Coustet, C., Dauchet, J., El Hafi, M., Eymet, V., Fournier, R., Gautrais, J., Khuong, A., Piaud, B. & Terrée, G. 2013 Integral formulation of null-collision Monte Carlo algorithms. *Journal of Quantitative Spectroscopy and Radiative Transfer* 125, 57–68.

Garcia, P., Ferrière, A. & Bezian, J.-J. 2008 Codes for solar flux calculation dedicated to central receiver system applications: A comparative review. *Solar Energy* 82 (3), 189–197.

García-Martín, F., Berenguel, M., Valverde, A. & Camacho, E. F. 1999 Heuristic knowledge-based heliostat field control for the optimization of the temperature distribution in a volumetric receiver. *Solar Energy* 66 (5), 355–369.

Hénault, F. 2015 Fast computation of solar concentrating ratio in presence of opto-mechanical errors. *Solar Energy* 112, 183–193.

Hildebrandt, A. F. & Vant-Hull, L. L. 1977 Power with Heliostats. *Science* 197 (4309), 1139–1146.

Ho, C. K. & Iverson, B. D. 2014 Review of high-temperature central receiver designs for concentrating solar power. *Renewable and Sustainable Energy Reviews* 29, 835–846.

Huang, W., Li, L., Li, Y. & Han, Z. 2013 Development and evaluation of several models for precise and fast calculations of shading and blocking in heliostats field. *Solar Energy* 95, 255–264.

Igel, E. & Hughes, R. 1979 Optical analysis of solar facility heliostats. *Solar Energy* 22, 283–295.

Irfan, M. a. & Chapman, W. 2009 Thermal stresses in radiant tubes due to axial, circumferential and radial temperature distributions. *Applied Thermal Engineering* 29 (10), 1913–1920.

Jones, D. R., Perttunen, C. D. & Stuckman, B. E. 1993 Lipschitzian optimization without the Lipschitz constant. *Journal of Optimization Theory and Applications* 79 (1), 157–181.

Jones, S. A. 1996*a* A comparison of on-axis and off-axis heliostat alignment strategies. In *American Solar Energy Society Conference*, pp. 95–100. Sandia National Laboratories, Asheville, NC (United States): SAND-96-0566C.

Jones, S. A. 1996*b* Annual performance prediction for off-axis aligned Lugo heliostats at Solar Two. In *American Society of Mechanical Engineers international solar energy conference*. Sandia National Laboratories, San Antonio, TX (United States): SAND-96-0212C.

Jones, S. A., Edgar, R. M. & Houser, R. M. 1994 Recent results on the optical performance of solar two heliostats. In *American Society of Mechanical Engineers international solar energy conference*. Sandia National Laboratories, Lahaina, HI (United States): SAND-94-2776C.

Kaelo, P. & Ali, M. M. 2006 Some variants of the controlled random search algorithm for global optimization. *Journal of Optimization Theory and Applications* 130 (2), 253–264.

Kalogirou, S. A. 2009 Solar Thermal Power Systems. In *Solar Energy Engineering: Processes and Systems*, chap. 10, pp. 521–552. Elsevier.

Kistler, B. 1986 A user's manual for DELSOL3: Computer code for calculating the optical performance and optimal system design for solar thermal central receiver plants. *Tech. Rep.*. Sandia National Laboratories, SAND-86-8018.

Lata, J. M., Alcalde, S., Fernández, D. & Lekube, X. 2010 First surrounding field of heliostats in the world for commercial solar power plants - Gemasolar. In *Proceedings of SolarPACES*.

Leary, P. L. & Hankins, J. D. 1979 User's guide for MIRVAL: a computer code for comparing designs of heliostat-receiver optics for central receiver solar power plants. *Tech. Rep.*. Sandia National Laboratories, SAND-77-8280.

Li, L., Coventry, J., Bader, R., Pye, J. & Lipiński, W. 2016 Optics of solar central receiver systems: a review. *Optics Express* 24 (14).

Lipps, F. W. 1992 Computer Simulation of Shading and Blocking : Discussion of Accuracy and Recommendations. *Tech. Rep.* April 1992. NREL, National Renewable Energy Laboratory, Golden, Colorado.

Lipps, F. W. & Vant-Hull, L. L. 1978 A cellwise method for the optimization of large central receiver systems. *Solar Energy* 20 (6), 505–516.

Lipps, F. W. & Walzel, M. D. 1978 An analytic evaluation of the flux density due to sunlight reflected from a flat mirror having a polygonal boundary. *Solar Energy* 21 (2), 113–121.

Litwin, R. Z. & Park, C. 2002 Receiver System : Lessons Learned from Solar Two. *Tech. Rep.* March. Sandia National Laboratories.

Lovegrove, K. & Stein, W. 2012 Introduction to concentrating solar power (CSP) technology. In *Concentrating Solar Power Technology*, chap. 1, pp. 3–15. Woodhead Publishing - Elsevier.

Modest, M. F. 2003 *Radiative heat transfer, Second edition.* Amsterdam: Academic press.

Monterreal, R. 2013 Personal communication.

Nelder, J. A. & Mead, R. 1965 A Simplex Method for Function Minimization. *The Computer Journal* 7 (4), 308–313.

Pacheco, J. E. 2002 Final Test and Evaluation Results from the Solar Two Project. *Tech. Rep.* January. Sandia National Laboratories, SAND2002-0120.

Piaud, B., Coustet, C., Caliot, C., Guillot, E. & Flamant, G. 2012 Application of Monte-Carlo sensitivities estimation in Solfast-4D. In *SolarPACES*.

Ren, L., Wei, X., Lu, Z., Yu, W., Xu, W. & Shen, Z. 2014 A review of available methods for the alignment of mirror facets of solar concentrator in solar thermal power system. *Renewable and Sustainable Energy Reviews* 32, 76–83.

Roccia, J. P., Piaud, B., Coustet, C., Caliot, C., Guillot, E., Flamant, G. & Delatorre, J. 2012 SOLFAST, a Ray-Tracing Monte-Carlo software for solar concentrating facilities. *Journal of Physics: Conference Series* 369, 012029.

Rodríguez-Sánchez, M., Marugan-Cruz, C., Acosta-Iborra, A. & Santana, D. 2014*a* Comparison of simplified heat transfer models and CFD simulations for molten salt external receiver. *Applied Thermal Engineering* 73, 991–1003.

Rodríguez-Sánchez, M., Sánchez-González, A., Marugán-Cruz, C. & Santana, D. 2014*b* Saving assessment using the PERS in solar power towers. *Energy Conversion and Management* 87, 810–819.

Rodríguez-Sánchez, M., Sánchez-González, A., Marugán-Cruz, C. & Santana, D. 2015*a* Flow patterns of external solar receivers. *Solar Energy* 122, 940–953.

Rodríguez-Sánchez, M., Sanchez-Gonzalez, A. & Santana, D. 2015*b* Revised receiver efficiency of molten-salt power towers. *Renewable and Sustainable Energy Reviews* 52, 1331–1339.

Rodríguez-Sánchez, M., Soria-Verdugo, A., Almendros-Ibáñez, J. A., Acosta-Iborra, A. & Santana, D. 2014*c* Thermal design guidelines of solar power towers. *Applied Thermal Engineering* 63 (1), 428–438.

Romero-Alvarez, M. & Zarza, E. 2007 Concentrating Solar Thermal Power. In *Handbook of Energy Efficiency and Renewable Energy*, , vol. 20070849, chap. 21, pp. 21.1–21.97. Taylor and Francis Ltd.

Salomé, A., Chhel, F., Flamant, G., Ferrière, A. & Thiery, F. 2013 Control of the flux distribution on a solar tower receiver using an optimized aiming point strategy: Application to THEMIS solar tower. *Solar Energy* 94, 352–366.

Sánchez-González, A., Caliot, C., Ferriere, A. & Santana, D. 2017 Determination of heliostat canting errors via deterministic optimization. *Solar Energy* 150, 136–146.

Sánchez-González, A., Rodríguez-Sánchez, M. & Santana, D. 2016 Aiming strategy model based on allowable flux densities for molten salt central receivers. *Solar Energy* In press (http://dx.doi.org/10.1016/j.solener.2015.12.055).

Sánchez-González, A. & Santana, D. 2015 Solar flux distribution on central receivers: A projection method from analytic function. *Renewable Energy* 74, 576–587.

Sargent & Lundy 2003 Assessment of Parabolic Trough and Power Tower Solar Technology Cost and Performance Forecasts. *Tech. Rep.*. NREL, Golden, CO (United States).

Schmitz, M., Schwarzbözl, P., Buck, R. & Pitz-Paal, R. 2006 Assessment of the potential improvement due to multiple apertures in central receiver systems with secondary concentrators. *Solar Energy* 80 (1), 111–120.

Schwarzbözl, P., Schmitz, M. & Pitz-paal, R. 2009 Visual HFLCAL - A software tool for layout and optimisation of heliostat fields. In *SolarPACES*. Berlin, Germany.

Siebers, D. L. & Kraabel, J. S. 1984 Estimating convective energy losses from solar central receivers. *Tech. Rep.*. Sandia National Laboratories, SAND84-8717.

SNL 2013 TOPHAT. *Theoretical Overlay Photographic Heliostat Alignment Technique* (https://ip.sandia.gov/technology.do/techID=16).

SolarConcentra 2013 Identificación de las principales líneas de investigación en el sector de la electricidad termosolar. *Tech. Rep.*. Solar Concentra.

Sproul, E., Chavez, K. & Yellowhair, J. 2011 The Development of the Heliostat Focusing and Canting Enhancement Technique: An Optical Heliostat Alignment Tool for the National Solar Thermal Test Facility. In *ASME 2011 5th International Conference on Energy Sustainability, Parts A, B, and C*, pp. 611–619. ASME.

Strachan, J. W. & Houser, R. M. 1993 Testing and evaluation of large-area heliostats for solar thermal applications. *Tech. Rep.*. Sandia National Laboratories, SAND92-1381.

Theodoridis, S. & Koutroumbas, K. 2009 Template Matching. In *Pattern Recognition*, chap. 8, pp. 481–519. Academic press - Elsevier.

USNO 2016 Solar position. *Online calculator* (http://aa.usno.navy.mil/data/docs/AltAz.php).

Vant-Hull, L. L. 2002 The Role of "Allowable Flux Density" in the Design and Operation of Molten-Salt Solar Central Receivers. *Journal of Solar Energy Engineering* 124 (2), 165.

Vant-Hull, L. L. 2012 Central tower concentrating solar power (CSP) systems. In *Concentrating solar power technology: principles, developments and applications*, chap. 8. Woodhead Publishing - Elsevier.

Vignarooban, K., Xu, X., Arvay, A., Hsu, K. & Kannan, A. 2015 Heat transfer fluids for concentrating solar power systems: A review. *Applied Energy* 146, 383–396.

Walzel, M. D., Lipps, F. W. & Vant-Hull, L. L. 1977 A solar flux density calculation for a solar tower concentrator using a two-dimensional Hermite function expansion. *Solar Energy* 19 (3), 239–253.

Wang, Y., Dong, X., Wei, J. & Jin, H. 2010 Numerical simulation of the heat flux distribution in a solar cavity receiver. *Frontiers of Energy and Power Engineering in China* 4 (4), 571–576.

Wendelin, T. 2003 SolTRACE: a new optical modeling tool for concentrating solar optics. In *ISEC*. ASME.

Wendelin, T., Dobos, A. & Lewandowski, A. 2013 SolTrace: A Ray-Tracing Code for Complex Solar Optical Systems. *Tech. Rep.*. NREL, National Renewable Energy Laboratory, Golden, Colorado.

Yellowhair, J. & Ho, C. K. 2010 Heliostat Canting and Focusing Methods: An Overview and Comparison. In *ASME 2010 4th International Conference on Energy Sustainability, Volume 2*, pp. 609–615. ASME.

Young, W. C. & Budynas, R. G. 2002 *Roark's formulas for stress and strain*, , vol. 7. McGraw-Hill, New York.

Yuan, J. K., Christian, J. M. & Ho, C. K. 2014 Compensation of Gravity Induced Heliostat Deflections for Improved Optical Performance. *Journal of Solar Energy Engineering* 137 (2), 021016.

Zavoico, A. B. 2001 Solar power tower: Design basis document. *Tech. Rep.* July. Sandia National Laboratories, SAND2001-2100.